DØ note 3400

Measurement of the Top Quark Mass

by

Tzu-Chung Frank Hsieh

A dissertation submitted in partial fulfillment
of the requirements for the degree of
Doctor of Philosophy
(Physics)
in The University of Michigan
1998

Doctoral Committee:

Assistant Professor Jianming Qian, Chair
Professor Timothy Chupp
Professor Robert Keener
Professor Byron Roe
Professor Edward Yao

Abstract

Measurement of the Top Quark Mass

by

Tzu-Chung Frank Hsieh

Chair: Jianming Qian

From $p\overline{p}$ collisions at $\sqrt{s} = 1.8\,\text{TeV}$ in the Fermilab Tevatron collider, top quarks are produced predominantly in $t\overline{t}$ pairs. After applying a sophisticated event selection to the $\approx 100\,\text{pb}^{-1}$ data recorded by the DØ detector, we have 35 $t\overline{t} \rightarrow e(\mu) + \text{jets}$ candidates with the background estimated to be 16.3 ± 2.2. We perform a kinematically constrained fit for individual events, and the results are input to a likelihood analysis. We compare the expectations with our observation and determine the top quark mass to be $m_t = 177.0 \pm 7.3\,(\text{stat})\ {}^{+4.1}_{-5.5}\,(\text{syst})\ \text{GeV}/c^2$.

For since the creation of the world God's invisible qualities—his eternal power and divine nature—have been clearly seen, being understood from what has been made . . .

—Book of Romans 1:20

To my mother Lin-yin

Acknowledgements

This experiment would be impossible without the participation of many people. I want to thank the largely unknown heros in the Fermilab Accelerator Division, in the DØ control room, and those who have designed, tested, and commissioned the DØ detector. Their endeavors and contributions provided the solid foundation that later analyses of data have been built upon.

My decision to enter the field of high energy physics was partly influenced by Prof. Byron Roe, whose broad knowledge, sincerity and dedication I admire immensely. I would not have completed this dissertation if Prof. Homer Neal did not give me an opportunity to join his group and the DØ collaboration. To them, I would like to express my sincere gratitude.

In addition, I am also deeply indebted to Dr. Chip Stewart and my dissertation advisor Prof. Jianming Qian. They helped me understand the DØ software when I first came to this large collaboration. Many thanks for their supervision and assistance.

As a member of Michigan-DØ group, I have been privileged to know these talented people: Dr. Norm Amos, Dr. Don Lincoln, Dr. Ken DelSignore, Lori Oesch, and graduate students Sailesh Chopra, Xingshuan Lee, and Eric Neis. I appreciate the experience of working with them. In particular, I learned a lot from Don when we worked together on the Preshower Detector project. I also want to thank him for his many valuable suggestions on my dissertation writing.

For the analysis of this dissertation, I am thankful to many people in the top group at DØ. Earlier pioneers have devoted many years to the search for the top quark, and their efforts have laid the ground work for the top mass analyses. I also benefited amply from the interactions within the top-mass subgroup—the analyses presented, the subjects discussed, and the questions raised in the group meetings.

Among the physicists who have contributed to the work on the top mass measurement, I would like to thank Tom Ferbel, Mike Jones, Myungyun Pang, Rich Partridge, Serban Protopopescu, Scott Snyder, Mark Strovink, and Eric Varnes. Their strenuous and unyielding spirit in the pursuit of this complicated measurement has been very inspiring to me.

My first two years as a graduate student in Ann Arbor will always be memorable. I will never forget Prof. Karl T. Hecht for his kindness and dedication, his wonderful lectures and demanding homework. The life in Ann Arbor would not as pleasant if there had not been so many scholars with different specialties and ideas. I enjoyed the friendship of people from different fields. Among them, I thank David Stephenson, a computer scientist and mathematician, for conversations and exchanges of ideas and life experiences, and another mathematician Mihai Ciucu and his wife Gabi.

At Fermilab, I was fortunate to know Taylor Goss of Texas A&M. For two years, we shared an apartment and went to the same church. Together with Jeff Tseng of MIT, we had wonderful times in Bible studies and in conversation during lunches. I have been equally blessed to have two close friends, Ssu-min Chang and Yi-cheng Liu at DØ. They were like brothers to me, always ready to help when I was in need. I am also grateful for the friendship of Chyi-chang Miao, then a student in Michigan-CDF group, and some Taiwanese friends in the Accelerator Division, CDF, and fixed target experiments.

I have enjoyed wonderful friendships with the elders and friends in church. I especially thank Don & Sally Brinks, Lendall & Cheryl Smith, Calvin & Ruth Long, Chau & Chin-Mei Wu, and Franz & Shelley Tsai for their love and support.

Finally I want to thank my wife, Li-yen, with whom I have had so many wonderful times.

Preface

The DØ experiment was proposed in 1983 and began taking data in 1992. The collaboration now consists of more than 500 physicists and technical personnel. The interests being pursued with the DØ detector include top physics, B physics, QCD, new phenomena (SUSY), and electroweak physics.

I began my residency at DØ in 1994. My first assignment was to study the uniformity of the Intercryostat Detector (ICD), a component of the DØ detector. Later, I worked with Dr. Don Lincoln on the Preshower Detector project for the DØ upgrade. I helped him build a prototype module and conduct cosmic ray tests. To become involved with a physics analysis, I began going to the top group meetings in 1995 and started writing programs for my top quark mass analysis. Over the years, I have worked on algorithms to minimize the effects of the Main-Ring contamination and hot cells, developed jet corrections, and studied jet energy scale for the top quark mass measurements.

There are many people at DØ who participated in the studies and measurements involving the top quark. The analysis presented in this dissertation represents one of the analyses of the top quark mass measurement. As is the nature of a collaborative effort, my analysis is built on the results of previous work. The discussion contained in chapters 3 & 4 detail some of the earlier efforts on the event reconstruction and selection. My contribution includes the jet corrections, the kinematic fitting, and the likelihood analysis presented in chapters 5 to 7. The jet corrections described in this dissertation were used in other top quark mass analyses at DØ. While the rest of this analysis was not published, it served as a cross-check for the published results.

I appreciate the opportunity to work on this subject and the experience of collaborating with so many devoted coworkers in this experiment. It is a great delight to see how the secrets of nature can be unveiled through the collective and coordinated work of many individuals.

Contents

Chapter

List of Tables

List of Figures

Chapter 1

Introduction

Since Ernest Rutherford probed the structure of the atom by scattering α-particles from a fixed target, a plethora of particles has been discovered from high energy collisions by the sophisticated particle detectors made possible by modern technology. Our understanding of the interactions between these subatomic particles has evolved as experimental data has grown. This knowledge has been combined into what we now call the "Standard Model."

Since the bottom quark was discovered in 1977 [1], physicists have searched for the top quark from high energy particle collisions without success. The difficulty in discovering the top quark stems from the fact that it is much heavier than other particles and requires a much higher collision energy to produce. At the Fermilab Tevatron, protons and antiprotons are accelerated to 900 GeV, achieving a 1.8 TeV center-of-mass energy. In 1995, after three years of data taking, both the CDF and DØ experiments had accumulated enough data to announce the discovery of the top quark [2, 3].

In this dissertation, we will present how the mass of the top quark is measured from a 100 pb^{-1} data set recorded by the DØ detector. We begin with a brief overview of the Standard Model and an introduction to top quark physics.

1.1 The Standard Model

As Victor Weisskopf put it, the Standard Model is "logically compelling and empirically successful" [4]. Gradually shaped by decades of physicists' efforts, the Standard Model has survived many tests, with no experimental result contradicting it. The grand picture of the Standard Model centers upon the fundamental particles and the four distinct forces between them.

1.1.1 Forces and Fundamental Particles

The four forces which we know in nature are: the gravitational force, the electromagnetic force, the weak force, and the strong force. The gravitational force between two objects with mass is too weak to be considered at the sub-atomic level and can be safely neglected in studying particle interactions at short distances. The electromagnetic force acts between charged particles. The weak force is most familiar in the nuclear beta decay, where a neutron is turned into a proton in the nucleus and an electron is emitted. The strong force is responsible for binding nucleons (protons and neutrons) together in the nucleus, overcoming the electromagnetic repulsion of the protons.

According to the Standard Model, there are two classes of structure-less particles. One class is called leptons and the other, quarks. Both of them are spin 1/2 fermions. The distinction between the two classes is that leptons do not participate in strong interactions.

There are three kinds of charged leptons: the electron (e), the muon (μ) and the tau (τ) with the same electric charge but distinct masses (see Table 1.1). There are also three types of neutral leptons which we call neutrinos. Neutrinos only participate in weak interactions and may be massless—a question that is currently undergoing vigorous investigation.

The concept of quarks was first proposed by Murray Gell-Mann [5] and George Zweig [6] in the 1960s, and was strongly supported by the ensuing lepton-nucleon collision (deep inelastic scattering) and e^+e^- annihilation experiments. In the original quark theory, there were only three types, or "flavors", of quarks: up, down, and

Quarks (spin 1/2)	Charge (e)	Mass (MeV/c^2)
u	+2/3	$2-8$
d	-1/3	$5-15$
c	+2/3	$1,000-1,600$
s	-1/3	$100-300$
t	+2/3	$\sim$175,000
b	-1/3	$4,100-4,500$
Leptons (spin 1/2)	Charge (e)	Mass (MeV/c^2)
e	-1	0.51
ν_e	0	$< 7.3 \times 10^{-6}$
μ	-1	105.6
ν_μ	0	< 0.17
τ	-1	1,777
ν_τ	0	< 24
Field Quanta (spin 1)	Charge (e)	Mass (MeV/c^2)
g (gluons)	0	0
γ (photons)	0	0
$W^\pm$	±1	80,300
Z	0	91,190

Table 1.1: Fundamental particles of the Standard Model.

strange. Later, another flavor of quark, charm, was theoretically proposed [7] and found experimentally shortly thereafter [8, 9] in 1974. The number of quark flavors increased again with the discovery of the bottom quark in 1977. Today, with the newly discovered top quark, we know there exists six flavors of quarks. A series of e^+e^- annihilation experiments showed that quarks possess fractional charges (the charge of electron $= -1$): some flavors of quarks (u, c, t) have charge $+2/3$ and others (d, s, b) have charge $-1/3$.

All interactions can be seen as forces caused by an exchange of the force carriers or field quanta between interacting particles. For electromagnetic interactions, the force carrier is the photon (γ). For the weak interaction, the force carrier can be one of three intermediate vector bosons: W^+, W^- or Z^0. The strong force is transmitted by the gluons (g). All of the force carriers are spin 1 bosons.

Interactions are described by gauge theories in which the Lagrangian remains invariant under space-time transformations. The electromagnetic and weak forces can be brought to unification as an electroweak force that exhibits an SU(2) × U(1) symmetry [10, 11, 12], while for the strong force, Quantum Chromodynamics (QCD) is a gauge theory based on the symmetry group SU(3). These gauge theories have proven to be renormalizable [13] (i. e. cross section calculations result in non-infinite values when higher order processes are considered) even when the symmetry is spontaneously broken.

Leptons, quarks and field quanta are all massless in the gauge theories. It is through a spontaneous symmetry breaking mechanism [11, 12] by which they are endowed with their masses. In this mechanism, the existence of an electrically neutral, spin-0 Higgs boson is predicted, but yet to be confirmed experimentally.

1.1.2 The Electromagnetic Force

The electromagnetic force acts only on particles with electric charge. Because its field quanta (photons) carry no electric charge, particles do not change their electric charge as a result of this interaction. Examples of electromagnetic interactions include Compton scattering, pair-annihilation and scattering of charged leptons. The theory of Quantum Electrodynamics (QED) [14, 15, 16] has been developed based on P.A.M. Dirac's relativistic quantum theory [17] and the techniques of perturbation theory. Because of the small numerical value of the fine structure constant ($\alpha \approx 1/137$), perturbation method works very well in QED. The results of QED calculations are in excellent agreement with experimental measurements.

1.1.3 The Weak Force

In contrast to the massless photon which mediates the electromagnetic force, as a result of broken $\mathrm{SU}(2) \times \mathrm{U}(1)$ symmetry, the W and Z bosons that transmit the weak force are remarkably heavy ($M_W \approx 80\,\mathrm{GeV}/c^2$ and $M_Z \approx 91\,\mathrm{GeV}/c^2$).

In a typical beta decay ($n \to p\; e\; \bar{\nu}_e$), the electron is emitted with an electron-type antineutrino. This also happens in muon decay ($\mu \to \nu_\mu\; e\; \bar{\nu}_e$) and other weak decays. In all charge-changing weak interactions, we find there is a partnership between a charged lepton and a neutrino. Similar partnerships between different flavors of quarks also exist in hadronic weak interactions. By this relation, we can group leptons and quarks as:

$$\begin{array}{cc} \text{Leptons} & \text{Quarks} \\ \begin{pmatrix} \nu_e \\ e \end{pmatrix} \begin{pmatrix} \nu_\mu \\ \mu \end{pmatrix} \begin{pmatrix} \nu_\tau \\ \tau \end{pmatrix} & \begin{pmatrix} u \\ d \end{pmatrix} \begin{pmatrix} c \\ s \end{pmatrix} \begin{pmatrix} t \\ b \end{pmatrix} \end{array}$$

We call each pair of the weak partners a family (or generation). To date, we know of three families of leptons and quarks.

When the weak force is transmitted by a W boson, the interacting lepton or quark will turn into its partner. This transformation is called "charged current" because there is a charge difference between the incoming and outgoing weak partners. It is also observed that the weak interaction can be mediated by the neutral Z boson [18]. When this occurs, the interacting leptons or quarks are not transformed to another type, thus creating the so-called "neutral currents."

When quarks are involved in weak interactions, there is an interesting phenomenon called "quark mixing" [19, 20] due to the fact that the weak eigenstate and the mass eigenstate are not the same for quarks. A quark in its mass eigenstate is actually a superposition of different weak eigenstates. Therefore, a quark does not always turn into its weak parter when a W boson is absorbed or emitted. For instance, in c-quark decay, in addition to $c \to \bar{s}\, e(\mu)\, \bar{\nu}_e(\bar{\nu_\mu})$, the other channel $c \to \bar{d}\, e(\mu)\, \bar{\nu}_e(\bar{\nu_\mu})$ is also possible, although less likely.

Another property of the weak force is the "universality": charged currents couple to the W with approximately the same strength. In fact, the strengths of couplings are slightly different for leptons and quarks, but the difference can be understood when quark-mixing is considered. This property allows us to easily estimate the branching ratios of the top quark decay.

1.1.4 The Strong Force

The gluons are the force carrier of the strong force. In analogy to electric charges in the electromagnetic force, we call the source of the strong force between quarks "color" charge. What differs from the electric charge is that there are three types of color charge, symbolically labeled as red, green and blue. The field theory that describes the strong force induced by the color charges is called Quantum Chromodynamics (QCD).

Another distinction between the electromagnetic and strong forces is that while photons carry no electric charge, gluons carry color charges. Therefore, not only can gluons couple to quarks, but they can also couple to each other. This results in a unique character of the strong force, called "color confinement": quarks do not exist by themselves, instead they will combine with other quarks or antiquarks to form color neutral hadrons. Those hadrons consisting of three composite quarks, each with different color to keep a color neutral state, are categorized as baryons. Other hadrons, made out of a quark and an antiquark of the same color, are called mesons.

At the Tevatron collider, we can study interactions involving quarks in high energy proton-antiproton collisions. Within the highly energetic proton, both quarks and gluons share its momentum and can be treated as free particles when a collision occurs. This picture is called the "parton model" [21, 22], in which the quarks and gluons within an energetic hadron are referred to as "partons." The success of this model is due to the "asymptotic freedom" [23, 24] of the strong force—the strong coupling strength becomes smaller as the momentum transfer increases, allowing partons to be treated as free particles in high energy collisions. It is also the reason that high energy strong interactions are calculable in QCD by the perturbative method.

Because of color confinement, the scattered parton will use part of its energy to create quark-antiquark pairs to form a cluster of hadrons. This is the process of "fragmentation" or "hadronization." Those hadrons created in the process of fragmentation from high energy partons are highly collimated and are observed in the tracking detectors and the calorimeters. The reconstructed cluster of hadrons is called "jet."

1.2 The Top Quark

As the weak partner of the bottom quark, the existence of the top quark was predicted by the Standard Model. For many years, efforts in the top quark search only resulted in its ever increasing mass limit [25, 26, 27, 28]: from $m_t > 44\,\mathrm{GeV}/c^2$ set by the UA1 collaboration to $m_t > 131\,\mathrm{GeV}/c^2$ by the DØ collaboration. Eventually, the Standard Model was once again vindicated when the top quark was discovered by both the CDF and DØ experiments in 1995.

1.2.1 Production of the Top Quark

At a proton-antiproton collision energy of 1.8 TeV , the top quark (t) and the anti-top quark ($\bar{t}$) are produced in pairs from the strong interaction between a quark and an antiquark, or between two gluons as shown in Figure 1.1. The cross section of the $t\bar{t}$ production at Tevatron has been calculated as a function of the top quark mass using QCD [29] and it is on the order of a few pico-barns ($10^{-36}\,\mathrm{cm}^2$) as shown in Figure 1.2.

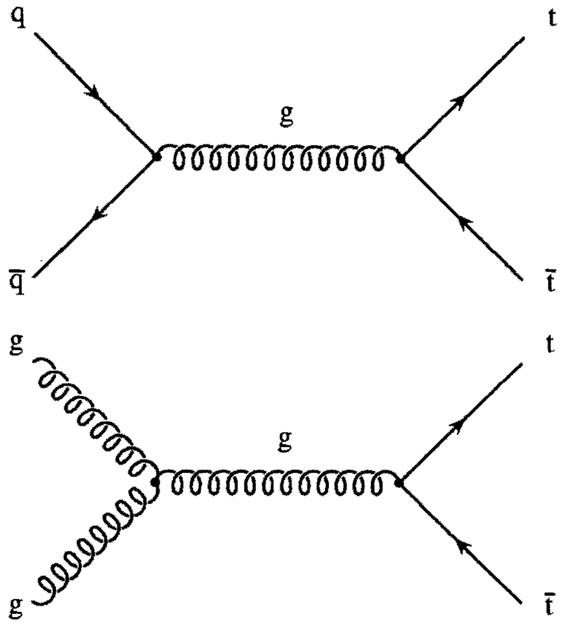

Figure 1.1: The lowest order Feynman diagrams of $t\bar{t}$ production.

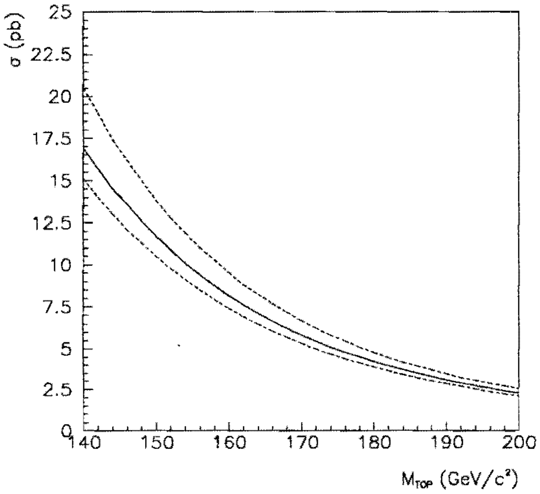

Figure 1.2: The theoretical $t\bar{t}$ production cross section as a function of the top quark mass. Dashed lines represent uncertainties associated with the calculation.

1.2.2 Decay of the Top Quark

Because the top quark mass is larger than the sum of the bottom quark and W boson masses, after the t is produced, it immediately decays before hadronization into a bottom quark and W boson ($t \to b\,W^+$ and its charge conjugate decay $\bar{t} \to \bar{b}\,W^-$). The W boson then decays either leptonically into a charged lepton and a neutrino ($W^- \to l\,\bar{\nu}_l$, $W^+ \to l^+\,\nu_l$), or decays hadronically into a quark and its weak partner antiquark ($W^+ \to c\,\bar{s}\,\mathrm{or}\,u\,\bar{d}$, $W^- \to \bar{c}\,s\,\mathrm{or}\,\bar{u}\,d$). The process of the top quark decay is depicted in Figure 1.3.

Depending on how the W bosons decay, a $t\bar{t}$ event has different signatures in the detector. If both W bosons decay leptonically, we have a two-charged-lepton final state. If one W decays leptonically and the other W decays hadronically, we will have only one charged lepton in the event. Similarly, if both W's decay hadronically, no charged lepton will be seen in the final state. As we mentioned earlier, a final state quark will hadronize to a jet because of the color confinement. Therefore, the decay modes of a $t\bar{t}$ event can be categorized as:

- the dilepton channels: $t\bar{t} \to l_1\,\bar{\nu}_1\,l_2^+\,\nu_2\,b\,\bar{b}$
- the lepton+jets channels: $t\bar{t} \to l\,\bar{\nu}\,q\bar{q}'\,b\,\bar{b}$
- the all-jets channel: $t\bar{t} \to q_1\,\bar{q}_1{}'\,q_2\,\bar{q}_2{}'\,b\,\bar{b}$

The universality of the weak decay predicts that 1/3 of the time the W decays into a charged lepton and its neutrino partner (1/9 for each family), and 2/3 of the time it decays into quark-antiquark pair, considering the three color charges a quark can possess. Consequently we can easily calculate the branching ratio of $t\bar{t}$ decay channels as shown in Table 1.2.

However, in the search for $t\bar{t}$ events, we do not include channels involving τ because the τ cannot be easily distinguished from jets in the detector (hadrons are very likely to be produced in the τ decay). From Table 1.2, the branching ratio for the τ-excluded dilepton channels (ee, $e\mu$, $\mu\mu$ channels) is 4/81 or 4.9%. e+jets and μ+jets together make up 24/81 or 29.6% branching ratio, and the all-jet channel has the largest share of 36/81 or 44.4%.

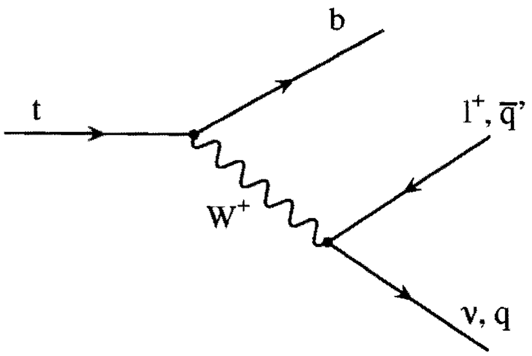

Figure 1.3: The Feynman diagram of the top quark decay.

$W \rightarrow$ $\downarrow$	$e\nu_e$ (1/9)	$\mu\nu_\mu$ (1/9)	$\tau\nu_\tau$ (1/9)	$q\bar{q}'$ (6/9)
$e\nu_e$ (1/9)	1/81	1/81	1/81	6/81
$\mu\nu_\mu$ (1/9)	1/81	1/81	1/81	6/81
$\tau\nu_\tau$ (1/9)	1/81	1/81	1/81	6/81
$q\bar{q}'$ (6/9)	6/81	6/81	6/81	36/81

Table 1.2: Branching fractions of $t\bar{t}$ decay channels.

Event channel	Signature	Branching ratio
Dilepton	two high p_T e or μ large $\not{E}_T$ two or more jets	$\approx 5\%$
Lepton+jets	one high p_T e or μ large $\not{E}_T$ multiple jets	$\approx 30\%$
All-jet	six or more jets	$\approx 44\%$

Table 1.3: The branching ratio and signature of $t\bar{t}$ decay channels. Channels involving the τ lepton are excluded.

The signature of a $t\bar{t}$ event is characterized by high p_T (transverse momentum) leptons and jets. This is due to the high mass of the top and the W—their decay products tend to come out at a wide angle with respect to their parent's momentum. For the lepton+jets and dilepton channels, there will be one or two neutrinos from the W decay in the event. Since neutrinos only interact via weak interactions for which the cross section is small, a high p_T neutrino usually leaves a transverse momentum imbalance (missing E_T or $\not{E}_T$) in the detector. The branching ratio and signature for various $t\bar{t}$ channels are summarized in Table 1.3.

Although the dilepton channels make up only a small portion of the $t\bar{t}$ branching ratio, they have the smallest background, which mainly comes from Z+jets and Drell-Yan production. On the other hand, the all-jet channel occupies the largest branching ratio, but it also encounters a huge QCD-multijet background. The lepton+jets channels are better than dilepton channels in terms of branching ratio, and their background is much less than that of the all-jet channel. Therefore, the lepton+jets channels are the most advantageous in terms of the number of observed events and the background level. In addition, the top quark mass is easier to reconstruct from the lepton+jets channels than from others—the dilepton event consists of two unmeasured neutrinos and in the all-jet event there are too many possible jet combinations. Not surprisingly, the lepton+jets events have been used to make the most precise measurement of the top quark mass. In the rest of the dissertation, we will discuss how to extract the top quark mass from the lepton+jets events.

1.2.3 The Top Quark Mass

It is necessary to determine the mass of a newly discovered particle. Besides this, there are other reasons that adds to the significance of the top quark mass measurement. First of all, the top quark is the heaviest fundamental particle, and its mass is one of the arbitrary Standard Model parameters[1] [30].

---

[1] The rest of parameters are masses of the other five quarks and three charged leptons, three gauge coupling constants (for the EM, weak, strong forces), three quark mixing angles & a complex phase (in the CKM matrix), the Higgs mass & the vacuum expectation value (for the spontaneous symmetry breaking) and the QCD vacuum angle. However, some physicists do not include the last one [31].

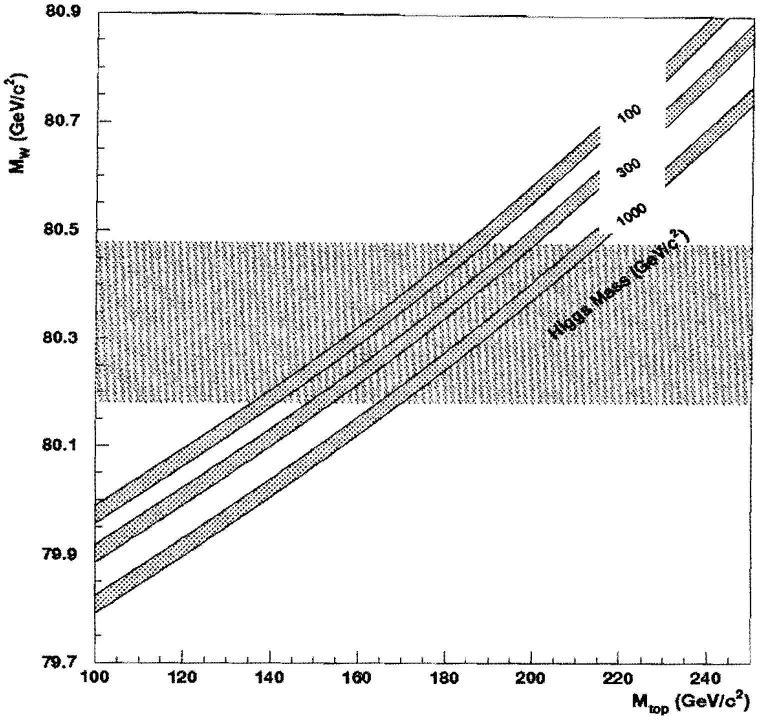

Figure 1.4: The Standard Model relation between m_t, M_W and M_H. The horizontal band represents the current world average of M_W measurements.

Secondly, if the masses of the W and the top quark are very precisely measured, we can predict the Higgs mass M_H theoretically [32]. (As an illustration, three possible Higgs mass curves are drawn on the M_W-m_t plane in Figure 1.4.) By restricting the allowed range of M_H, we will have a better chance to directly observe the Higgs boson, which is an pivotal ingredient of the Standard Model. While the Tevatron run I (1992-1996) data is not statistically sufficient to enable both the W and top mass measurements to achieve such a degree of precision, the method we currently use for the top quark mass measurement will still be useful for the next Tevatron run.

Chapter 2

Experimental Apparatus

Two major pieces of apparatus are used to conduct the experiment for the top quark study. One is the Tevatron collider which accelerates protons and antiprotons to a very high energy, and brings them into collision at two experimental sites. The other is the detector that detects particles emerging from the $p\bar{p}$ collision and thus helps us understand the underlying physics.

2.1 The Tevatron Collider

The Fermilab Tevatron [33, 34] is a synchrotron that accelerates protons and antiprotons simultaneously in opposite directions to 900 GeV, producing a center-of-mass collision energy of 1.8 TeV, the highest among hadron colliders.

A synchrotron typically consists of three major parts: RF (radio-frequency) cavities, bending magnets, and focusing/defocusing magnets. The alternating high voltages of the RF cavities accelerate charged beam particles every time they pass the cavities and synchronize them with the RF frequency. Dipole magnets are used to bend the orbit of the beam by the Lorentz force exerted on charged particles moving in a magnetic field. Quadrupole magnets are commonly used to keep the beam focused to ensure its stability and to maintain high particle density. Since a quadrupole magnet only focuses the beam in one transverse direction (typically either vertical or horizontal) and defocuses in the other orthogonal transverse direction, alternate quadrupoles having poles reversed are needed in order to achieve a net effect of focusing the entire cross-section of the beam. A synchrotron typically contains many repetitions of identical arrangements of dipoles and quadrupoles.

The confined beam in a synchrotron undergoes a periodic closed orbit motion while radiating energy in the form of electromagnetic wave (synchrotron radiation). The radiated energy per revolution per particle is [35]

$$\triangle E = \frac{4\pi}{3}\frac{e^2}{\rho}\beta^3\gamma^4 ,$$

where ρ is the synchrotron radius. When the charged particle of mass m is accelerated to a high energy E (so that $\beta \approx 1$), the radiated energy can be rewritten as

$$\triangle E \approx \frac{4\pi}{3}\frac{e^2}{\rho}\frac{E^4}{m^4c^8} .$$

It indicates that for electron and proton synchrotrons operated at the same energy, the electron machine would suffer ${m_p}^4/{m_e}^4 \approx 10^{13}$ times more radiation. This is why a large electron synchrotron like the Large Electron-Positron Collider (LEP) at CERN cannot achieve the same energy level as that of the Tevatron.

However, unlike composite protons, electrons are structure-less particles and all the energy carried by them can be used in the collisions. On the other hand, in hadron colliders, the partons that really participate in interactions only share part of the accelerated energy of hadrons.

The Tevatron itself is actually the final stage of a series of accelerators designed to boost proton and antiproton beams to 900 GeV and to achieve a peak luminosity[1] of $\approx 10^{31}\,\mathrm{cm}^{-2}\,\mathrm{s}^{-1}$. The whole accelerator system, shown in Figure 2.1, consists of the following components:

The Cockroft-Walton Pre-Accelerator: Negative hydrogen ions H^- are produced through a DC discharge of hydrogen atoms and accelerated to 750 KeV through a static potential.

The Linear Accelerator (LINAC): The H^- ions travels through a series of RF-driven alternating electric field, each separated by a drift region. This combination

---

[1] Luminosity is the area density of the colliding beams and is proportional to the number of head-on collisions in a unit time.

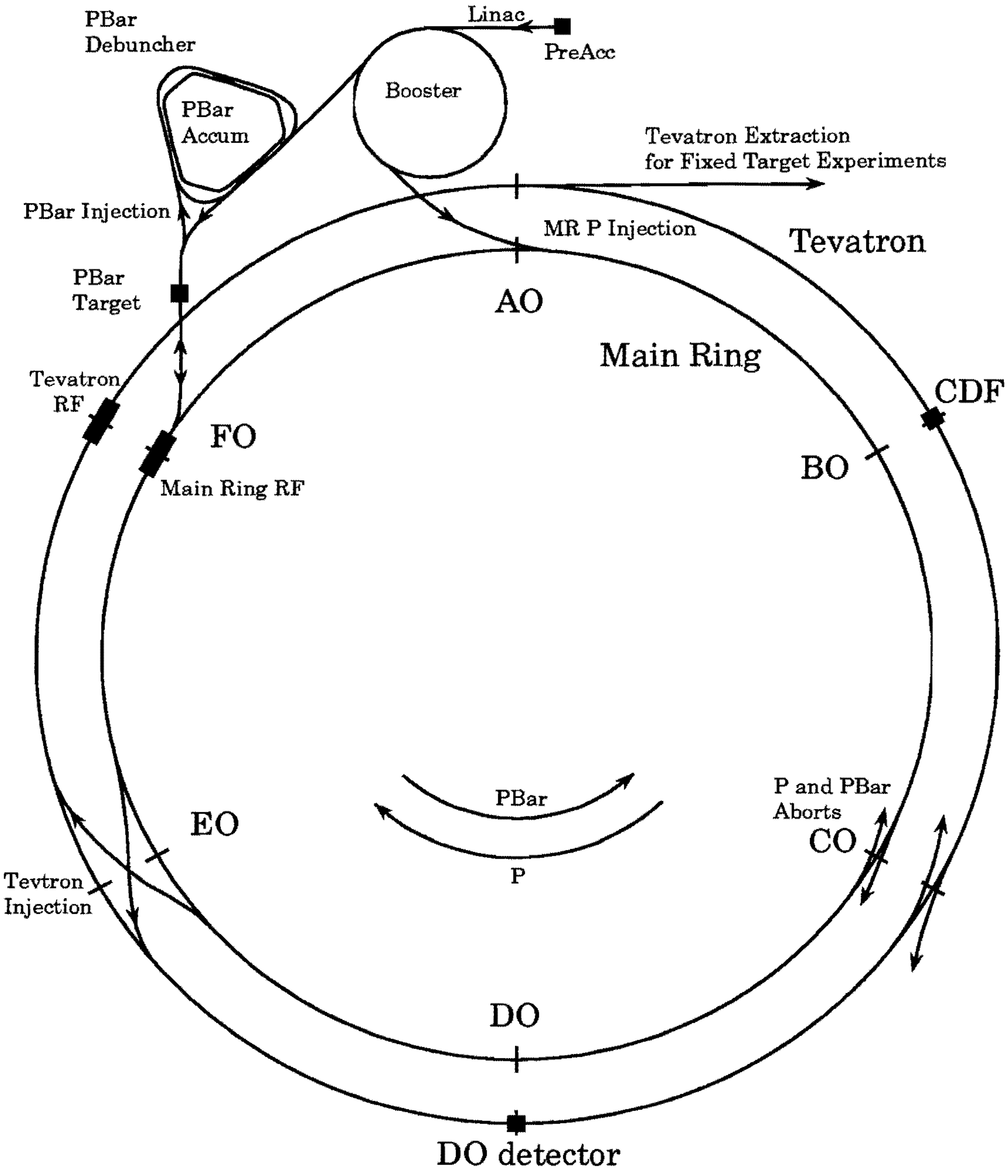

Figure 2.1: Layout of the Fermilab accelerator facility. Not drawn to scale.

accelerates the ions to 400 MeV over their 150-meter journey through the LINAC. Quadrupole magnets are embedded in the drift tubes to focus the H^- ion beam. A carbon foil right after the LINAC removes all the electrons from the H^- ions, leaving only protons.

The Booster: The Booster is a synchrotron with 96 combined function dipole/quadrupole magnets and 17 dual gap ferrite-tuned cavity resonators arranged around the 500-meter circumference. Since those beam particles not synchronous with the RF cavities will be lost along the beam pipe, protons naturally appear in bunches. There are 84 proton bunches in the Booster. The protons are accelerated to 8 GeV before being injected into the Main Ring.

The Main Ring: Being a large synchrotron with a one-kilometer radius, the Main Ring consists of 774 dipole magnets, 240 quadrupole magnets, and 18 dual gap RF cavities. Beam losses usually occur during the injection from the Booster and at a transition point (17.6 GeV) in the Main Ring acceleration process. In order to increase the number of particles per bunch, seven RF cavities with two different frequencies are used to coalesce several bunches into one. When the proton energy reaches 120 GeV, some proton bunches are directed to a nickel target to produce antiprotons. The antiprotons are cooled and accumulated in the Antiproton Storage Rings before being injected back into the Main Ring. Proton and antiproton bunches are further accelerated to 150 GeV before entering the Tevatron.

The Antiproton Storage Rings: A cylindrical lithium lens is placed immediately after the nickel target to focus the secondary particles produced in the target. A pulsed dipole magnet is used to select negatively charged particles of roughly 8 GeV. However, the produced antiprotons are still divergent in momentum and need to be "cooled"—reducing their momentum spread—before they can be further accelerated in the Tevatron. Two antiproton storage rings, the Debuncher and the Accumulator, are designed for cooling and accumulating antiprotons. In the Debuncher, a computer-coded RF voltage speeds up slower antiprotons and slows down the faster ones. Also the transverse motion of antiprotons is decreased by the "stochastic cooling"—deviated particles are first detected by sensors, and then signals are passed to kicker electrodes to correct the path of those particles. After being squeezed in momentum and size, antiprotons go to the Accumulator for further cooling and accumulation. The process takes several hours and hundreds of billions of antiprotons will be stored.

The Tevatron: This world-class synchrotron shares a tunnel with the Main Ring. Six bunches of protons (about 2×10^{11} protons per bunch) and six bunches of antiprotons (about 5×10^{10} antiprotons per bunch) are accelerated in opposite directions. The Tevatron has over a thousand superconducting magnets (774 dipoles and 216 quadrupoles) which are operated at 4.8° Kelvin. With the strong magnetic fields in these magnets, the Tevatron is able to keep very high energy beams within the ring. The proton and antiproton bunches are accelerated from 150 GeV at injection to 900 GeV. At two beam-crossing stations, BØ (where the CDF experiment resides) and DØ, the beam size is squeezed to about 1 mm^2 by special superconducting quadrupole magnets in order to maximize the luminosity. With beam crossings taking place every $3.5\,\mu$s, the Tevatron luminosity ranges from 10^{30} to $10^{31}\,\mathrm{cm}^{-2}\,\mathrm{s}^{-1}$.

2.2 The DØ Detector

The DØ [36] detector is a general purpose detector for a collider experiment. It features good electron and muon identification capabilities, and excellent calorimetry which results in good measurements of electrons, photons, jets and missing transverse energy ($\not\!\!E_T$). In contrast to other collider detectors, the DØ detector does not contain a tracking solenoid which is usually used for momentum measurements and particle identification. Instead, it relies on its good calorimetry to measure the energies of high p_T objects and to identify electrons and photons.

The whole detector can be divided into three parts: the central tracker, the calorimeter, and the muon spectrometer. We will begin with the definition of the coordinate system and then proceed to each of the three parts of the detector.

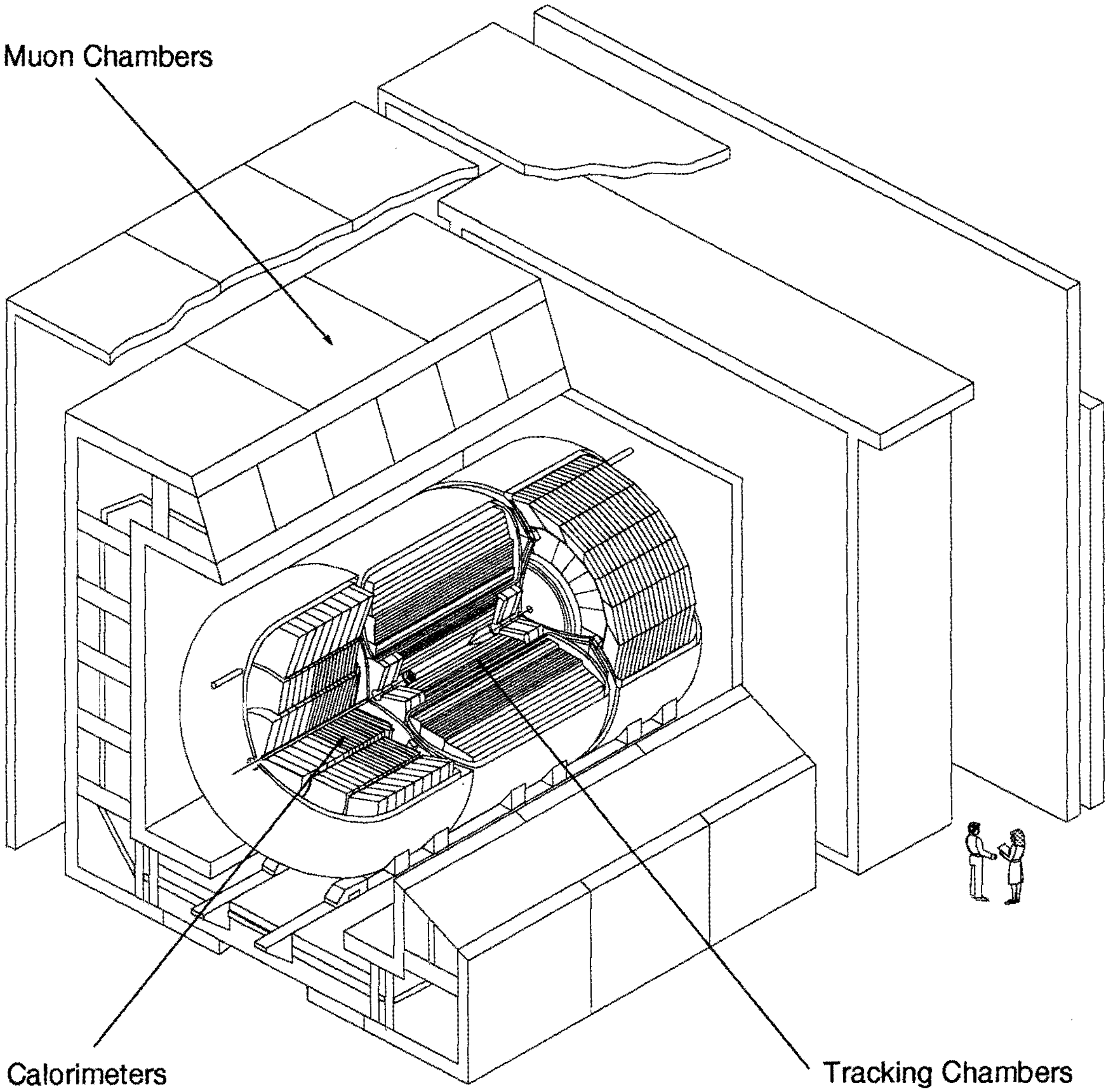

Figure 2.2: Isometric view of the DØ detector.

2.3 Coordinate Convention

Although the Cartesian coordinate system is rarely used in describing detector components or scattered objects, it is the basis for other widely-used coordinates such as η and ϕ. The z-axis of the Cartesian coordinates is defined as the direction of the proton beam, and the y-axis is upward. Accordingly, the x-axis is fixed by the right-hand rule.

The azimuthal ϕ and polar θ angles are coordinates in the spherical coordinate system: ϕ is the angle from the x-axis to the referred vector projected onto the plane transverse to the beam (the transverse plan), and θ is the angle between the referred vector and the z-axis.

The polar angle θ can be mapped to a more convenient coordinate, the pseudorapidity η defined as

$$\eta \equiv -\ln(\tan\frac{\theta}{2}) \ .$$

The reason η is more commonly used than θ is that in the high energy limit, $m/E \to 0$, η approximates the true rapidity

$$y \equiv \frac{1}{2}\ln\left(\frac{E+p_z}{E-p_z}\right) \ .$$

Using the pseudorapidity η, the invariant cross section of interactions can be readily measured by:

$$E\frac{d^3\sigma}{dp^3} = \frac{1}{2\pi}\frac{d^2\sigma}{p_T dp_T dy} \simeq \frac{1}{2\pi}\frac{d^2\sigma}{E_T dE_T d\eta} \ ,$$

where p_T is the transverse momentum of the particle, $p_T = p\sin\theta$, and is measured by the energy deposited in the calorimeter as $E_T = E\sin\theta$.

2.4 Central Tracker

The central tracker is located in the innermost section of the detector. It has the following functions: (1) Reconstruct charged particle tracks, (2) Determine the interaction vertex (collision point), (3) Measure the ionization of charged particle tracks to distinguish single charged particles from the photon conversion $\gamma \to e^+e^-$. There are three types of drift chambers [37, 38, 39] in the central tracker: a Vertex

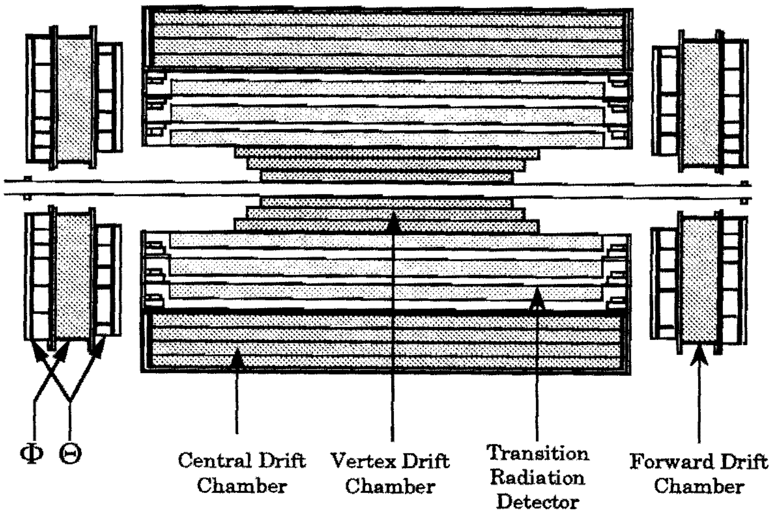

Figure 2.3: Sideview (perpendicular to the z-axis) of the DØ central tracker. The Φ and Θ modules of the FDC are designed to measure ϕ and θ respectively.

Drift Chamber (VTX), a Central Drift Chamber (CDC), and two Forward Drift Chambers (FDC).

Basically a drift chamber contains many anode and cathode wires that create regions of approximately uniform electric field, and a gas—used as an ionization medium—which fills the volume. When a charged particle passes through the volume, the ionization electrons in the gas will be drawn to the anode wires. By measuring their drift time, the spatial position of the charged particle can be determined.

Another tracking subdetector is a transition radiation detector (TRD) which utilizes the radiation emitted by relativistic particles when they pass through a junction between two dielectric media to distinguish charged pions and electrons. The arrangement of the central tracker is shown is Figure 2.3.

The whole system provides charged particle tracking in the region $|\eta| < 3.2$ with the resolutions $\delta\phi \approx 2.5\,\mathrm{mrad}$ and $\delta\theta \approx 28\,\mathrm{mrad}$. From the measurements of tracks, the interaction vertex can be determined with a resolution of $\delta z \approx 8\,\mathrm{mm}$.

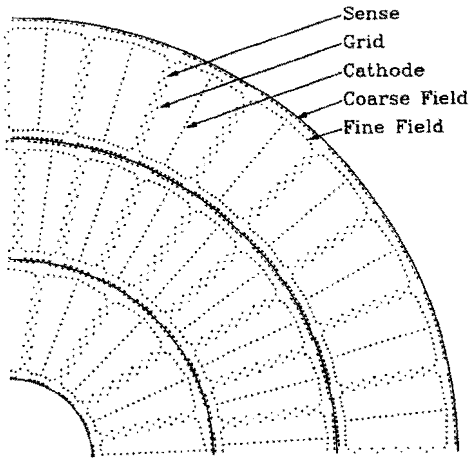

Figure 2.4: r-ϕ view of a quadrant of the VTX chamber.

2.4.1 Vertex Chamber (VTX)

The vertex chamber [40] has an inner radius of 3.7 cm (just outside the beam pipe) and an outer radius of 16.2 cm. It consists of three layers of concentric cells, as shown in Figure 2.4. The innermost layer has 16 cells in azimuth and the outer two layers have 32 cells each. Adjacent sense wires are staggered by $\pm 100\,\mu$m to resolve left-right ambiguities. The sense wires have a resistivity of 1.8 kΩ/m and provide a measurement of the z-coordinate from readouts at both ends. The r-ϕ position of a hit is determined from the drift time. The r-ϕ resolution in the VTX is $\approx 60\,\mu$m and the z resolution is $\approx 1.5\,$cm.

2.4.2 Central Drift Chamber (CDC)

The central drift chamber [41] resides between the TRD and the central calorimeter and provides coverage for tracks at large angles. The CDC is a cylindrical shell of length 184 cm and radii between 49.5 and 74.5 cm. It consists of four concentric rings of 32 azimuthal cells per ring, as shown in Figure 2.5. In each cell, there are 7 equally spaced sense wires at the same ϕ coordinate. These wires are parallel to the z-axis and read out at one end to measure the ϕ coordinate of a track. There are two delay lines embedded in the inner and outer shelves of each cell. The delay lines propagate

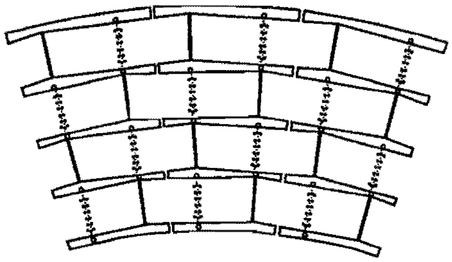

Figure 2.5: End view of three segments of the central drift chamber.

signals induced from the nearest neighboring anode wire. The z coordinate of a track can be measured by the difference of signal arrival times at the two ends. The r-ϕ resolution is $\approx 180\,\mu$m and the z resolution is $\approx 3\,$mm.

2.4.3 Forward Drift Chambers (FDC)

The forward drift chambers [42] are located at either end of the concentric barrels of the VTX, TRD, and CDC and just before the entrance wall of the end calorimeters. They extend the coverage for charged particle tracking down to $\theta \approx 5^\circ$ with respect to both emerging beams. Each FDC package consists of three separate chambers, as shown in Figure 2.6. The Φ module has radial sense wires and measures the ϕ coordinate. It is sandwiched between a pair of Θ modules whose sense wires measure the θ coordinate. The geometric composition of the FDC cells is more complicated than that of the CDC, but the operating principle is similar and the chamber gas is the same. The position resolution is about $200\,\mu$m for r-ϕ and $300\,\mu$m for r-θ.

2.4.4 Transition Radiation Detector (TRD)

The transition radiation detector [43] is located between the VTX and CDC. It provides independent electron identification in addition to that given by the calorimeter and the tracking chambers. When highly relativistic charged particles ($\gamma > 10^3$) traverse boundaries between media with different dielectric constants, transition radiation X-rays are produced on a cone with an opening angle of $1/\gamma$. The energy

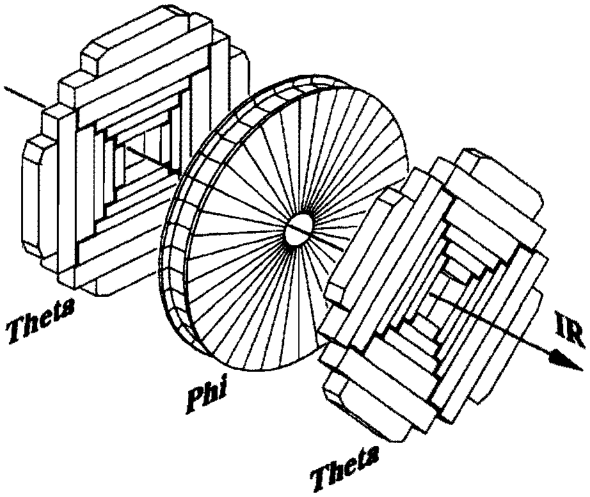

Figure 2.6: The Θ and Φ modules of the forward drift chamber.

flux of the radiation is proportional to the γ. These characteristics can be used to distinguish particles which have similar energies but different masses.

The TRD uses many dielectric (polypropylene) foils with gaps (nitrogen gas) between them to produce the X-ray radiation. A radial-drift proportional wire chamber acts as the X-ray conversion medium and also collects the resulting charges which drift radially outwards to the sense wires. The magnitude and the arrival time of charge clusters are used to distinguish electrons from hadrons. Due to its low efficiency, this detector is not used in many analyses, including those involving the top quark.

2.5 Calorimeter

Because of the absence of a tracking magnet, we rely heavily on the calorimeter to identify electrons, photons and jets, and to reconstruct their momenta. In addition, all detected energies in the calorimeter are used to measure the transverse energy imbalance caused by the neutrinos.

The DØ calorimeter is a sampling calorimeter. A typical configuration of the sampling calorimeter is a stack of dense metallic plates as energy absorbers, inter-

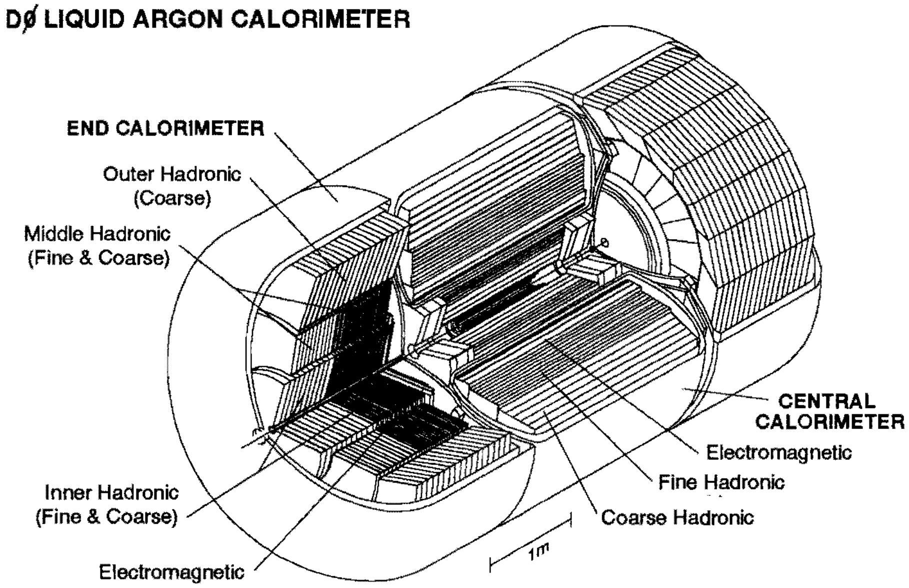

Figure 2.7: A cutaway view of the DØ calorimeter.

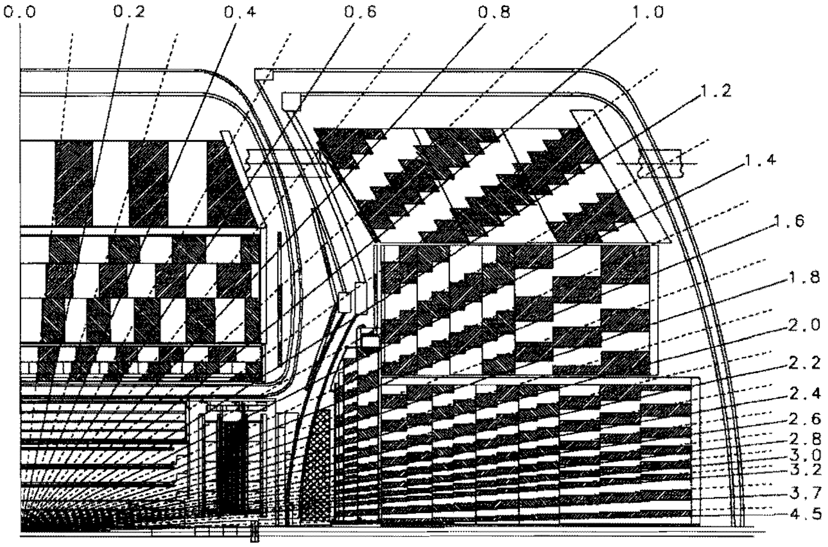

Figure 2.8: Sideview of a quarter of the CC and EC calorimeters showing the transverse and longitudinal segmentation. The shading pattern indicates distinct cells. The rays indicate the pseudorapidity intervals seen from the center of the detector.

leaved with planes of sensitive material where the ionization energy is measured. The measured energy in the sensitive layers only accounts for a small fraction of the total ionization energy, usually ~1-10%, but this fraction is fixed for various total energies. Therefore, through proper calibration, the whole electron or jet energy can be determined from a sampling calorimeter. The DØ calorimeter uses liquid argon as the sensitive material, and uranium and copper as the absorbers.

There are two types of particle showers in the calorimeter: the electromagnetic showers which are produced by an energetic electron or photon, and the hadronic showers, which usually occur in the outer part of the calorimeter, are induced by incident hadrons.

The electromagnetic shower is a cascade of electrons, positrons, and photons as a result of bremsstrahlung and e^+e^- pair production—high energy e^- or e^+ radiates photons as they travel through calorimeter material, and photons in turn create e^+e^- pairs of lower energy. The number of particles increases exponentially until electrons reach the critical energy, at which point electrons lose the same amount of energy by radiation and ionization. After that, the number of particles decreases and their energies gradually dissipate through the process of ionization.

Unlike electromagnetic showers, the physical processes that cause the propagation of hadronic showers are mainly strong interactions between hadrons and nuclei. A considerable fraction of the hadron energy is transferred to the nuclei and causes the production of secondary hadrons, which in turn produce more hadrons. This cascade process begins to stop when the energies of the secondary hadrons are small enough to be exhausted by ionization or to be absorbed in a nuclear process. Neutral pions (π^0) may be produced as secondary hadrons and subsequently decay into two photons which give rise to an electromagnetic shower within a hadronic one.

Hadronic showers tend to be more spread out laterally and more penetrating longitudinally than electromagnetic showers, and their larger variety of interaction processes also implies a larger fluctuation in the energy measurement.

The longitudinal development of the electromagnetic showers is characterized by the radiation length (X_0)—the mean distance over which an electron loses all but $1/e$ of its energy by bremsstrahlung. The length scale appropriate for hadronic showers is the nuclear interaction length (λ_I)—the distance over which the probability that an incident hadron does not interact with calorimeter material is $1/e$. Both the radiation length and the nuclear interaction length depend on the material of the calorimeter and can be approximated by the empirical formulae[2] [44]:

$$\begin{aligned} X_0 &\approx \frac{716.4\,\mathrm{A}}{\mathrm{Z(Z+1)\ln(287/\sqrt{Z})}}\ \mathrm{g/cm^2}\ \text{and} \\ \lambda_I &\approx 35\,\mathrm{A}^{1/3}\,\mathrm{g/cm^2}, \end{aligned}$$

where Z and A are respectively the atomic number and the atomic weight of the medium. Typically $\lambda_I \gg X_0$. Heavy metals such as iron ($X_0 = 1.76\,\mathrm{cm}$, $\lambda_I = 16.76\,\mathrm{cm}$) or uranium ($X_0 = 0.32\,\mathrm{cm}$, $\lambda_I = 10.5\,\mathrm{cm}$) are usually used to minimize the size of the calorimeter.

The DØ liquid argon calorimeter consists of a central calorimeter (CC) and two end calorimeters (EC), each contained within a steel cryostat, and each including an inner electromagnetic (EM) section, a fine hadronic (FH) section, and a coarse hadronic (CH) section. The intercryostat detector (ICD), made of scintillator tiles, is installed between the CC and EC cryostats to improve the energy resolution for jets in the intercryostat region.

In each cryostat of the DØ calorimeter, the EM section is roughly 21 radiation lengths deep, and is divided into four longitudinal layers in order to provide shower profile information. The hadronic sections cover 7 to 9 nuclear interaction lengths and are divided into four (CC) or five (EC) layers. The calorimeter is segmented into $\Delta\eta \times \Delta\phi = 0.1 \times 0.1$ towers (see Figure 2.8) except that the third layer of the EM section, where the maximum of electromagnetic showers is expected, is segmented into cells with $\Delta\eta \times \Delta\phi = 0.05 \times 0.05$.

The performance of the calorimeter has been studied by using electron and pion beams with energies between 10 and 150 GeV targeted on an EM and a hadronic calorimeter module [36, 45] at a test beam facility. The study concludes electrons

---

[2] To convert to a length unit, one must divide the the X_0 or λ_I number by the density of the medium.

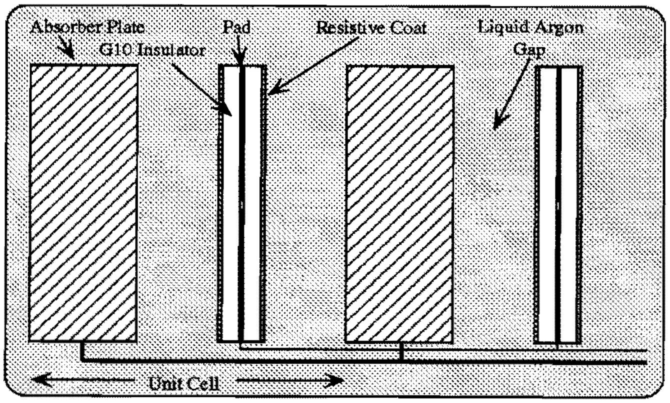

Figure 2.9: Schematic view of a unit cell of the D0 liquid argon calorimeter.

and pions have the following energy resolutions:

$$
\begin{aligned}
\frac{\sigma(E)}{E} &= \frac{16\%}{\sqrt{E(\,\mathrm{GeV})}} \oplus 0.3\% \quad \text{for electrons,} \\
\frac{\sigma(E)}{E} &= \frac{41\%}{\sqrt{E(\,\mathrm{GeV})}} \oplus 3.2\% \quad \text{for pions.}
\end{aligned}
$$

2.5.1 Central Calorimeter (CC)

The central calorimeter (CC) covers the pseudorapidity range $|\eta| \lesssim 1$. It comprises three concentric cylindrical shells: 32 EM modules in the inner ring, 16 FH modules in the surrounding ring, and 16 CH modules in the outer ring. In order to reduce the energy loss in cracks, the EM, FH, and CH module boundaries are properly arranged so that no projective ray encounters more than one intermodule gap. The CCEM modules have four longitudinal sections of 2.0, 2.0, 6.8, and 9.8 X_0. The CCFH modules contain three longitudinal sections of 1.3, 1.0, and 0.9 λ_I. The CCCH modules contain only one depth segment of 3.2 λ_I.

A unit cell of the calorimeter modules typically consists of liquid argon gaps, absorber plates, and signal boards, as shown in Figure 2.9. Each signal board has a surface coated with a resistive epoxy. The electric field in the cell is established by connecting the resistive surfaces of the boards to a high positive voltage (2.0-2.5 kV) and grounding the metal absorber plates. The electron drift time across the 2.3 mm gap is $\approx 450\,\mathrm{ns}$.

2.5.2 End Calorimeters (EC)

The two mirror-image end calorimeters (ECs) extend the coverage to $|\eta| \approx 4$. Each EC contains one EM module, one inner hadronic module (IH), and 16 middle and outer hadronic (MH and OH) modules. The azimuthal boundaries of the MH and OH modules are offset to avoid through-going cracks. The ECEM modules contain four readout sections of 0.3, 2.6, 7.9, and 9.3 X_0. The material of the cryostat wall brings the total absorber for the first section up to about 2 X_0. The fine hadronic part of the ECIH has four readout sections of 1.1 λ_I for each, and the coarse hadronic part has a single readout section of 4.1 λ_I. Each of the ECMH modules contains four uranium fine-hadronic sections of about 0.9 λ_I and a single stainless steel coarse-hadronic section of 4.4 λ_I. The ECOH are all stainless steel coarse-hadronic modules with the absorber plates inclined at an angle of about 60° with respect to the z-axis.

2.5.3 Intercryostat Detectors and Massless Gaps

Two scintillation counter arrays, called intercryostat detectors (ICD), were built in the region $0.8 \leq |\eta| \leq 1.4$ to correct for the energy deposited in the uninstrumented cryostat walls. Each ICD consists of 384 scintillator tiles of size $\Delta\eta = \Delta\phi = 0.1$ exactly matching the liquid argon calorimeter cells. In addition, separate readout cells called massless gaps are installed in both the CC and EC calorimeters. Each massless gap consists of three liquid argon gaps with two readout boards without any absorber plates. These massless gaps together with the ICD provide an approximation to the sampling of EM and hadronic showers.

2.6 Muon Spectrometer

The outermost part of the DØ detector is the muon spectrometer [46] which consists of five solid iron toroidal magnets and layers of proportional drift tube chambers

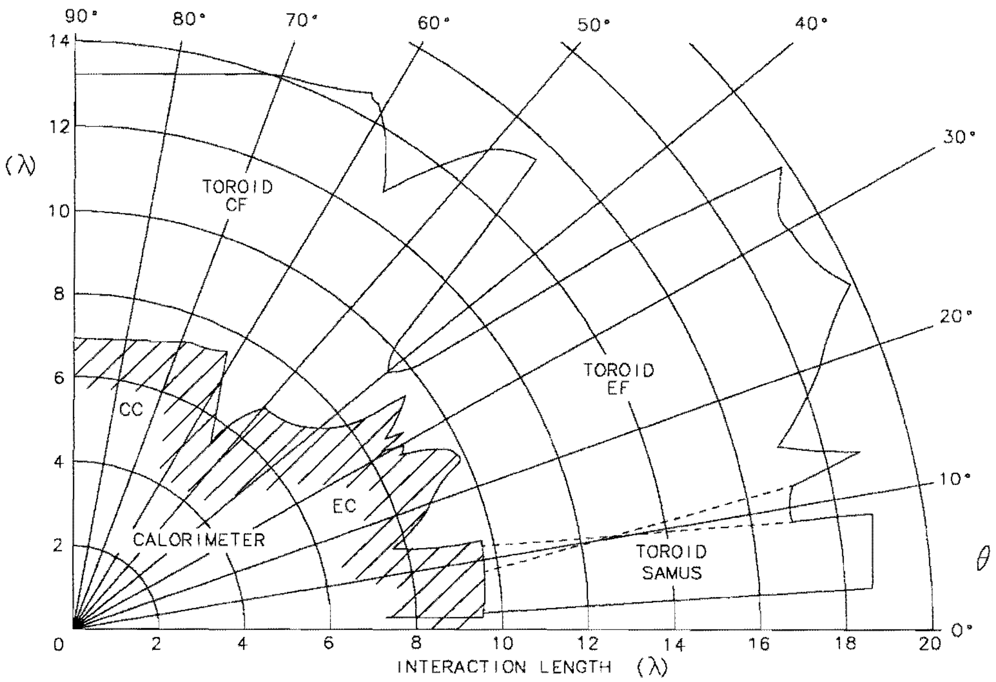

Figure 2.10: The detector thickness in interaction lengths as a function of the polar angle (θ).

(PDT). The toroids provide strong magnetic fields to bend the muon trajectory and the drift chambers measure the muon track. Both are indispensable for identifying muons and measuring their momenta (p).

The calorimeter is designed to contain electromagnetic and hadronic showers (see Figure 2.10). The possibility that a π or a K from a hadronic shower traverses the muon chambers (punch-through) is negligible. Background in the muon chambers mainly comes from cosmic muons and beam remnants.

The whole muon spectrometer can be divided into two systems: the WAMUS and the SAMUS. In the WAMUS, a central toroid (CF) covers the pseudorapidity region $|\eta| \leq 1$ and two end toroids (EFs) cover $1 < |\eta| \leq 2.5$. Two SAMUS toroids, fitting in the central holes of the EF toroids, extend the coverage to $2.5 \leq |\eta| \leq 3.6$.

The resolution of the muon momentum measurement is limited largely due to the multiple Coulomb scattering in the toroids and the hit position resolution in the drift

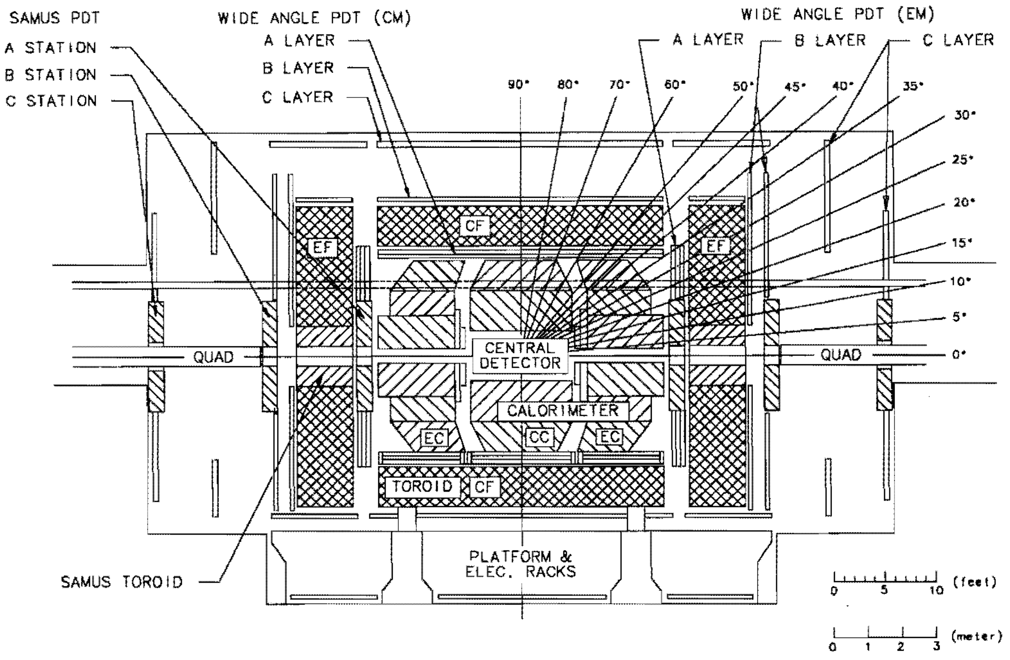

Figure 2.11: Sideview of the DØ detector including the muon spectrometer.

chambers. The resolution[3] for $1/p$ is approximately Gaussian and parametrized as [47]:

$$\sigma\left(\frac{1}{p}\right) = \frac{0.18\,(p-2)}{p^2} \oplus 0.008 \quad \text{where } p \text{ is in GeV}/c.$$

2.6.1 Wide Angle Muon System (WAMUS)

The wide angle muon system (WAMUS) consists of one CF and two EF toroids and three layers of PDT chambers as shown in Figure 2.11. The A layer of PDT chambers are between the CF and EF toroids, and the B and C layers are outside the EF toroids. In order to have a good measurement of the muon track, the B and C layers are separated by more than one meter.

The WAMUS PDTs are formed from aluminum extrusion unit cells as shown in Figure 2.12. A transverse offset between planes of chambers resolves the left-right drift time ambiguity. Two cathode-pad strips are inserted into the top and bottom

---

[3] This was determined by comparing $Z \to \mu^+\mu^-$ data with Monte Carlo events where the hit position resolution was degraded until the width of the $\mu^+\mu^-$ invariant mass matched the data.

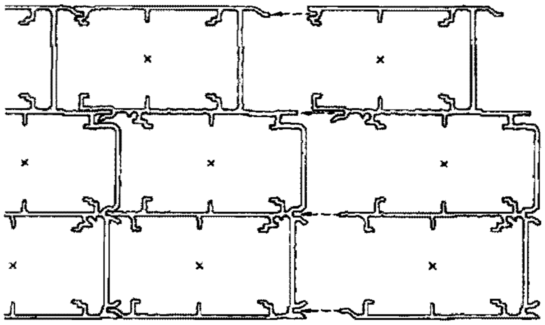

Figure 2.12: The end-view of PDT chambers.

of each unit cell and the anode wire is held near the center of the cell, as shown in Figure 2.13. The maximum drift distance is 5 cm.

The chamber wires are oriented parallel to the primary magnetic field to give accurate measurement of the bend coordinate of muon tracks. The coordinate (ξ) along the wire direction is measured by a combination of cathode-pad signals and timing information from the anode wires. The resolutions of coordinate measurements and other parameters of the WAMUS are summarized in Table 2.1.

2.6.2 Small Angle Muon System (SAMUS)

The small angle muon system (SAMUS) consists of two SAMUS toroids, each inserted into the center hole of EF toroid, and a collection of PDT chambers. The chambers cover the pseudorapidity region $2.5 \leq |\eta| \leq 3.5$ and are arranged into three stations. The A station precedes the SAMUS toroid and the B and C stations are after the toroid. Each station consists of three doublets of proportional drift tubes oriented in x, y, and u (u being at 45° with respect to x and y) directions. Further details about the SAMUS are listed in Table 2.1.

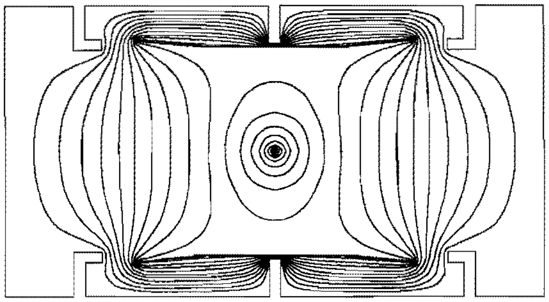

Figure 2.13: A unit cell of PDT chambers with the equipotential lines shown. The cathode-pad strips are on the top and bottom and the anode wire at the center.

	WAMUS	SAMUS
Pseudorapidity coverage	$\|\eta\| \leq 1.7$	$1.7 \leq \|\eta\| \leq 3.6$
Magnetic field	2 T	2 T
Number of chambers	164	6
Interaction lengths	13.4	18.7
Bend view resolution	±0.9 mm	±0.35 mm
Non-bend (ξ) resolution	±10 mm	±0.35 mm
Gas composition	Ar 90%, CF_4 6%, CO_2 4%	CF_4 90%, CH_4 10%
Avg. drift velocity	6.5 cm/μs	9.7 cm/μs
Anode wire voltage	+4.56 kV	+4.0 kV
Cathode pad voltage	+2.3 kV	—
Number of cells	11,386	5308

Table 2.1: Muon System Parameters.

2.7 Trigger and Data Acquisition

When the collider is running, there are hundreds of thousands of collisions occurring per second within the DØ detector. However, most of the collisions are not of interest. In order to select interesting events (at a rate of a few events per second) from such a large amount of collisions, we need a trigger and data acquisition system. The DØ trigger has three levels of increasingly sophisticated event characterization.

2.7.1 Level 0

The Level 0 trigger [36, 48] registers the occurrence of inelastic collisions and serves as the luminosity monitor for the experiment. It uses two hodoscopes of scintillation counters mounted on the front surfaces of the end calorimeters. These hodoscopes have an array of counters inscribed in a 45 cm radius circle to give partial coverage for the pseudorapidity range $1.9 \leq |\eta| \leq 4.3$ and nearly full coverage for $2.3 \leq |\eta| \leq 3.9$.

The z-coordinate of the interaction vertex (collision point) can be roughly measured from the the difference in the arrival time of particles to the hodoscopes at both ends. This information is used for the transverse energy (E_T) measurements at the subsequent trigger levels.

At a luminosity of $\mathcal{L} = 5 \times 10^{30}\,\mathrm{cm}^{-2}\mathrm{s}^{-1}$, the Level 0 rate is about 150 kHz. In the case of multiple interactions in one crossing (per $3.5\,\mu$s), the time difference information is ambiguous and a flag is set to identify these events.

2.7.2 Level 1

Level 1 [36, 49] is a collection of hardware trigger elements arranged in a flexible software driven architecture that allows for easy modification. It gathers digital information from each of the specific Level 1 trigger devices (which are connected to the calorimeter, muon chambers, and TRD) and selects a particular event for further examination.

Specific trigger selection is performed by a two-dimensional AND-OR network. The 256 latched bits (called AND-OR input terms) which carry specific pieces of detector information form one set of inputs to the AND-OR network. The 32 orthogonal AND-OR lines corresponding to 32 specific Level 1 triggers are the outputs of the AND-OR network. Each of these triggers is defined by a pattern indicating, for every AND-OR input term, whether that term is required to be asserted, negated or ignored. Satisfaction of one or more specific trigger requirements results in a request for the readout of the full event data by the data acquisition hardware if free from front-end busy restrictions or other vetoes.

Many Level 1 triggers operate within the $3.5\,\mu$s interval between beam crossings and thus contribute no deadtime. Others require several bunch crossing times to complete and are referred to as Level 1.5 triggers [50, 51]. The rate of successful Level 1 triggers is about 200 Hz; after the action by Level 1.5 triggers, the rate is reduced to below 100 Hz.

2.7.3 Level 2

The Level 2 system is a farm of 50 parallel nodes connected to the detector electronics and triggered by a set of eight 32-bit wide high-speed (40 MB/s) data cables. Each node consists of a VAXstation processor coupled via a VME bus adaptor to multiport memory boards (for receiving data) and an output memory board.

The event-filtering process in each node is built around a series of software tools. Each tool has a specific function related to particle identification or event characteristics. For instance, there are tools for identifying or computing jets, muons, calorimeter EM clusters, tracks associated with calorimeter clusters, and missing E_T. Some other tools are designed to recognize noise or background conditions.

The rate of successful Level 2 events is about 2 Hz. These events are passed on to the host computer for run-time monitoring and recording on 8mm tapes for permanent storage.

Chapter 3

Event Reconstruction and Simulation

Although the $p\bar{p}$ collision energy at Tevatron makes the top quark production possible, the probability of a top quark being produced in a particular collision is remarkably small. As mentioned in Chapter 1, the top quark is most likely produced together with its antiparticle at the Tevatron, and the cross section for the production is on the order of pico-barn (pb). In other words, among the inclusive $p\bar{p}$ inelastic collisions (the cross section $\approx 70\,\text{mb}$), the $t\bar{t}$ events account for less than one part in ten billion.

How to choose the signal events from trillions of collisions is undoubtedly a very demanding challenge in analyses involving the top quark. Enormous efforts have been made to efficiently select the signal and, at the same time, effectively suppress the background. Strictly speaking, the event selection begins with the triggering—when the decision to keep or discard the event is made. The offline analysis starts with the event reconstruction in which the final state particles which emerge from the collision are identified.

As a prelude to a complex event selection algorithm, this chapter will introduce how various objects—electrons, photons, muons, jets and $\not{E}_T$ are reconstructed and identified. In addition, we will describe how signal and background events are simulated, since, as it will be seen later, proper event simulation is very important for the top mass measurement.

3.1 Particle Identification

The identification and reconstruction algorithms of electrons, photons, muons, jets, and the missing transverse energy $\not{E}_T$ are described below.

3.1.1 Electrons

The first step in electron identification is the formation of electromagnetic clusters using a "nearest neighbor" algorithm—adjacent calorimeter towers with significant energy deposition are grouped as a cluster, and the cluster centroid is computed from the energy weighted cell coordinates. If most of the cluster energy is contained in the EM calorimeter and in the central tower, and there is a track in the drift chambers pointing to the cluster, then the cluster becomes an electron candidate.

However, a large fraction of the electron candidates is background, which mainly comes from two sources—low energy charged hadrons spatially overlapping with energetic photons from π^0 or η decays, and isolated photons that converted to e^+e^- in the tracking chambers. Therefore, more efforts are needed to identify electrons.

To develop algorithms to reject electron backgrounds, we first establish both electron and background samples from data. The electron sample is selected from Z $\rightarrow e^+e^-$ events where two electron candidates have an invariant mass around the Z mass peak. The background sample is more readily available since more than 95% of the electron candidates are "fake" electrons (those that are not from either W or Z). We select events where there is only one electron candidate and a low $\not{E}_T$ (so the electron is not likely to come from W $\rightarrow e\nu$) to be our background sample.

Studies show that with information from the central tracker and the calorimeter, there are four attributes of electrons that distinguish themselves from their background, as shown in Figure 3.1. These attributes are as follows:

- **EM energy fraction**: The EM calorimeter contains almost all of the electron energy, while charged hadrons deposit only about 10% of their energy in the electromagnetic section of the calorimeter. Therefore the EM energy fraction of the cluster, f_{EM}, serves as a powerful discriminant against charged hadrons.

- **Shower shape**: Electromagnetic showers can be characterized by the fraction of the cluster energy deposited in each layer of the calorimeter. Based on Monte Carlo electrons with energies ranging between 10 and 150 GeV, a covariant matrix (H-matrix) is constructed to represent the correlation between the energy depositions in individual layers [53]. For an electron candidate, a χ^2 is computed from the observed shower shape and the covariant matrix (expected shower shape), so that the lower the χ^2 the more the candidate cluster resembles an electron shower.

- **Cluster-track match**: The π^0 and η meson background can be reduced by demanding a good spatial match between the cluster and a charged particle track in the tracking detectors. The track match significance is defined as:

$$\sigma_{trk} = \sqrt{\left(\frac{\triangle\phi}{\delta_{\triangle\phi}}\right)^2 + \left(\frac{\triangle z}{\delta_{\triangle z}}\right)^2} \quad \text{for CC candidates,}$$

$$\sigma_{trk} = \sqrt{\left(\frac{\triangle\phi}{\delta_{\triangle\phi}}\right)^2 + \left(\frac{\triangle r}{\delta_{\triangle r}}\right)^2} \quad \text{for EC candidates,}$$

  where $\triangle\phi$ and $\triangle z$ are the azimuthal mismatch and the z-coordinate (beam direction) mismatch respectively, $\triangle r$ is the radial mismatch transverse to the beam, and $\delta_{\triangle\phi}$, $\delta_{\triangle z}$, $\delta_{\triangle r}$ are their resolutions respectively. The smaller the σ_{trk}, the better the track-cluster match.

- **Track ionization**: Due to the absence of a central magnetic field, e^+e^- pairs from photon conversions before or in the tracking chambers are not bent apart and often are reconstructed as a single charged particle. However, in the tracking chambers the ionization energy per unit length (dE/dx) of a e^+e^- pair is about twice that of a single charged particle. In Figure 3.1, the dE/dx distribution for real electrons has only one peak, but the distribution for the background has a two-peak structure where the second peak results from the photon conversion.

Using these four variables, we define an electron likelihood [54] and make a cut on the likelihood to quantitatively identify electrons. The likelihood function is built

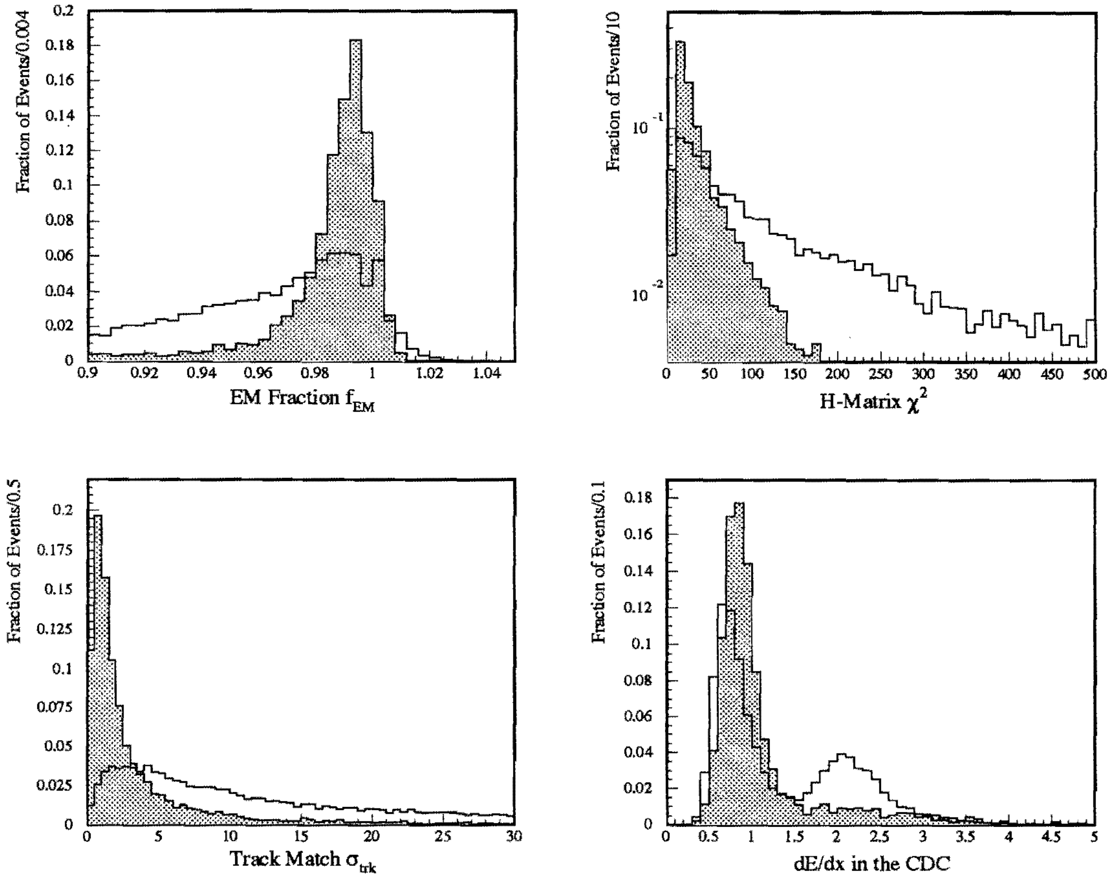

Figure 3.1: The distributions of the four variables used in computing electron likelihood. The shaded histograms are of the Z $\rightarrow e^+e^-$ electron sample and the unshaded histograms are of the electron background.

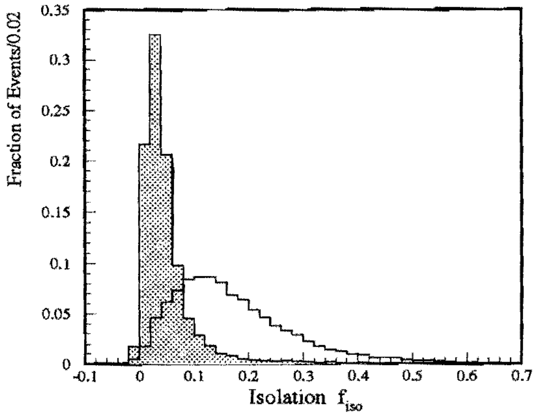

Figure 3.2: The distribution of the isolation parameter f_{iso} for the Z $\rightarrow e^+e^-$ electron sample (shaded) and the background sample (unshaded).

on the probability density distributions of the four variables: $P_1(f_{EM}|h)$, $P_2(\chi^2|h)$, $P_3(\sigma_{trk}|h)$ and $P_4(dE/dx|h)$, where $h = e$ for real electrons and $h = b$ for background. Since those four variables are only weakly correlated, the probability density function at the 4-dimensional phase space point $X = (f_{EM}, \chi^2, \sigma_{trk}, dE/dx)$ is approximately

$$P(X|h) \approx P_1(f_{EM}|h) \cdot P_2(\chi^2|h) \cdot P_3(\sigma_{trk}|h) \cdot P_4(dE/dx|h).$$

The electron likelihood at the observed point x for a particular electron candidate is defined as

$$\mathcal{L}_e(x) \equiv \frac{P(X|b)}{P(X|e)} \ .$$

In selecting electrons for our analysis, we require $\mathcal{L}_e < 0.25$ if the cluster is in the CC, and $\mathcal{L}_e < 0.30$ if the cluster is in the EC.

The electron from b or c quark decays is boosted in the direction of motion of the parent quark and is very often adjacent to the jet resulting from the parent quark. In the case of $t\bar{t}$ events, the electron from the W decay is generally isolated from jets except occasional coincidental spatial overlap. Therefore we define an isolation parameter f_{iso}:

$$f_{iso} = \frac{E_{total}(R = 0.4) - E_{EM}(R = 0.2)}{E_{EM}(R = 0.2)} \ ,$$

where $E_{total}(R)$ ($E_{EM}(R)$) is the total (EM) calorimeter energy in the cone of radius

$R = \sqrt{\Delta\eta^2 + \Delta\phi^2}$. Figure 3.2 shows the f_{iso} distribution for the electron and the background samples. The requirement for electrons is $f_{iso} < 0.1$.

3.1.2 Photons

The signature of a photon in the EM calorimeter is identical to that of an electron, however, there is no charged particle track pointing to the EM cluster of a photon. Since isolated photons are unlikely to occur in the $t\bar{t}$ event, we reject the events in which any photon is identified. The identification of a photon requires the following conditions:

- **EM energy fraction**: the fraction must be greater than 90%.
- **Shower shape**: the H-matrix $\chi^2 < 100$.
- **Isolation**: $f_{iso} < 0.1$.

3.1.3 Muons

Muons are reconstructed as tracks in the muon PDT chambers. The transverse momentum of the muon is computed from the deflection in the magnetized toroid. Sources of muon background are cosmic muons, the combinatoric errors in track reconstruction, and the random hits from the beam spray. To identify muons, several measures are taken to minimize the background.

First, to reject cosmic muons the muon track is required to be able to trace back to the interaction vertex with a small impact parameter. Furthermore the PDT hits must coincide with the beam crossing time. Secondly, to reject the background from random hits, we require that at least five PDT planes have hits along the track. A typical muon track has hits on 7 to 10 planes. Thirdly, in an attempt to reduce the hadronic punchthrough, we require that the track have enough hits in the two PDT layers behind the toroids.

There is a general requirement on the track reconstruction quality which blends in the number of muon modules with recorded hits, the impact parameters, and the hit residuals.

A muon typically deposits ~1-2 GeV ionization energy as it passes through the calorimeter. Therefore we examine the calorimeter cells along the track path to seek a confirmation from the cell energies. If there is no sign of a charged particle penetrating the calorimeter on the reconstructed track, most likely the track is a background and is rejected. Finally, we reject muon candidates that exit at a certain angle ($|\eta| \approx 0.9$), because their path in the toroid is too short to have enough deflection for a good momentum measurement.

Like electrons, the muon from the W decay is usually isolated from jets (in contrast to the muon from b-quark or c-quark decay). To identify the muons from the W, we require the separation between the muon and the nearest jet in the η-ϕ plane must be greater than 0.5, or $\triangle R(\mu, jet) > 0.5$. Any muon which meets this requirement is referred to as an "isolated" muon. For the $t\bar{t} \rightarrow \mu +$ jets events, where there is one muon from the W decay, we require that one isolated muon is present (see Section 4.1).

3.1.4 Jets

Our jet finding algorithm is based on the calorimeter transverse energy in a cone of radius $R = \sqrt{\triangle\eta^2 + \triangle\phi^2}$, similar to that used by the UA1 and CDF collaborations [55, 56]. Our jet cone radius is chosen to be $R = 0.5$. The reconstruction steps are specified below.

1. For each $\triangle\eta \times \triangle\phi = 0.1 \times 0.1$ calorimeter tower, the transverse energy E_T is calculated as:

$$\begin{aligned} E_T &= \sqrt{{E_x}^2 + {E_y}^2} \qquad \text{where} \\ E_x &= \sum_i^{cells} E_x^i = \sum_i^{cells} E_i \sin\theta_i \cos\phi_i \\ E_y &= \sum_i^{cells} E_y^i = \sum_i^{cells} E_i \sin\theta_i \sin\phi_i \quad . \end{aligned}$$

2. Beginning with the highest E_T tower, "preclusters" are formed from contiguous

$E_T > 1$ GeV towers within $\Delta\eta \times \Delta\phi = 0.3 \times 0.3$. The precluster center is used as the initial centroid.

3. A new E_T weighted η-ϕ centroid is computed using E_T of all towers within a radius $R < 0.5$. The process is repeated until the centroid is stable (i. e. the change of the centroid location is less than 10^{-3} in η-ϕ space). The final centroid is the jet axis and the E_T contained in the final $R = 0.5$ cluster is the jet E_T.

4. If two jets are close to each other and share energy, then the shared amount of E_T is examined. If the shared E_T is more than 50% of that of the lower E_T cluster, the two clusters are merged, and the jet axis is recomputed. Otherwise, the clusters are split into two jets, and shared cells are reassigned to the closest jet.

5. A minimum threshold of 8 GeV is applied to jet candidates.

Since calorimeter cells in both the EM and hadronic sections are all used in the jet reconstruction, electrons and photons will be recognized as jet candidates. Therefore in our analysis identified electrons or photons have to be removed from jets.

3.1.5 Missing Transverse Energy ($\not\!\!E_T$)

In a parton-parton collision, the momenta of the interacting partons are parallel to that of their composite hadrons. The transverse momenta are negligible compared to the magnitude of their longitudinal momenta. Therefore, the total transverse momentum of the objects produced in the collision must be close to zero, or balanced, because the momentum must be conserved in the interaction.

When a large transverse momentum imbalance is observed, it suggests the presence of a high p_T neutrino (or neutrinos) because neutrinos do not interact with the detector. The transverse momentum imbalance, denoted as $\not\!\!E_T$, is measured using the calorimeter and the muon spectrometer. The component of $\not\!\!E_T$ from the calorimeter alone is denoted as $\not\!\!E_T^{cal}$. It is measured by summing over the energies in every calorimeter cell:

$$\begin{aligned}
\not{E}_x^{cal} &= -\sum_i^{all\,cells} E_i \sin\theta_i \cos\phi_i \\
\not{E}_y^{cal} &= -\sum_i^{all\,cells} E_i \sin\theta_i \sin\phi_i \\
\not{E}_T^{cal} &= \sqrt{{\not{E}_x^{cal}}^2 + {\not{E}_y^{cal}}^2}
\end{aligned}$$

where E_i is the energy in the particular cell, and θ_i and ϕ_i are the polar and azimuthal angles corresponding to each cell respectively. In addition to calorimeter energies, the momenta of muons must be considered. The $\not{E}_T$ is thus defined as

$$\begin{aligned}
\not{E}_x &= \not{E}_x^{cal} - \sum_i p_x^{\mu_i} \\
\not{E}_y &= \not{E}_y^{cal} - \sum_i p_y^{\mu_i} \\
\not{E}_T &= \sqrt{{\not{E}_x}^2 + {\not{E}_y}^2}\,.
\end{aligned}$$

This $\not{E}_T$ is a measurement of the neutrino transverse momentum.

3.2 Standard Energy Corrections

At DØ, there is a set of standard energy corrections, called CAFIX, regarding measurements within the calorimeter—measurements on electrons, photons, jets and $\not{E}_T$. Applied after the event reconstruction process, CAFIX is designed to correct existing calorimeter systematic biases including nonuniformity, nonlinearity in its response to hadrons, uranium radioactive noise, and extra energy due to spectator partons (underlying event).

In CAFIX, the energy scale of the EM section is calibrated [57] by setting the measured invariant mass peak of $Z \to e^+e^-$ to the measured LEP value. Lower mass resonances ($\pi^0 \to \gamma\gamma$, $J/\Psi \to ee$) have also been used to check the calibrated scale at lower energies.

The jet energies are corrected [58] for various detector effects using

$$E_{corr} = \frac{E_{meas} - O}{R(1-S)}\,,$$

where O is the offset energy due to both uranium noise and the underlying event; R is the calorimeter response to jets; and S is the fraction of the jet energy leaking out of the jet cone due to particle showering.

The O parameter is determined from the E_T density in minimum bias events, where only uranium noise and the spectator partons contribute to energies in the calorimeter. The hadronic scale is studied using $\gamma+$jets samples—since the EM scale is already calibrated, one can use the measured photon E_T to determine the jet response. A method using the $\not\!\!E_T$ projection has been proposed by CDF collaboration [56] and is adopted here to measure the jet response. Since the $\not\!\!E_T$ in the $\gamma+$jets event is largely due to the mismeasurement of jet energy, the method proposes the hadronic response be determined from the $\not\!\!E_T$ bias as

$$R = 1 + \frac{\vec{\not\!\!E}_T \cdot \hat{n}_T^\gamma}{E_T^\gamma},$$

where $\hat{n}_T^\gamma$ is the unit vector along the photon E_T, which is denoted as E_T^γ. The fraction of showering leakage S is determined by using Monte Carlo generated jets and the calorimeter showering simulation based on the test beam data. The transverse momentum of the final state particles within the fixed size cone is compared with the reconstructed jet E_T, and the out-of-cone leakage fraction is computed.

After the corrections have been carried out for electrons, photons and jets, the $\not\!\!E_T$, measured by all the energies deposited in the calorimeter, is recalculated according to the corrections on electromagnetic and hadronic clusters.

Although CAFIX is widely used for physics analyses at DØ, it is not sufficient for a precision top quark mass measurement. Since the energy leakage due to the gluon radiation and fragmented particles falling out of the cone is not considered in CAFIX, additional remedies will have to be introduced. These corrections are discussed in detail in Chapter 5.

3.3 Event Simulation

Accurate signal and background event simulations are critical for the measurement of the $t\bar{t}$ production cross section in order to optimize the selection cut, to estimate the detection acceptance and efficiency, and to calculate the number of background events in the final sample. The event simulation becomes even more demanding for the top mass measurement, because the observed data must be compared directly with the simulated signal and background in order to extract the top mass. The complexity of the top mass analysis, which involves not only the kinematic behavior of events but also the performance of every detector component, further underlines the importance of accurate simulation.

3.3.1 Signal Simulation

The DØ Monte Carlo simulation for $p\bar{p} \to t\bar{t} + X \to l + jets + X$ is primarily based on the HERWIG [59] generator, although an alternative generator, ISAJET [60], is also used to provide a comparison. In general, the generators start from the leading order parton-parton scattering and higher order QCD radiative corrections for initial and final state partons are later incorporated. Although the basic underlying assumptions are similar, the two event generators differ in the details of their implementation, including the employment of different phenomenological models for jet fragmentation. Monte Carlo samples of $t\bar{t}$ events have been generated with various input top mass values ranging from 110 GeV/c^2 to 230 GeV/c^2.

The detector responses to the generated final state particles are simulated with DØGEANT program [61]. This program incorporates the detector geometry and the materials of individual components and simulates the detector responses to charged particle tracks and electromagnetic & hadronic showering. After DØGEANT, the events are passed through a trigger simulator before they are reconstructed by the same reconstruction program that processes data.

3.3.2 W + jets Background Simulation

The VECBOS Monte Carlo program [62] is used to simulate the background from W + jets production. VECBOS is a parton-level program using exact tree-level matrix elements for W(or Z) + n jets processes, for which calculations are carried out with perturbative QCD at the order α_s^n. After final state partons are generated, HERWIG is used for fragmentation. The subsequent detector, trigger simulation and event reconstruction are the same as those of signal Monte Carlo.

3.3.3 QCD-multijet Background Simulation

We refer to any observed electron or muon not from the W-decay as a fake lepton. Most fake electrons arise from misidentified jets. Another source of fake leptons is heavy quark decays—either an electron or a muon can be produced in a b-quark or c-quark decay and, in some rare cases, passes the identification cut. Most QCD-multijet events have low $\not\!\!E_T$ because there is no high p_T neutrino present, but one could observe a high $\not\!\!E_T$ in those events due to a fluctuation in the energy measurement. In that case, if a fake lepton also occurs, the event is likely to pass the selection criteria and becomes a background event in the candidate sample.

To simulate the QCD background, we use multijet data events in which the high p_T electron or muon candidate is almost certain to be a fake one: $\mathcal{L}_e > 1.5$ for CC fake electrons, $\mathcal{L}_e > 2.0$ for EC fake electrons, and $\triangle R(\mu, jet) < 0.5$ for fake muons. The rest of the selection criteria is the same as that for the data (described in Chapter 4) in order to precisely model the kinematic behaviors of the QCD background.

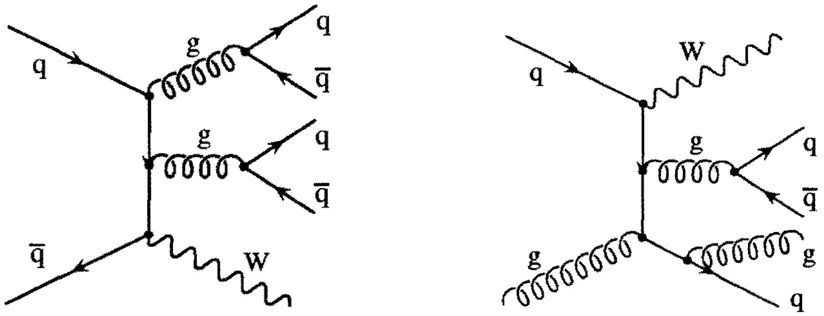

Figure 3.3: Examples of the W +jets background processes.

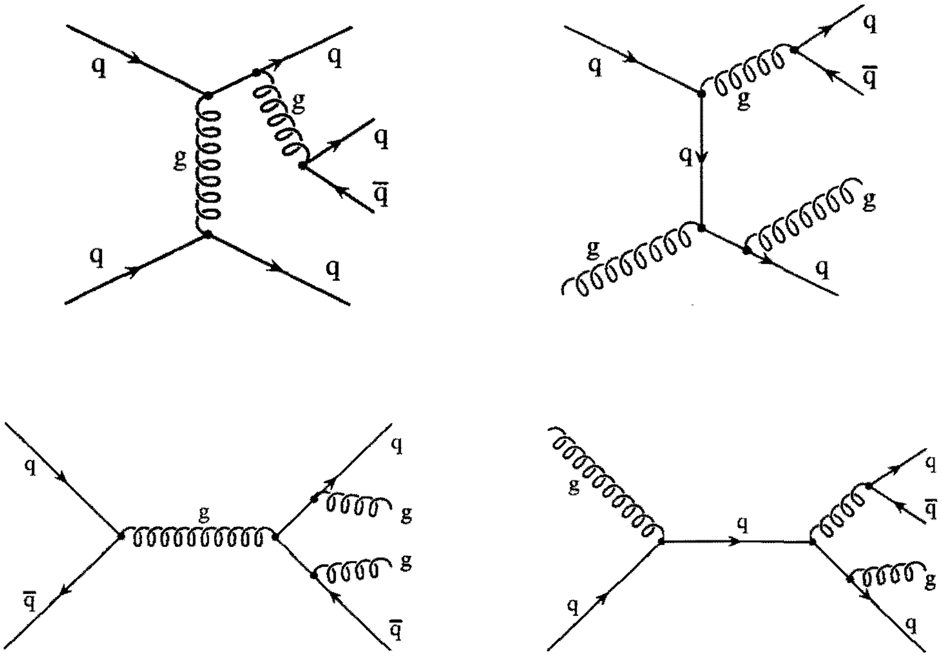

Figure 3.4: Examples of the QCD-multijet processes.

Chapter 4

Event Selection

Our analysis consists mainly of three parts: event selection, which optimizes the signal-to-background ratio for further analysis; jet corrections, which minimize jet energy biases in the reconstruction process for the top mass; and lastly the top mass analysis which comprises algorithms to measure the top mass from our data. We will discuss event selection in this chapter, jet corrections in Chapter 5 and the top mass extraction algorithms in Chapters 6 and 7.

As we pointed out in Chapter 1, we will use $t\bar{t} \to l$+jets channels to extract the top quark mass. The background of l+jets events mainly comes from $W +$jets production and QCD-multijet events in which a lepton is misidentified. What must be done in our event selection is to suppress these two sources of background, according to some distinct features that background and signal events possess. In the end, we want to have a final sample where not only the signal events comprise a larger fraction, but also the total number of events is statistically large enough for the extraction of the top quark mass.

Our selection procedures for $t\bar{t} \to l +$jets events consist of two stages. The first stage is to apply a basic and loose cut in order to collect a base sample in which events have the characteristics of the l+jets events, namely, a high p_T charged lepton, a large $\not{E}_T$, and several jets. The second stage employs a more sophisticated cut that aims at enhancing the signal-to-background ratio while at the same time not introducing systematic biases on the reconstructed top mass. Details are described

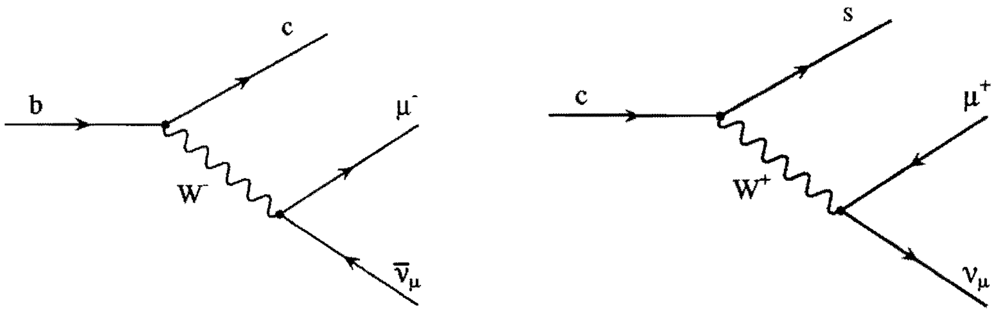

Figure 4.1: The processes of b and c quark decays that can be tagged by a soft muon.

in the following two sections.

4.1 Basic Selection Criteria

At DØ, we use low p_T (soft) muons to tag b-quark or c-quark jets that include muons as depicted in Figure 4.1. The branching ratio of $b \to \mu X$ is about 20%, including cascade decays $b \to c \to \mu X$; while the branching ratio of $c \to \mu X$ is about 10%. Since each $t\bar{t} \to l + \text{jets}$ event contains two b-quark jets and a c-quark jet half of the time, approximately 40% of $t\bar{t} \to l + \text{jets}$ events have a muon associated with jets.

The tagging algorithm is to find a muon adjacent to a jet. In addition to the muon identification criteria, we require that the tag muon must satisfy the following conditions:

1. the muon p_T must be greater than $4\,\text{GeV}/c$
2. the separation between the muon and its nearest jet in η-ϕ space must be less than 0.5 ($\triangle R(\mu, jet) < 0.5$).

Signal events are much more likely to have a tag muon than their backgrounds: approximately 20% of $t\bar{t}$ events have an observed tag muon, compared to only about 2% in the W + jets and QCD backgrounds.

The tag muons should be clearly distinguished from the muons from the W decay. In the latter case, the muon has a high transverse momentum and is usually isolated

e+jets cut	μ+jets cut
1 electron ($E_T > 20\,\text{GeV}$, $\lvert\eta\rvert < 2.0$)	1 isolated muon ($p_T > 20\,\text{GeV}/c$, $\lvert\eta\rvert < 1.7$)
≥ 4 jets ($E_T > 15\,\text{GeV}$, $\lvert\eta\rvert < 2.0$)	≥ 4 jets ($E_T > 15\,\text{GeV}$, $\lvert\eta\rvert < 2.0$)
$\not{E}_T^{cal} > 25\,\text{GeV}$, $\not{E}_T > 20\,\text{GeV}$	$\not{E}_T^{cal} > 20\,\text{GeV}$, $\not{E}_T > 20\,\text{GeV}$

Table 4.1: Basic selection requirements for e+jets and μ+jets events.

from jets. Therefore, for μ+jets events, there must be exactly one isolated muon (defined in Subsection 3.1.3) regardless of any tag muon presence.

Since the main ring passes through the DØ calorimeter, its noise in the form of localized calorimeter energies arises during its beam injection periods. This contamination happens in about one fifth of our data and is constantly monitored in the data taking and event reconstruction processes. Algorithms have been developed to reject heavily contaminated events and to remove the noise for slightly contaminated events.

The basic requirements for e+jets and μ+jets are specified in Table 4.1. Basically, they are intended to select events which contain the primary characteristics of the l+jets event—exactly one isolated electron or muon, a signature of a high p_T neutrino (large $\not{E}_T$), and four or more jets. In addition, we reject events with any identified photons because they are inconsistent with the $t\bar{t}$ assumption.

Depending on whether tag muons are present, events undergo two different paths for further examination. If an event has a tag muon, denoted as e+jets/μ or μ+jets/μ for e+jets, μ+jets channels respectively, both $\not{E}_T^{cal}$ and $\not{E}_T$ are likely to be affected by the accuracy of the muon momentum measurement. To ensure that the large $\not{E}_T^{cal}$ and $\not{E}_T$ are not caused by mismeasured muon momentum, we apply additional cuts on the $\not{E}_T^{cal}$ and $\not{E}_T$ vectors as listed in Table 4.2.

If there is no tag muon, we impose another cut to suppress the QCD background. Two variables are used for this purpose:

1. The "computed" pseudorapidity of the W which decayed leptonically, denoted as η^W. Assuming the measured $\not{E}_T$ is equal to the neutrino p_T, together with

e+jets/μ	μ+jets/μ
$\not{E}_T^{cal} > 35\,\mathrm{GeV}$ if $\triangle\phi(\not{E}_T^{cal}, \mu) < 25°$	For highest p_T muon: $\frac{\lvert\triangle\phi(\not{E}_T, \mu) - 90°\rvert}{90°} < \frac{\not{E}_T}{45\,\mathrm{GeV}}$ and $\triangle\phi(\not{E}_T, \mu) < 170°$

Table 4.2: Additional requirement for the mu-tagged events. $\triangle\phi(\not{E}_T^{cal}, \mu)$ is the azimuthal angle between $\not{E}_T^{cal}$ and μ, similarly for $\triangle\phi(\not{E}_T, \mu)$.

the measured momentum of e or μ, one can solve for p_z of the W (p_z^W) by the invariant W mass constraint. Usually two real roots for p_z^W are found from the quadratic equation, and the one with the smaller absolute value is used (this choice is based on our Monte Carlo study). If there is no real solution, the $\not{E}_T$ is scaled so that the transverse mass[1] of the charged lepton and the neutrino is equal to the W mass, and one real solution for p_z^W is found. Once the momentum of the W is determined, η^W can be computed.

2. The scalar sum of $\not{E}_T$ and the charged lepton p_T, denoted as E_T^W ($= p_T^l + \not{E}_T$).

Figure 4.2 shows distributions of η^W and E_T^W for signal (HERWIG generated) and QCD background. We require an untagged event to satisfy:

$$\begin{aligned} |\eta^W| &< 2 \\ E_T^W &> 60\,\mathrm{GeV}\,. \end{aligned}$$

The estimation of background is based primarily on the fact [62] that the ratio of number of events when the jet multiplicity increases by one should be roughly constant, or

$$\frac{N_{n-1}}{N_n} \approx \frac{N_n}{N_{n+1}} \approx \text{constant}$$

where N_n stands for the number of events with $\geq n$ jets. This relation has been proven valid in our data for both W + jets and QCD backgrounds. As an example, Figure 4.3

---

[1] The transverse mass of two objects l and ν, denoted as $M_T(l, \nu)$, is defined as $M_T^2(l, \nu) \equiv \left(|\mathbf{p}_\mathbf{T}^\mathbf{l}| + |\mathbf{p}_\mathbf{T}^\nu|\right)^2 - \left(\mathbf{p}_\mathbf{T}^\mathbf{l} + \mathbf{p}_\mathbf{T}^\nu\right)^2$, where $\mathbf{p}_\mathbf{T}^\mathbf{l}$ and $\mathbf{p}_\mathbf{T}^\nu$ are momentum vectors of l and ν respectively.

shows the jet multiplicity distribution of W+jets in the e+jets channel. Detailed studies on the background estimation are documented elsewhere [63]. The background estimates in various channels after the basic selection are listed in Table 4.3.

	e+jets	μ+jets	e+jets/μ	μ+jets/μ	All l+jets
Luminosity (pb^{-1})	105.9	95.7	90.5	95.7	
W+jets bkg	33.9 ± 3.9	28.2 ± 8.5	0.99 ± 1.09	0.84 ± 0.19	63.9 ± 9.4
QCD bkg	8.5 ± 2.7	9.4 ± 3.4	0.25 ± 0.79	1.08 ± 0.30	19.2 ± 4.4
Total bkg	42.4 ± 4.7	37.5 ± 9.1	1.24 ± 1.35	1.91 ± 0.35	83.1 ± 10.4
Observed events	43	40	4	2	89

Table 4.3: Estimated background numbers after the basic selection.

4.2 Signal-Background Discriminant

To this point, the expected background in our sample of 89 events is very large. Clearly more effort is needed to reduce the background, especially in the untagged channels. Fortunately, there are kinematic properties that distinguish $t\bar{t}$ and background events which make further background reduction possible. Using four kinematic variables, a more sophisticated background reduction algorithm was developed by M. Strovink and S. Protopopescu [64]. The four kinematic variables are:

- $x_1 = \not{E}_T$ (without scaling).
- x_2 = Aplanarity [65] of the jets and the W. ($3/2\times$ the least eigenvalue of normalized laboratory momentum tensor of the jets and the W.)
- $x_3 = \dfrac{H_T - E_T^{j_1}}{H_{\|}}$, where

  H_T is the sum of $|E_T|$ of the jets,
  $E_T^{j_1}$ is the leading jet E_T, and
  $H_{\|}$ is the sum of $|p_z|$ of the jets, the charged lepton, and the neutrino.

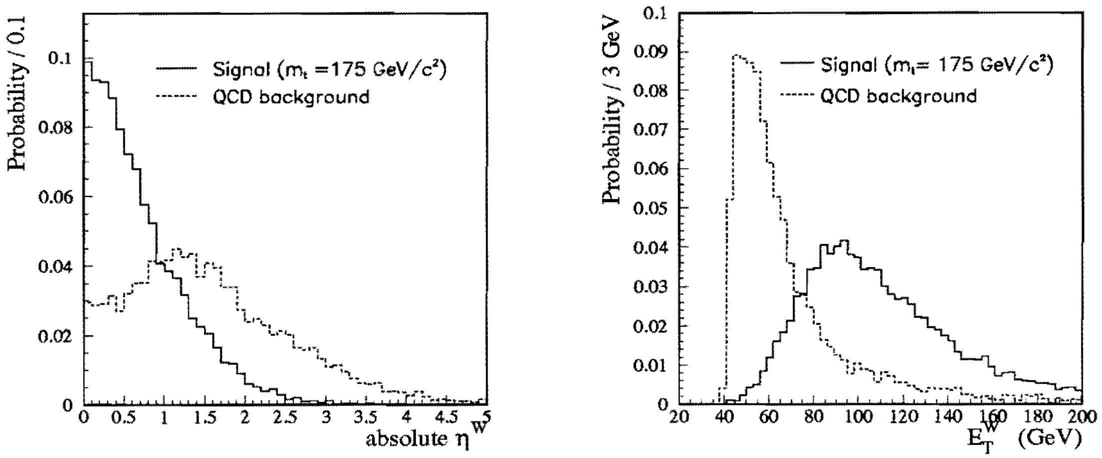

Figure 4.2: Distributions of $|\eta^W|$ (Left) and E_T^W (right). Signal distributions are modeled by HERWIG with $m_t = 175\,\mathrm{GeV}/c^2$. The QCD sample comes from data.

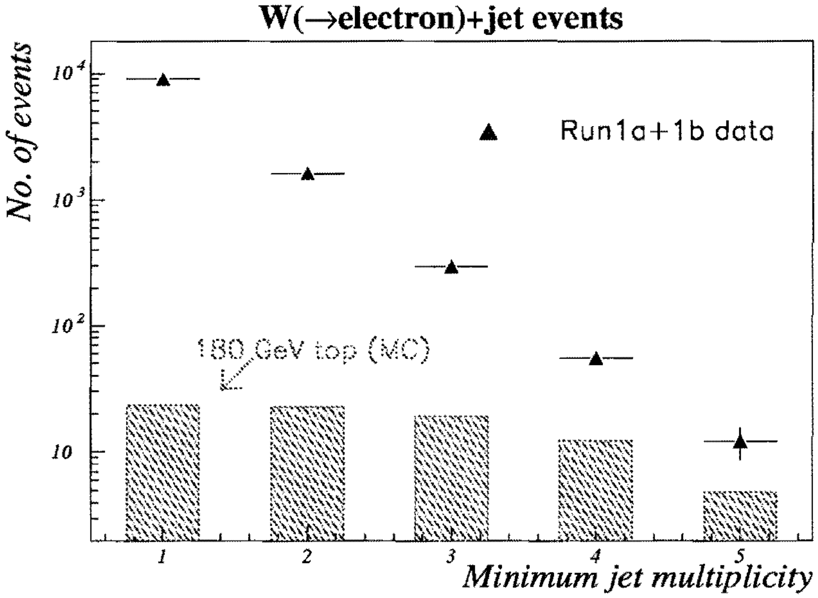

Figure 4.3: Number of events as a function of jet multiplicity for inclusive e+jets data and HERWIG generated $t\bar{t}$ Monte Carlo.

- $x_4 = \dfrac{\triangle R_{jj}^{\min} E_T^{j<}}{E_T^W}$, where

  $\triangle R_{jj}^{\min}$ is the minimum distance in the η-ϕ space between two jets, and
  $E_T^{j<}$ is the smaller jet E_T for the two jets in $\triangle R_{jj}^{\min}$.

Distributions of these variables for signal, W + jets and QCD backgrounds are compared, and a signal-background discriminant is concocted out of the observed variables. Procedures to compute the discriminant are specified below.

1. Parameterize $\mathcal{L}_i(x_i) \equiv \dfrac{s_i(x_i)}{b_i(x_i)}, \quad i = 1, \cdots 4$, where

   $s_i(x_i)$ is the signal probability density function of variable x_i, and
   $b_i(x_i)$ is the background probability density function of x_i.

2. Form a likelihood $\mathcal{L}$ that $\ln \mathcal{L} \equiv \sum_{i=1}^{4} w_i \ln \mathcal{L}_i$, where

   the weights w_i are adjusted away from unity[2] to nullify correlations with the fitted top mass.

3. The discriminant is defined as $\mathcal{D} \equiv \dfrac{\mathcal{L}}{1 + \mathcal{L}}$.

The computed discriminant $\mathcal{D}$, ranging between 0 and 1, is powerful for background rejection. As shown in Figure 4.4, both W + jets and QCD backgrounds tend to have $\mathcal{D}$ closer to zero, whereas signal events are more likely to have $\mathcal{D}$ closer to unity.

In addition to the discriminant $\mathcal{D}$, another kinematic variable H_{T2} is also useful for suppressing the background in the untagged channels. H_{T2} is defined as the scalar sum of all but the leading jet E_T:

$$H_{T2} \equiv \sum_{i=2}^{N_{jets}} E_T^i \ .$$

---

[2] The weights used are $w_1 = 1.016$, $w_2 = 0.715$, $w_3 = 0.759$, $w_4 = 0.812$.

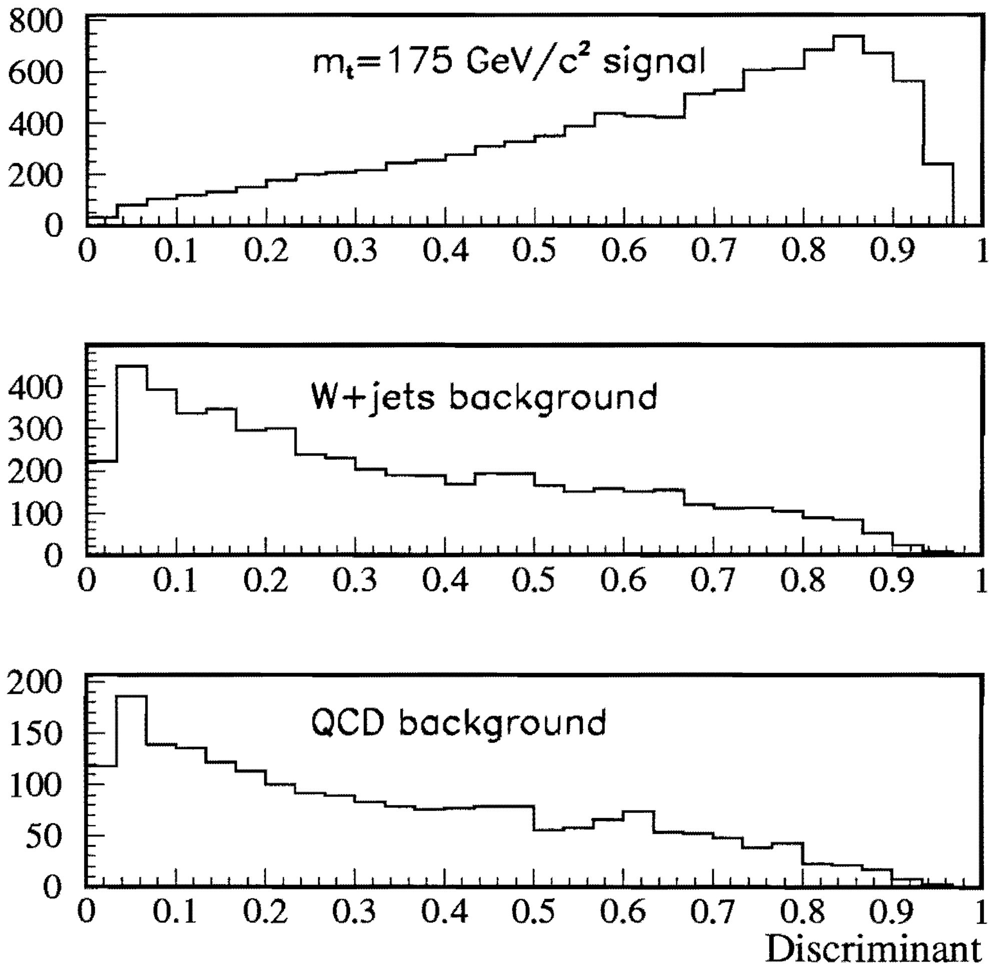

Figure 4.4: Distribution of the $t\bar{t}$ discriminant for signal (HERWIG Monte Carlo), W+jets background (VECBOS Monte Carlo) and QCD background (data).

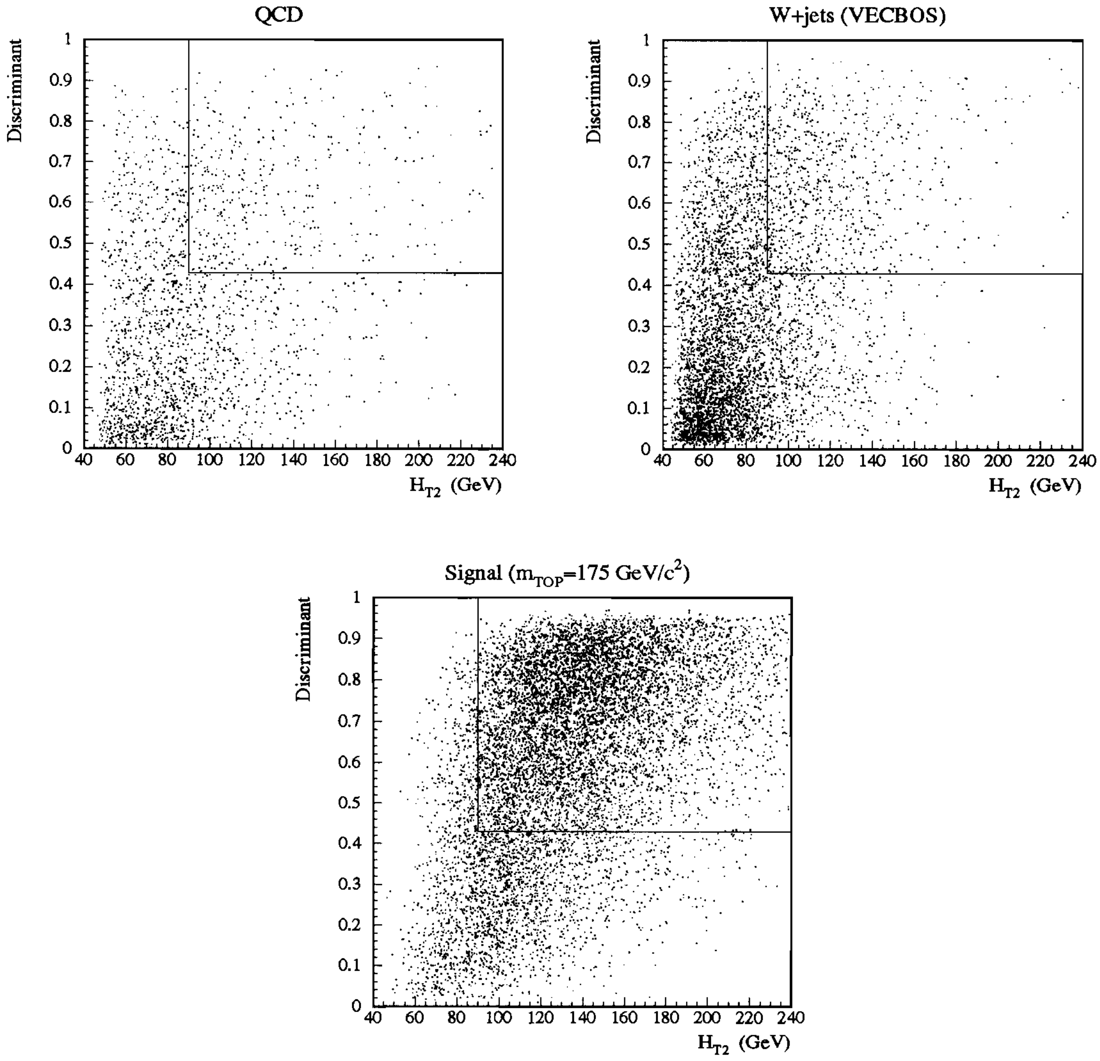
QCD

W+jets (VECBOS)

Signal (m_{TOP}=175 GeV/c^2)

Figure 4.5: The $\mathcal{D}$ *vs.* H_{T2} scatter plots for QCD and W+jets backgrounds and $t\bar{t}$ signal (HERWIG, $m_t = 175\,\mathrm{GeV}/c^2$). The selection cut $\mathcal{D} > 0.43$ & $H_{T2} > 90\,\mathrm{GeV}$ is superimposed in each plot.

	e+jets		μ+jets	
	efficiency	pass/total	efficiency	pass/total
W+jets bkg	$(15.11 \pm 0.71)\%$	383/2534	$(15.44 \pm 0.67)\%$	448/2901
QCD bkg	$(14.67 \pm 1.01)\%$	181/1234	$(25.50 \pm 1.45)\%$	229/898
$t\bar{t}$ signal	$(72.11 \pm 0.66)\%$	3363/4664	$(73.09 \pm 0.61)\%$	3920/5363

Table 4.4: The efficiency of the cut, $\mathcal{D} > 0.43$ and $H_{T2} > 90\,\text{GeV}$, for signal (HERWIG, $m_t = 175\,\text{GeV}/c^2$) and backgrounds. This cut is applied only to untagged events. The efficiencies and errors are calculated using Binomial statistics from the number of events passing the cut and the number of total events, which are shown in the pass/total column.

We require $\mathcal{D} > 0.43$ and $H_{T2} > 90\,\text{GeV}$ if the event has no tag muon. Table 4.4 summarizes the efficiencies of the cut for the signal and background, which are calculated based on HERWIG-generated $t\bar{t}$ samples, VECBOS-generated W+jets samples, and QCD background from data. The various backgrounds after the cut are calculated from Table 4.3 and listed in Table 4.5.

Only 35 events pass the cut. They will be further analyzed to extract the top mass. The total background in the final sample, as shown in Table 4.5, is estimated to be 16.3 ± 2.2. The probability[3] of an upward fluctuation of the background to 35 or more events is 1.7×10^{-4}, equivalent to a $3.8\,\sigma$ effect.

Two candidate events are displayed in Figure 4.6 in the form of lego plot, where the direction of each object is plotted in the η-ϕ plane and the magnitude of transverse momentum is drawn as the height.

---

[3] The probability is calculated using Poisson statistics, taking into account the Gaussian error of the estimated background.

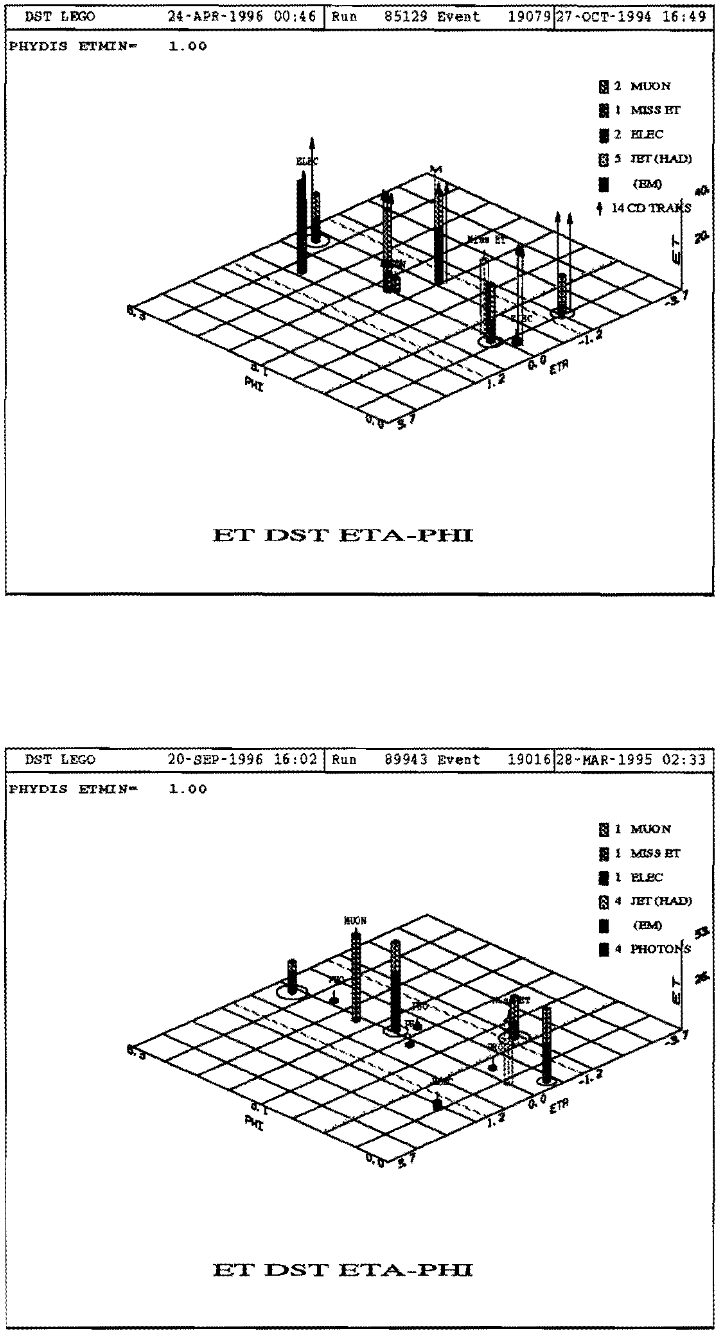

Figure 4.6: Display of $t\bar{t}$ candidate events: electron, muon, jets and $\not\!\!E_T$ are depicted in the η-ϕ plane with their height representing the transverse momentum. The event on the top is an e+jets/μ candidate. On the bottom, it shows a μ+jets candidate event.

	e+jets	μ+jets	e+jets/μ	μ+jets/μ	All l+jets
W+jets bkg	5.13 ± 0.59	4.35 ± 1.30	0.99 ± 1.09	0.84 ± 0.19	11.30 ± 1.81
QCD bkg	1.24 ± 0.39	2.43 ± 0.89	0.25 ± 0.79	1.08 ± 0.30	5.00 ± 1.29
Total bkg	6.37 ± 0.71	6.78 ± 1.58	1.24 ± 1.35	1.91 ± 0.35	16.31 ± 2.22
Observed events	13	16	4	2	35

Table 4.5: The estimated backgrounds and observed events after the discriminant cut.

Chapter 5

Jet Corrections and Jet Energy Scale

At this point, we have a candidate sample and the estimated number of background events in the sample. But before we can continue to analyze the sample, we have to deal with the jet measurements which are crucial for an accurate measurement of the top quark mass, because in a l+jets event, four out of six objects from t and $\bar{t}$ decays are jets. As mentioned in Chapter 3, the jet energy loss due to gluon radiation and fragmented particles falling out of the jet cone are not accounted for in CAFIX. Therefore, we need post-CAFIX jet corrections to compensate this energy loss.

To demonstrate the need for the jet correction, let us take $t\bar{t}$ Monte Carlo events and reconstruct the mass of W bosons which decay hadronically into two jets:

$$M_W^2 = (E_1 + E_2)^2 - |\vec{P}_1 + \vec{P}_2|^2 \,, \tag{5.1}$$

where E_i and $\vec{P}_i$ are the energy and momentum of the i-th jet respectively. The reconstructed M_W distribution is on the left hand side of Figure 5.1, in which the peak occurs at a position lower than the true M_W ($\approx 80\,\mathrm{GeV}/c^2$). The out-of-cone radiation is even more obvious if the parton energy (from Monte Carlo) is compared with the CAFIX corrected jet energy as shown on the right hand side of Figure 5.1.

Since the top quark decays immediately without hadronizing, its mass can be reconstructed from the parton-level energy (the energy before fragmentation for quarks) of the decay products. Any energy loss due to either the gluon radiation or fragmentation out of the jet cone will systematically shift the reconstructed top mass peak.

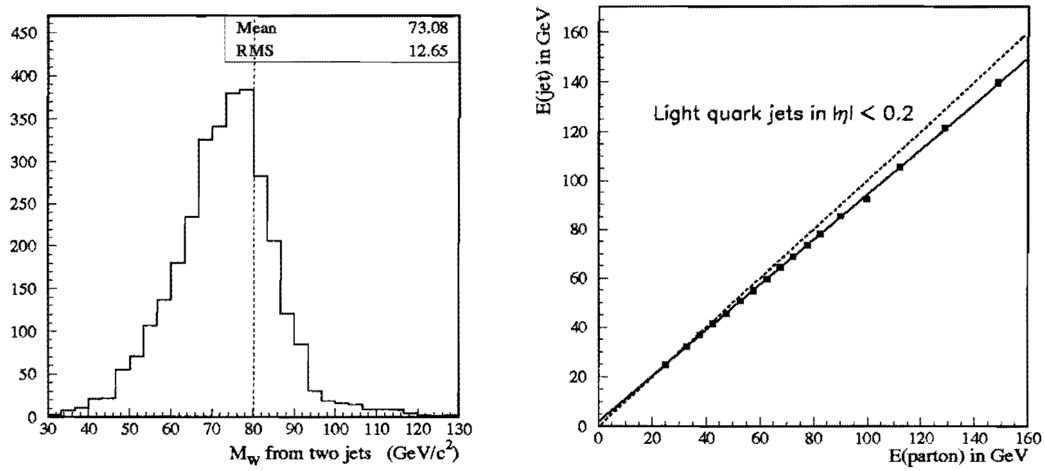

Figure 5.1: **Left**: W mass reconstructed from the two jets the W decays into, where the jets are previously corrected by CAFIX. The peak occurs at a position lower than the true $M_W \approx 80\,\mathrm{GeV}/c^2$. **Right**: Parton energy (x) *vs.* CAFIX corrected jet energy (y). The out-of-cone energy loss is clearly seen in comparison with the ideal $x = y$ dashed line. Although the jets in this plot are limited to be central ($|\eta| < 0.2$), the effect exists to various degrees in all η regions.

Therefore, we have to compensate the out-of-cone energy loss in order to correct the measured jet energy back to the parton level. This is the basic motivation for the corrections to be discussed in the following section.

In addition to the out-of-cone effect, there is another source of energy loss for b and c quark jets: the energy of the neutrino in b or c quark's semi-leptonic decay is not measured. We separate b-quark jets from light quark (including c quarks) jets in correcting their energy to the parton level, because hypothesis about the identity of b-quark jets will be made in the later kinematic fit, thus allowing us to treat the assigned b-quark jets differently from the other jets.

The latter half of this chapter is devoted to the jet energy scale study, which was initially aimed at determining the energy scale uncertainty, but ended up by introducing a correction to fix the problem with the energy scale. In the end, we will use a Z + jets sample to cross check the result of a series of corrections for jets.

5.1 Jet Corrections

The parton information needed for the corrections is provided by HERWIG (v5.7) generated $t\bar{t}$ Monte Carlo samples with the input top mass ranging from 160 to 210 GeV/c^2. Different correction algorithms [66] are used for tagged and untagged jets, because the tag muon provides additional information for the tagged jet.

An untagged jet could be fragmented from a gluon, a light quark, or a b-quark. But attention must be paid to the fact that an untagged jet can originate from a b-quark which decays into $\mu + X$, with the μ failing to be detected. In the kinematic fit which we will describe in the next chapter, each jet will be assumed to be either a light quark jet or a b-quark jet, so here we want to correct light quark and b-quark untagged jets separately for the purpose of later analysis.

For a tagged jet, it is most likely to be a b-quark jet, though it can also be a c-quark jet. However, we will derive the correction for the tagged jets from a collection of tagged jets which are truly fragmented form the b-quark. The reason for this is that we will assume every tagged jet is a b-quark jet in the later kinematic fit.

5.1.1 Correction for Untagged Jets

When the quark energy at the parton level is compared with the measured jet energy (CAFIX corrected), we see a linear relation between them very consistently—at different η regions for the light quark jets and for the untagged b-quark jets as well—as shown in Figure 5.1 (right). Each data point represents both the mean of the parton energy on the x-axis and the mean of the jet energy on the y-axis in a parton energy bin whose size is adjusted to ensure enough statistics within the bin. Biases would occur if the binning were made with the jet energy, because the jet energy is a smeared observable—the result would be affected by the initial parton energy distribution and the jet energy resolution.

To correct the measured energy to the parton level, we fit the data points with a straight line. Once we have the fitted parameters, the correction is straightforward:

$$E_{cor} = \frac{E_{jet} - I}{M}, \tag{5.2}$$

	Light quark jets		Untagged b-jets	
η region	I	M	I	M
$\|\eta\| < 0.2$	0.3222	0.9331	-0.6722	0.9065
$0.2 < \|\eta\| < 0.6$	0.6350	0.9299	-1.3365	0.9137
$0.6 < \|\eta\| < 0.9$	1.8620	0.8831	0.0016	0.8675
$0.9 < \|\eta\| < 1.3$	1.6962	0.9331	-0.5476	0.9035
$1.3 < \|\eta\|$	4.4978	0.8818	2.4648	0.8588

Table 5.1: The offset and slope parameters in *parton energy vs. jet energy* used in the jet correction for light quark and untagged b-quark jets in various η regions.

where E_{cor} is the corrected jet energy, E_{jet} is the measured jet energy, I is the intercept on y, and M is the slope. Since the out-of-cone radiation varies to some extent in different η regions, the corrections are derived for five η bins, as shown in Table 5.1, with enough statistics in each bin to determine the parameters.

The derived corrections are then applied back to the jets and checked by comparing the corrected jet energy with the parton energy. The resolution of corrected jet energy can be parameterized as

$$\left(\frac{\sigma}{E}\right)^2 = \mathcal{C}^2 + \frac{\mathcal{S}^2}{E} \tag{5.3}$$

as shown in Figure 5.2 ,where the fitted parameters $\mathcal{C}$ and $\mathcal{S}$ are listed below.

	$\mathcal{C}$	$\mathcal{S}$
Light quark jets	0.064	1.04
Untagged b-jets	0.120	1.08

5.1.2 Correction for Tagged Jets

For tagged b-quark jets, two corrections need to be made to each jet. One correction is for the leptonic part of the energy (E_l), which includes the energies of the muon and neutrino in the b-quark's semi-leptonic decay. The other correction is for the hadronic part of energy (E_h), which is the energy associated with the parton fragmentation.

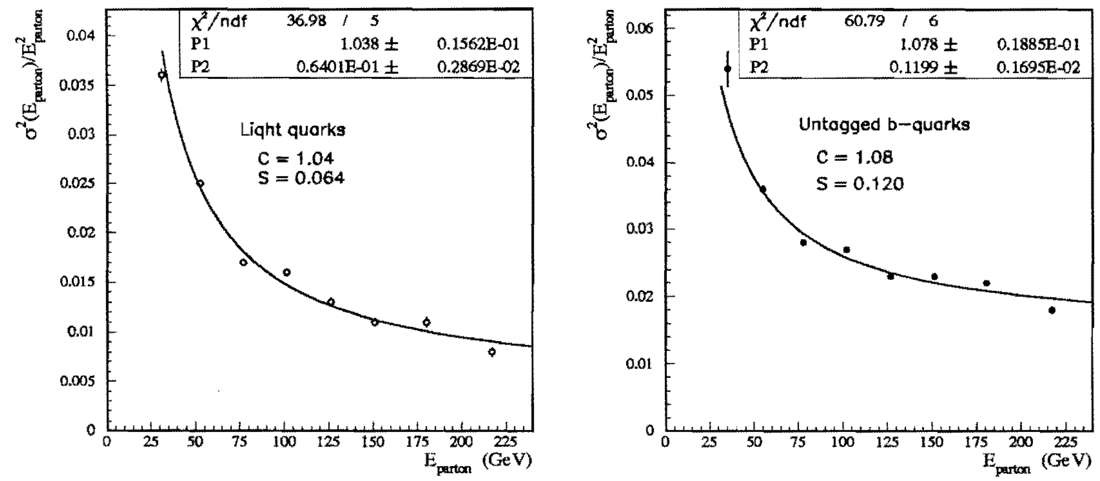

Figure 5.2: After corrections are applied, σ^2/E^2 is plotted against E for light quarks (**Left**) and untagged b-quarks (**Right**).

The correction for the leptonic energy E_l is intended to compensate the unmeasured neutrino energy in the semi-leptonic decay. Its procedure consists of the following two steps:

- Our understanding of muon momentum resolution [47] indicates that the measured momenta tend to be biased towards a high value. The relation between the true tag muon energy in a $t\bar{t}$ event and the measured energy is shown in Figure 5.3 (Left), where the tag muon spectrum is modeled by HERWIG-generated $t\bar{t}$ Monte Carlo. Using the fit function of Figure 5.3 (Left), we map the measured tag muon energy (E^m_μ) to its corrected value (E^c_μ).

- Let us denote the true energy of the tag muon as E_μ and that of the neutrino as E_ν; thus $E_l = E_\mu + E_\nu$. Although E_μ and E_ν are not strongly correlated in general, $\langle (E_\mu + E_\nu)/E_\mu \rangle$ can be fit as a function of E_μ as shown in Figure 5.3 (Right). Let us denote the function as $f(E_\mu)$. The corrected E_l is then $E^c_l = f(E^c_\mu)\, E^c_\mu$.

The resolution for E_l, denoted as $\sigma(E_l)$, is checked in Figure 5.4, where the resolution squared $\sigma^2(E_l) \equiv \langle (E^c_l - E_l)^2 \rangle$ is plotted as a function of $(E^m_\mu)^{-1}$.

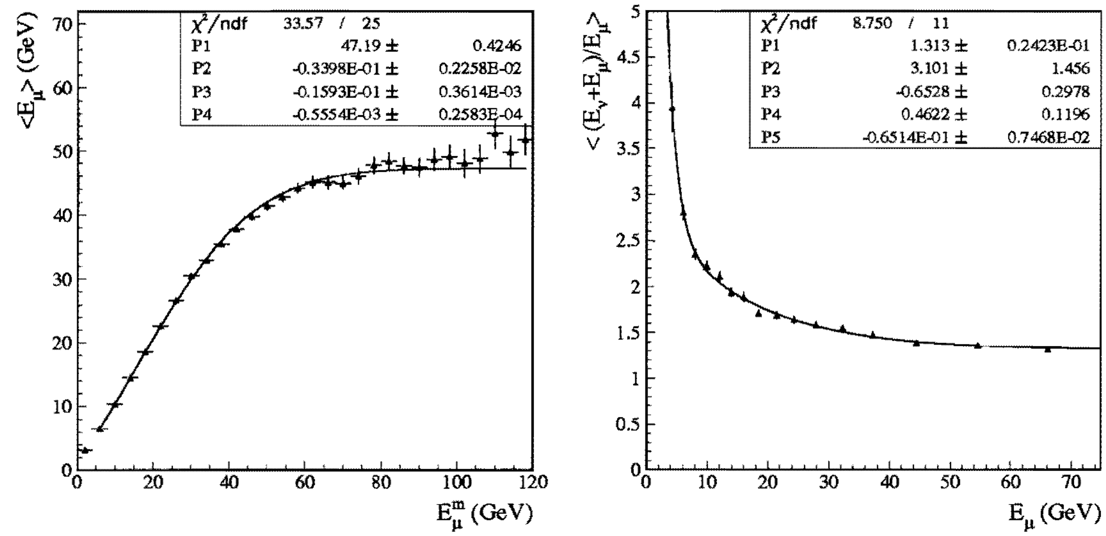

Figure 5.3: **Left**: The relation between the measured muon energy and the true muon energy. Fit function: $y = p_1(1 - e^{p_2+p_3x+p_4x^2})$. **Right**: $\langle(E_\mu + E_\nu)/E_\mu\rangle$ as a function of the muon energy E_μ. Fit function: $y = p_1 + e^{p_2+p_3x} + e^{p_4+p_5x}$.

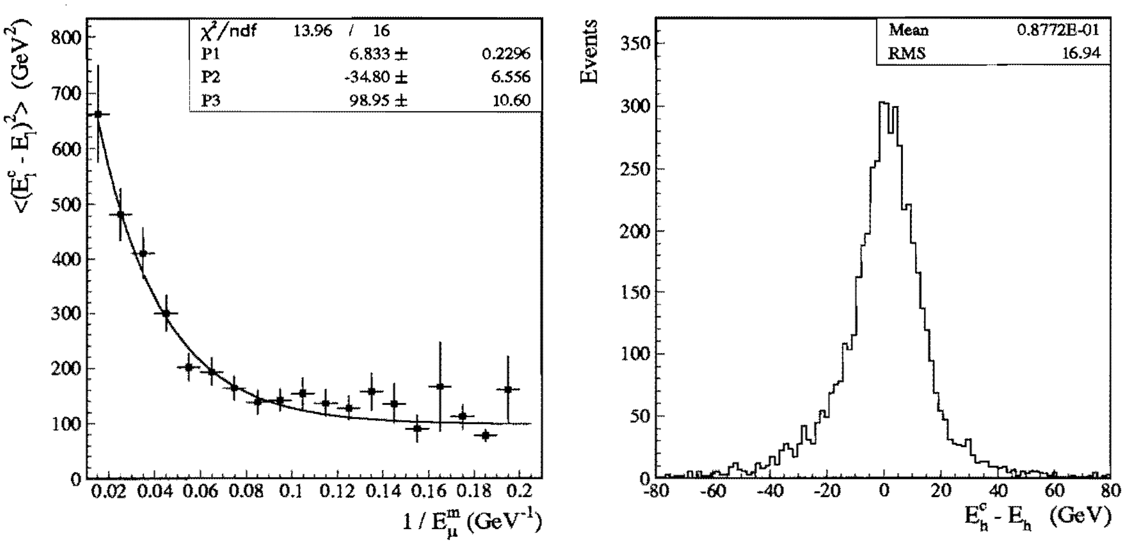

Figure 5.4: **Left**: $\sigma^2(E_l)$ (E_l resolution squared) as a function of the inverse of measured muon energy. Fit function: $y = e^{p_1+p_2x} + p_3$. **Right**: The distribution of $(E_h^c - E_h)$. The overall resolution of E_h is $\approx 17\,\text{GeV}$.

For the hadronic part of correction, we correct the tagged jet for its out-of-cone energy loss with the light-quark parameters in Table 5.1. The reason for not using the untagged b-jet parameters is that with an observed tag muon, the tagged jet is less likely to have another undetected soft-muon as in the case for the untagged b-jets.

A muon track typically deposits ~1-2 GeV of energy in ionization. This energy will be measured as part of the jet energy. But since it is already included in the corrected leptonic energy, we have to subtract it from the jet to avoid double measuring. The corrected hadronic energy is checked with the true hadronic energy, and its overall resolution is shown in Figure 5.4 (Right).

Finally, we take the sum of the resulting leptonic and hadronic energies ($E_l^c + E_h^c$) to be the corrected energy for the tagged b-quark.

5.1.3 Checking the Corrections

Since the identities of the partons initiating each jet are known in the $t\bar{t}$ Monte Carlo, we can check the corrections by reconstructing the W mass from the two jets in the W decay $W \to q\,q\prime$ as (5.1), and the top quark mass from three jets in the top decay $t \to b\,W \to b\,q\,q'$ as

$$m_t^2 = (E_1 + E_2 + E_3)^2 - |\vec{P}_1 + \vec{P}_2 + \vec{P}_3|^2 \,, \tag{5.4}$$

where E_i and $\vec{P}_i$ are the energy and momentum of the i-th jet respectively. We denote the former 2-jet mass as M_W^{2j} and the latter 3-jet mass as m_t^{3j}. Figures 5.5 to 5.7 show the distributions of M_W^{2j} and m_t^{3j} from HERWIG-generated $t\bar{t}$ events with the top mass 140, 180, and 220 GeV/c^2.

Comparing the results before and after the jet corrections, we have the following observations:

1. The light-quark jet correction moves the M_W^{2j} peak from a lower value to the true M_W. This shows the light-quark jet correction is correctly derived.
2. Improved results are obtained in m_t^{3j} when the b-quark jet is untagged indicates no serious flaw with the correction for untagged b-quark jets.

	before correction			after correction		
m_t	$\langle M_W^{2j} \rangle$	$\langle m_t^{3j} \rangle$(untag)	$\langle m_t^{3j} \rangle$(tag)	$\langle M_W^{2j} \rangle$	$\langle m_t^{3j} \rangle$(untag)	$\langle m_t^{3j} \rangle$(tag)
140	72.4	124.7	114.3	76.9	135.3	140.8
180	73.2	160.1	146.6	77.9	174.4	180.1
220	74.1	196.2	174.9	79.0	214.3	214.2

Table 5.2: The mean of M_W^{2j} and m_t^{3j} (in GeV/c^2) with both the b-quark jet tagged and untagged before and after the jet correction from $t\bar{t}$ Monte Carlo events with the top mass 140, 180, and 220 GeV/c^2.

3. A similar observation for m_t^{3j} when the b-quark jet is tagged suggests no serious flaw with the correction for tagged b-quark jets.

4. The corrections work well for the $t\bar{t}$ events with the top mass between 140 and 220 GeV/c^2.

The means of these distributions are listed in Table 5.2.

5.2 Jet Energy Scale

We have seen the jet corrections work successfully for Monte Carlo $t\bar{t}$ events; however, before they can be applied to the top mass analysis, we ought to cross-check them with data. Moreover, we need to understand the jet energy scale uncertainty after jets are corrected, which will be used in estimating the systematic error on the measured top mass.

The ideal sample for our energy scale study is γ+jets (direct photon) events [67] for two reasons. First, the well-calibrated EM sector enables the photon to provide an absolute energy scale for jets. Second, the abundant γ+jets events from data cover a wide range of jet E_T.

To study the jet energy scale in various η regions for different E_T ranges, we choose events with exactly one jet ($\gamma + 1$ jet events, depicted in Figure 5.8) and require that the photon and the jet are approximately back-to-back in ϕ. Using the well-measured photon E_T, we can gauge the jet energy scale at a particular η by balancing photon

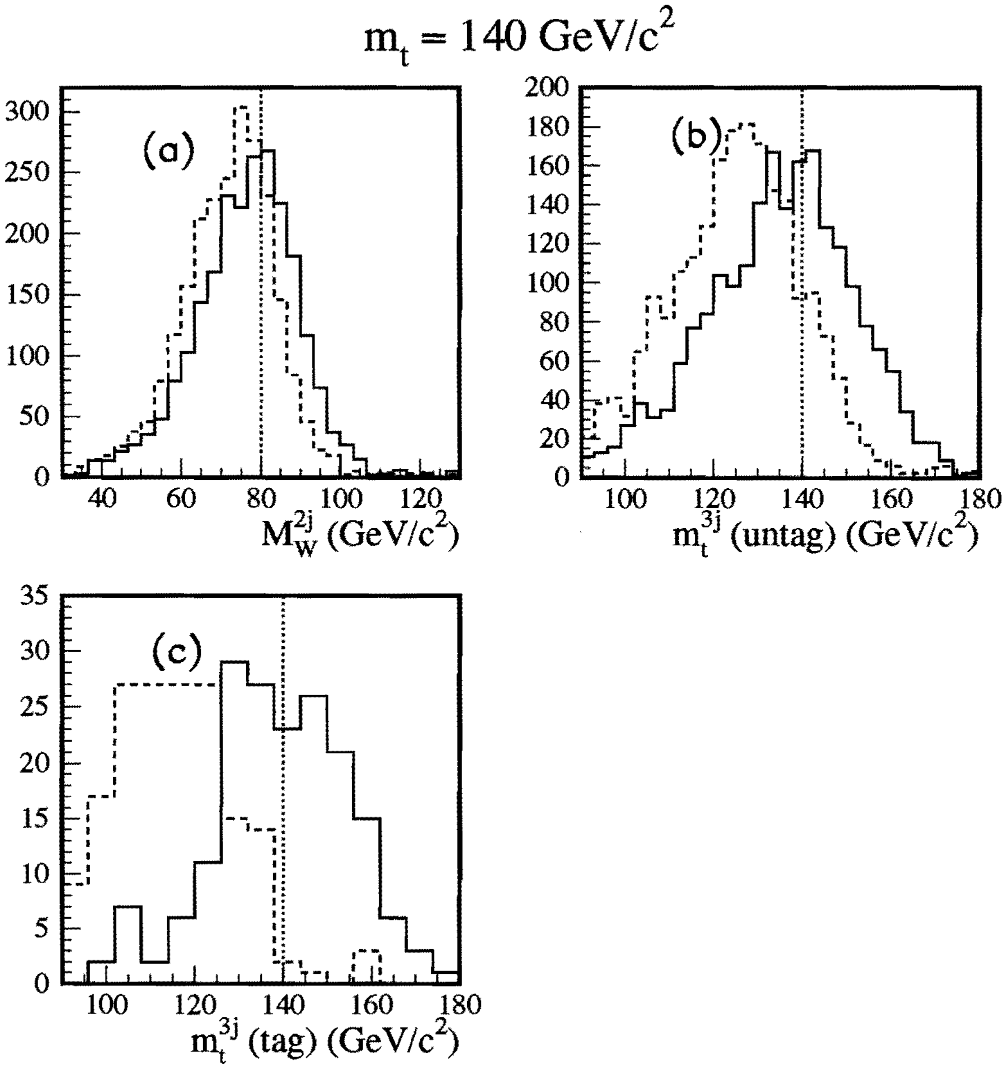

Figure 5.5: From HERWIG-generated $t\bar{t}$ Monte Carlo events with $m_t = 140\,\mathrm{GeV}/c^2$: (a) M_W^{2j} distribution (b) m_t^{3j} distribution when the b-quark jet is not tagged (c) m_t^{3j} distribution when the b-quark jet is tagged. The solid-line (dashed-line) histograms are the distributions after (before) the jet correction.

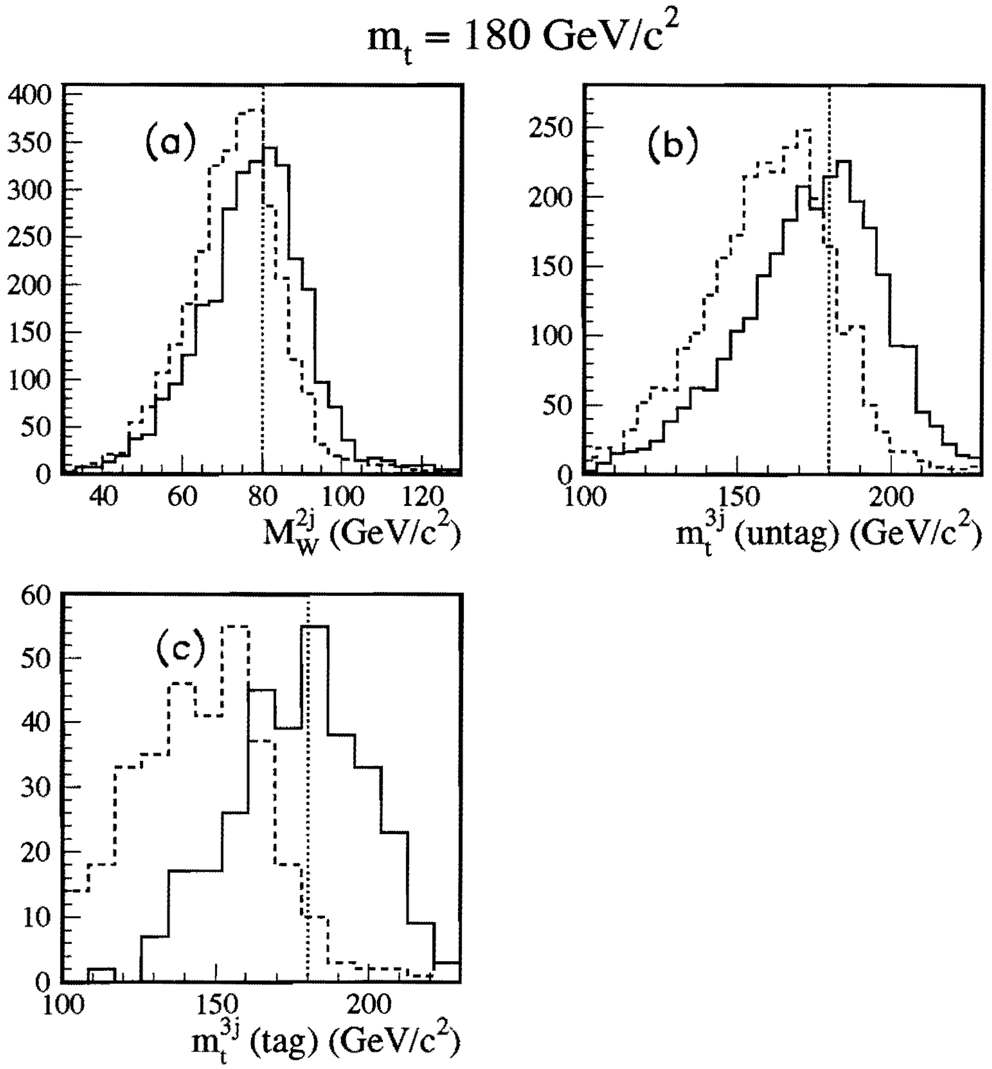

Figure 5.6: Similar to Figure 5.5, except $m_t = 180\,\mathrm{GeV}/c^2$ for the Monte Carlo.

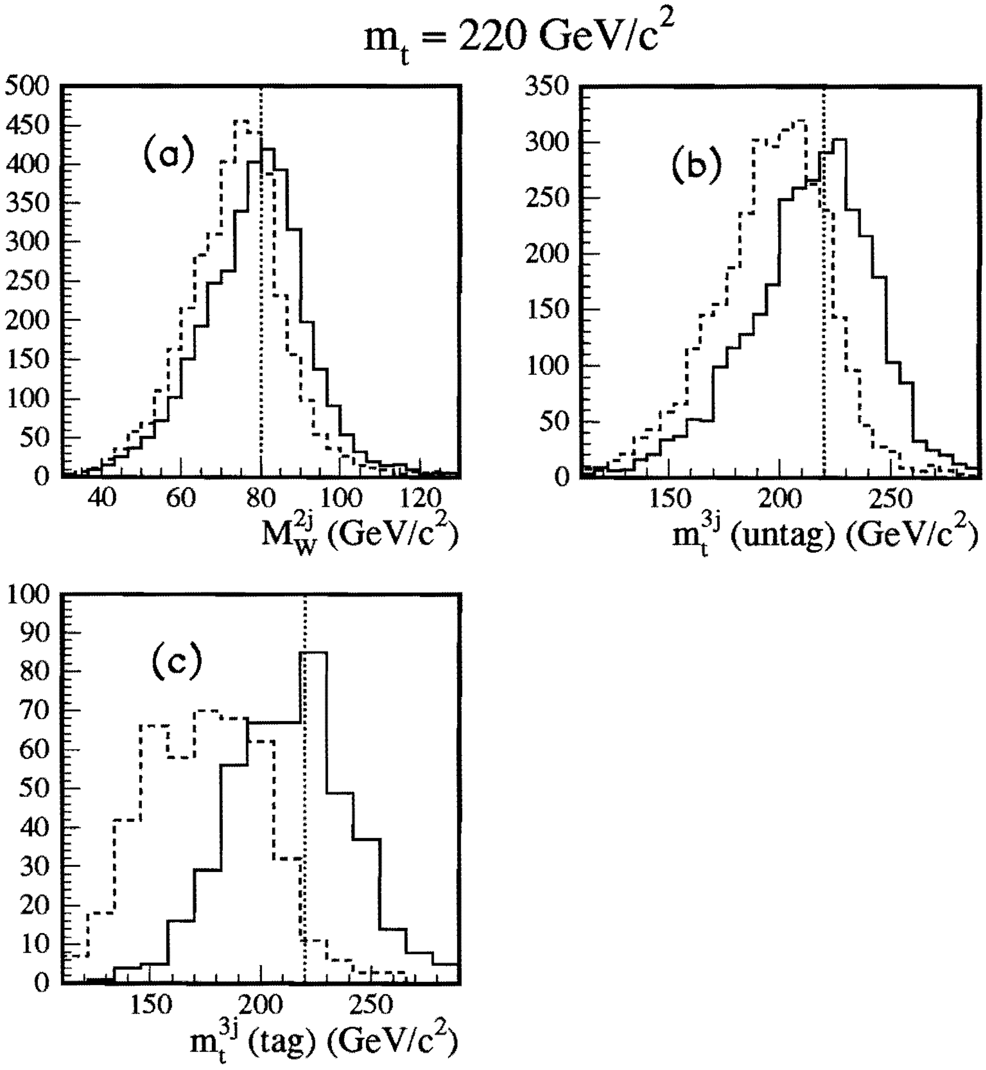

Figure 5.7: Similar to Figure 5.5, except $m_t = 220\,\mathrm{GeV}/c^2$ for the Monte Carlo.

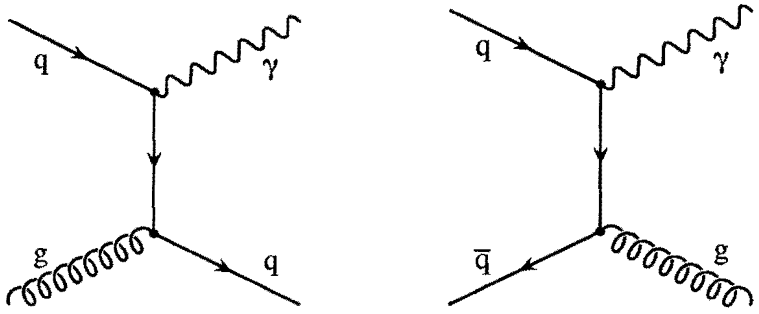

Figure 5.8: Processes of $\gamma + 1\,\text{jet}$ production, the events we choose for the jet energy scale study.

and jet transverse momentum. The event selection criteria are summarized as follows:

- Veto events with Main-Ring activity, noisy cells or multiple interactions;
- There must be no identified electron or muon;
- There is exactly one photon[1] in the regions fully covered by the EM calorimeter: $|\eta| < 1$ and $1.6 < |\eta| < 2.5$;
- A $\not{E}_T$ cut to remove the W events and those with undetected muons:

  $$\begin{aligned} \not{E}_T/E_T(\gamma) &< 1.2 \quad \text{if } E_T(\gamma) \leq 25\,\text{GeV} \\ \not{E}_T/E_T(\gamma) &< 0.65 \quad \text{if } E_T(\gamma) > 25\,\text{GeV}\,, \end{aligned}$$

  where $E_T(\gamma)$ is the photon E_T.
- There is only one reconstructed jet and the jet satisfies $E_T > 15\,\text{GeV}$ and $|\eta| < 2$, as required by the top quark analyses.
- The photon and the jet are back-to-back in ϕ : $2.942 < |\phi_{jet} - \phi_\gamma| < 3.342$, where ϕ_{jet} and ϕ_γ are the ϕ coordinate of the jet and the photon respectively.

---

[1] The photon ID is described in subsection 3.1.2, but here we have a tighter EM fraction cut, requiring it greater than 95%.

5.2.1 Energy Scale Correction

The jets in the $\gamma + 1\,\text{jet}$ sample have all been corrected for the out-of-cone radiation as described in the previous section (using the light quark correction parameters). Since the event consists of only a photon and a back-to-back jet and the EM scale is well calibrated, the deviation from unity ($\triangle S$) of the jet energy scale can be measured by averaging the fractional difference in E_T between the jet and the photon over a large number of events:

$$\triangle S = \left\langle \frac{E_T(\text{jet}) - E_T(\gamma)}{E_T(\gamma)} \right\rangle . \tag{5.5}$$

For this study, we limit the photon E_T in the range of 20 to 100 GeV. The lower limit is to avoid biases from the 15 GeV jet E_T threshold, and the higher limit is intended to maintain enough statistics as the photon E_T rises. This E_T range covers most of the jet E_T distribution for the $t\bar{t}$ events.

The scale deviation $\triangle S$ is calculated as a function of detector-η (η_{det}) for both data and MC $\gamma + 1\,\text{jet}$ samples. Detector-η is the recalculated η of the jet with the interaction z-vertex set to the center of the calorimeter or $z = 0$ as charted in Figure 2.8. Specified with η_{det}, jets from vertices far apart will have the same η_{det} if their energies are dominantly deposited in the same calorimeter region. By converting η to η_{det}, we are able to study the jet energy scale for various calorimeter regions.

The results are shown in Figure 5.9. As can be seen, the energy scales of data and Monte Carlo agree better in the Central Calorimeter ($|\eta_{det}| < 0.9$), but they become very different beyond that. In particular, the jet energy in the End Calorimeter ($|\eta_{det}| > 1.3$) region is significantly underestimated.

The MC plot in Figure 5.9 also provides a check on the out-of-cone radiation correction. In the correction, jets are binned in the η intervals between 0, 0.2, 0.6, 0.9, 1.3 and ∞. Therefore we expect the average $\triangle S$ in each bin be close to zero but its structure within the bin should remain, as shown in Figure 5.9 (bottom plot).

In order to minimize the systematic error in our analysis, we perform a further correction for the jet energy scale. The correction is based on the $\triangle S$ variation in η_{det} (Figure 5.9), and data and MC are corrected differently. Using the fit function

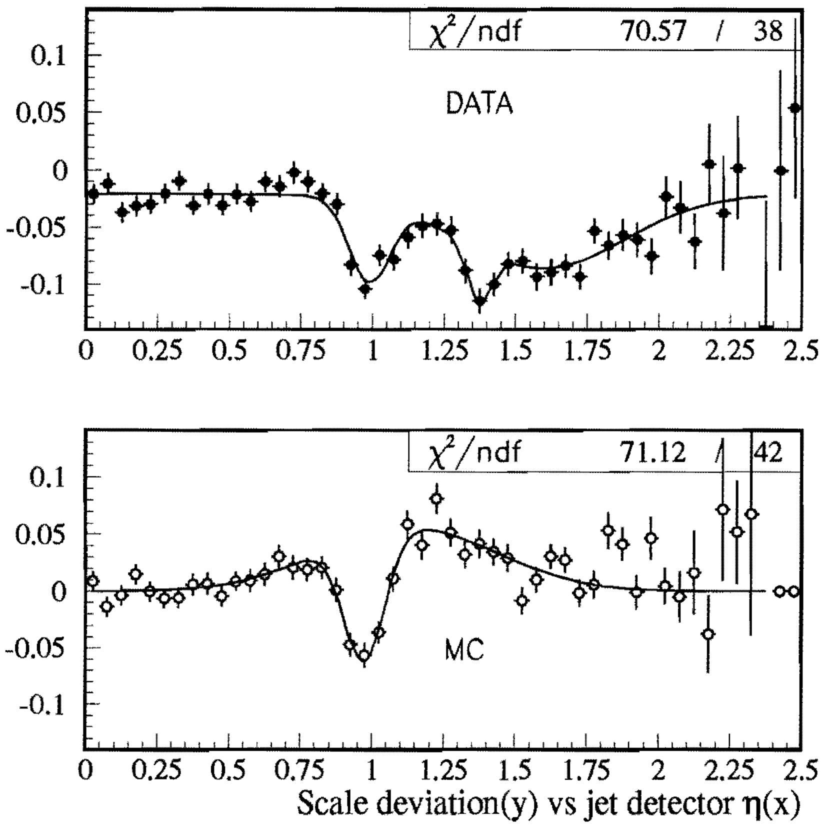

Figure 5.9: The energy scale deviation $\triangle S$ as a function of the η_{det} for data (top) and MC (bottom). Jets in the sample are of $E_T > 15\,\text{GeV}$ and $|\eta| < 2$. Photon E_T ranges from 20 to 100 GeV.

(triple-Gaussian + pedestal) for the η_{det}-dependent $\triangle S$, we correct the jet by scaling its 4-momentum by $1/(1+\triangle S)$ to flatten the energy scale variation in η_{det}.

5.2.2 Energy Scale Error

After the jets are corrected for the energy scale bias, we want to examine the variations of $\triangle S$ for various E_T ranges to check the correction result and to determine the uncertainty associated with the corrected energy scale. For both data and MC, $\triangle S$ as a function of photon E_T, denoted as $E_T(\gamma)$, is shown in Figure 5.10.

One should note that $E_T(\gamma)$ is approximately the true jet E_T, and it is impossible to introduce another correction to flatten out the variations in Figure 5.10 as we did in the previous subsection, because the true jet E_T is completely unknown in events other than $\gamma + 1\,\text{jet}$. We cannot replace $E_T(\gamma)$ in Figure 5.10 with $E_T(\text{jet})$ and correct for its structure, because $E_T(\text{jet})$ is a biased variable.

Figure 5.10 shows that the scale deviation, for both data and MC, is within 3-4% in the E_T range between 20 to 100 GeV. However, for the top mass analysis, in which the Monte Carlo is relied on to model the data, the difference between data and MC scales is what contributes to the systematic errors of the analysis.

Based on the $\triangle S$ variation in Figure 5.10, the difference between data and MC scales, i. e. $\triangle S_{\text{data}} - \triangle S_{\text{MC}}$, is shown as a function of $E_T(\gamma)$ in Figure 5.11. The error on the corrected jet energy scale is empirically estimated from Figure 5.11 to be $\pm(2.5\% + 0.5\,\text{GeV}/E_T)$. As can be seen, the error band sufficiently covers the data-MC scale differences for various E_T ranges.

5.3 Cross-checking the Corrections

All the jet corrections to be used for the top mass analysis in addition to CAFIX have been described in the previous two sections. Now we will use an independent Z + jets data sample, where the Z decays into two well-measured electrons, to cross-check the corrections. We apply the out-of-cone radiation and energy scale corrections to the jets and examine how the jets balance the Z in transverse momentum.

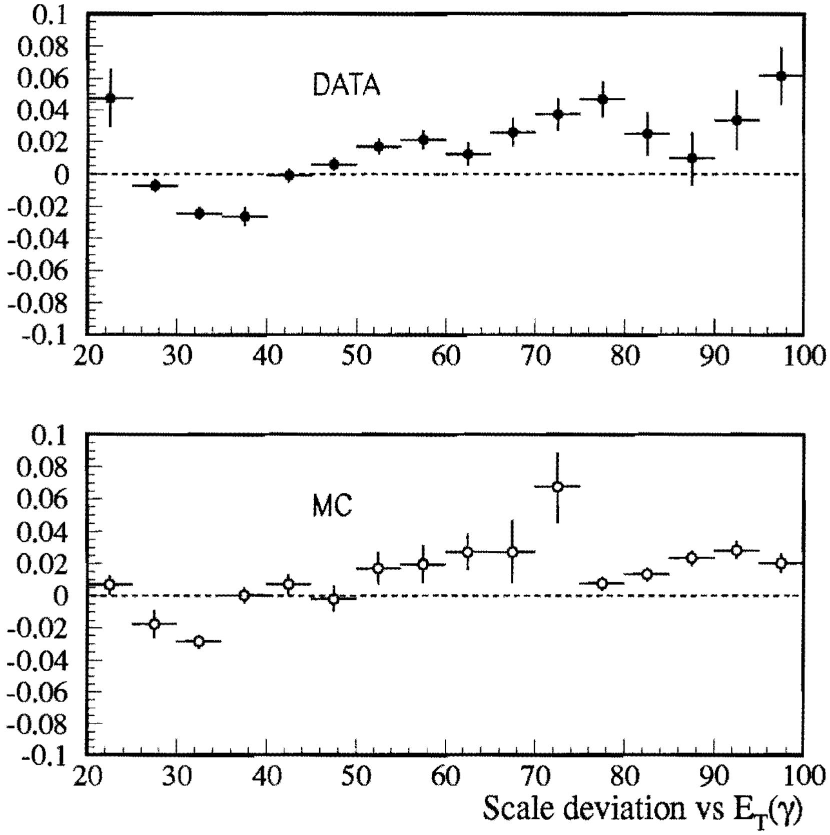

Figure 5.10: The scale deviation ΔS as a function of photon E_T ($\approx$ true jet E_T) after the energy scale correction, for data (top) and MC (bottom).

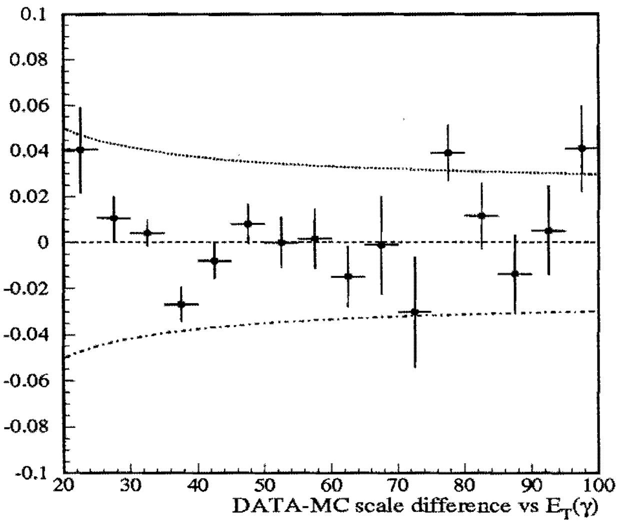

Figure 5.11: The energy scale difference between data and MC ($\Delta S_{data} - \Delta S_{MC}$) as a function of photon E_T. The curves covering the error $\pm(2.5\% + 0.5\,\text{GeV}/E_T)$ are also plotted.

In order to make sure the electron momenta are precisely measured, we particularly choose events whose reconstructed Z mass from the two electrons is between 86 and 96 GeV/c^2. We also require that at least one of the jets pass the jet requirement for the top mass analysis—$E_T > 15\,\text{GeV}$ and $|\eta| < 2$—so that the jets in the sample are comparable with those in the $t\bar{t}$ candidate events.

To check the corrected jet energies, we project the measured total transverse momentum $\sum_{\text{jets}} \vec{E}_T(\text{jet}) + \sum_{i=1,2} \vec{P}_T(e_i)$ to the bisector of the transverse momenta of two electrons[2] $\vec{P}_T(e_{i=1,2})$. The distribution of the projection is shown in Figure 5.13.

From the fitted Gaussian width and the number of events, we estimate the statistical error associated with the mean as $\sigma(\approx 6.2\,\text{GeV})/\sqrt{N(=437)}$ which is about 0.3 GeV. Therefore the fitted mean of $-0.14\,\text{GeV}$ is consistent with zero. We conclude that the corrected jet and the Z are balanced in transverse momentum and the function of our jet corrections is confirmed.

---

[2] The bisector is chosen as the projection axis in order to minimize possible biases when one of the electron's momentum is not precisely measured.

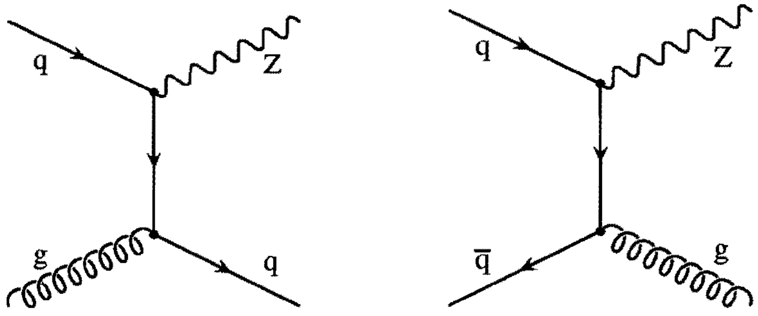

Figure 5.12: Processes of Z+1 jets prodution. Events like these make up a large portion of the inclusive $Z(\rightarrow ee)$ + jets sample used for cross-checking the jet corrections.

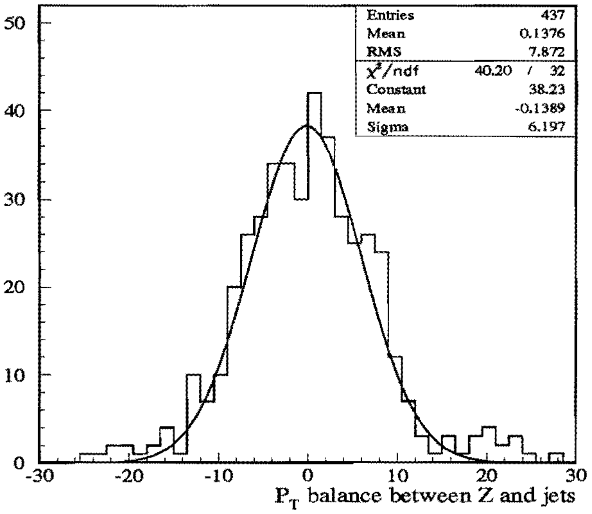

Figure 5.13: The transverse momentum balance in Z+jets events after applying all the corrections to the jets: the vector $\sum_{\text{jets}} \vec{E}_T(\text{jets}) + \vec{P}_T(Z)$ is projected to the bisector of the two electron $\vec{P}_T(e_i)$, $i = 1, 2$.

Chapter 6

Kinematic Fitting

In this chapter and the next, we will describe how the top mass is measured. This chapter will focus on the kinematic fitting for the reconstruction of the top mass on an event-by-event basis, and in the next chapter we will present a likelihood analysis from which the top mass can be extracted.

6.1 Fitting Method

The kinematic fitting attempts to reconstruct the unknown top quark mass from the observed objects in the event according to the kinematic constraints consistent with the $t\bar{t}$ hypothesis. The technique of kinematic fitting was first used some thirty years ago to fit multiple-vertex events in a bubble chamber experiment to an event hypothesis [68]. The principles in our fitting are similar, but the complexity of t and $\bar{t}$ decays certainly imposes a greater challenge.

6.1.1 General Algorithm

The $t\bar{t}$ event with a l+jets final state is depicted in Figure 6.1. In addition to the objects from the t and $\bar{t}$ decays, there are underlying spectator partons and possibly initial and final state gluon radiation as illustrated in Figure 6.2. Therefore, what we observe in the event is actually $t\bar{t} + X$, with X representing anything not originated from the t or $\bar{t}$.

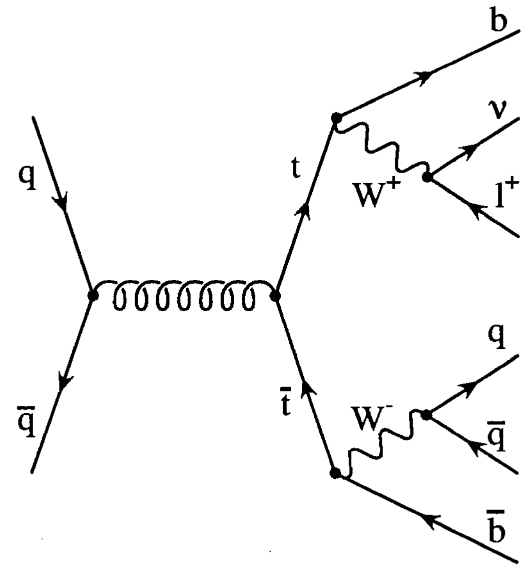

Figure 6.1: The process of $p\bar{p} \rightarrow t\bar{t} \rightarrow l + 4\,\mathrm{jets}$.

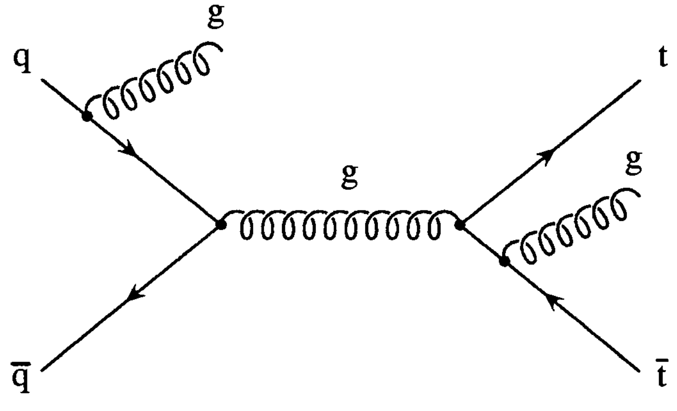

Figure 6.2: An example of gluon radiation in the $t\bar{t}$ production.

A $t\bar{t}$ event is subject to the following constraints:

$$\sum_i P_x^i = 0\,, \qquad \sum_i P_y^i = 0 \tag{6.1}$$

$$M(l,\nu_l) = M_W\,, \qquad M(q,\bar{q}) = M_W \tag{6.2}$$

$$M(l,\nu_l,b_1) = m_t\,, \qquad M(q,\bar{q},b_2) = m_t \tag{6.3}$$

Equation (6.1) represents the transverse momentum conservation—the transverse momentum in the $p\bar{p}$ collision is negligible; consequently the two components of total transverse momentum must equal to zero. The two-body weak decays of the W boson add (6.2) as two more constraints—the invariant mass[1] of the decay products must be consistent with the W mass ($80.2\,\mathrm{GeV}/c^2$). Finally, the top and the anti-top quarks—one decays hadronically and the other leptonically through the W—must have the same mass, as stated in (6.3).

The momentum of neutrino is inferred from the measured $\not{E}_T$, which is largely affected by jet energy and muon momentum resolutions. We will use $\not{E}_T$ as the initial neutrino transverse momentum, but the three components of neutrino momentum are treated as unknowns. Along with the top quark mass to be determined, we have four unknowns. Using the six kinematic constraints, we are able to perform an over-constrained fit (2C fit) to solve for the unknowns.

One big challenge in our analysis is that we have no knowledge of the identity of each jet—whether it is fragmented from a gluon or any flavor of quark. To perform the kinematic fit, there must be a hypothesis of the identities of jets. Our approach is to try every possible combination—assigning b, $\bar{b}$, q, $\bar{q}$ combinatorically to each of the jets—and take the solution of the best fitted combination (the one with the lowest χ^2) as our fitted result.

There can be more than four jets in a $t\bar{t}$ event due to gluon radiation, as shown in Figure 6.2. For an event with N jets ($N \geq 4$), the number of jet combinations is $\frac{N!}{2(N-4)!}$ if no jet is tagged. Note that the two sets of assignments with q and $\bar{q}$ switched have identical results, thus they count as one combination. If there is any

---

[1] The invariant mass of n objects, $O_1, O_2, \cdots, O_n$, denoted as $M(O_1, O_2, \cdots, O_n)$ is defined as $M^2(O_1, O_2, \cdots, O_n) = (\sum_{i=1}^n E_i)^2 - \left|\sum_{i=1}^n \vec{P}_i\right|^2$,where E_i and $\vec{P}_i$ are respectively the energy and momentum of object O_i.

	$N_{\text{tag}} = 0$ $N_c = \dfrac{N!}{2\,(N-4)!}$	$N_{\text{tag}} = 1$ $N_c = \dfrac{(N-1)!}{(N-4)!}$	$N_{\text{tag}} = 2$ $N_c = \dfrac{(N-2)!}{(N-4)!}$
$N = 4$	12	6	2
$N = 5$	60	24	6
$N = 6$	180	60	12
$N = 7$	420	120	20

Table 6.1: Numbers of jet combinations (N_c) when the event has N jets, out of which N_{tag} jets are tagged.

tagged jet, we require that the tagged jet be assigned as a b-quark jet, which reduces the number of combinations to $\frac{(N-1)!}{(N-4)!}$ if there is one tagged jet, and $\frac{(N-2)!}{(N-4)!}$ if two jets are tagged. As Table 6.1 shows, the number of jet combinations increases as the jet multiplicity gets higher. We find it most advantageous to use only the four leading jets (the four jets with highest E_T) for the kinematic fit. As will be seen later, in 3/4 of $t\bar{t} \rightarrow l + \text{jets}$ events, the four leading jets are from the final-state quarks—b, $\bar{b}$, q and $\bar{q}$. By choosing the four jets, we have the least combinations to fit and the best chance of obtaining a solution from the correct combination.

In order to avoid complications in the course of the kinematic fit, we use uncorrelated measurements to infer the momenta of the objects. For instance, for electrons and jets we use the measured energy, the polar (θ) and azimuthal (ϕ) angles, and the knowledge of their masses [44] to compute their 4-momenta. When the jet is assumed to be a light quark (u, d, c, s) jet, we use $m = 0.5\,\text{GeV}/c^2$ for its mass with the uncertainty $\sigma(m) = 0.5\,\text{GeV}/c^2$. When the jet is assigned as a b-quark jet, we use $m = 4.3\,\text{GeV}/c^2$ and $\sigma(m) = 0.3\,\text{GeV}/c^2$.

For muons, since what has been measured is the curvature of its track in the muon chamber, it is the inverse of its momentum ($1/p$) that has a Gaussian error. Therefore, in addition to θ and ϕ, we use $1/p$ rather than E to infer the muon 4-momentum.

The W mass ($M_W \approx 80.2\,\text{GeV}/c^2$) is used as two measured quantities: one for the leptonically decaying W, and the other for the hadronically decaying one. Since the

M_W measurement uncertainty ($\approx 0.3\,\mathrm{GeV}/c^2$) is far less than its Breit-Wigner width ($\approx 2.1\,\mathrm{GeV}/c^2$), we take the latter as the M_W resolution.

If the event has more than four jets, the jets not assigned as a of b, $\bar{b}$, q or $\bar{q}$ (the jets not among the leading four jets) are assumed to be gluon jets. Their combined transverse energy, denoted as $\vec{E}_T^G$, is computed in (6.4), where $\vec{E}_T^j$ stands for the transverse energy of the j-th jet.

The transverse momentum from the underlying event (the spectator partons), denoted as $\vec{E}_T^U$, is inferred by subtracting the E_T of the electron and jets from the total transverse energy deposited in the calorimeter, $-\vec{\not{E}}_T^{cal}$, as in (6.5).

$$\vec{E}_T^G = \sum_{j=5}^{N} \vec{E}_T^j \tag{6.4}$$

$$\begin{aligned}\vec{E}_T^U &= \sum_{i=1}^{cells} \vec{E}_T^i - \vec{E}_T^e - \sum_{j=1}^{N} \vec{E}_T^j \\ &= -\vec{\not{E}}_T^{cal} - \vec{E}_T^e - \sum_{j=1}^{N} \vec{E}_T^j \end{aligned}\tag{6.5}$$

With $\vec{E}_T^G$ and $\vec{E}_T^U$ determined, the constraints of (6.1) are equivalent to

$$\vec{P}_T^l + \vec{P}_T^\nu + \vec{E}_T^b + \vec{E}_T^{\bar{b}} + \vec{E}_T^q + \vec{E}_T^{\bar{q}} + \vec{E}_T^G + \vec{E}_T^U = \vec{0} \tag{6.6}$$

where the identity of each vector is denoted by its super index.

Overall there are 26 measured quantities used in the kinematic fit: $4 \times 4 = 16$ for the four jets, 4 for the charged lepton, 2 for $\vec{E}_T^G$, 2 for $\vec{E}_T^U$, and 2 for M_W. The resolutions of various measured quantities are summarized in Tables 6.2 and 6.3.

6.1.2 Finding the Solution

For each jet combination, the kinematic fit procedures are specified as follows. Let the column array $\mathbf{x_m}$ contain the measurements of the well-measured quantities (E, m, θ, ϕ of the electron, jets, etc.), and let another column array $\mathbf{y_m}$ contain the initial values of the unknowns or poorly-measured quantities (P_x^ν, P_y^ν, P_z^ν, m_t). Furthermore, let the fit results of $\mathbf{x_m}$ and $\mathbf{y_m}$ be $\mathbf{x}$ and $\mathbf{y}$ respectively.

Electrons	$\frac{\sigma^2(E)}{E^2} = 0.03^2 + \frac{0.15^2}{E}\,, \quad \sigma(\theta) = 0.005\,, \quad \sigma(\phi) = 0.005$
Muons	$\sigma^2\left(\frac{1}{p}\right) = \left(\frac{0.18}{p}\right)^2 + 0.01^2\,, \quad \sigma(\theta) = 0.005\,, \quad \sigma(\phi) = 0.005$
Jets	$\sigma(\theta) = 0.05\,, \quad \sigma(\phi) = 0.05$
Gluon Radiation	$\sigma(E_x^G) = 6\,\mathrm{GeV}\,, \quad \sigma(E_y^G) = 6\,\mathrm{GeV}$
Underlying Event	$\sigma(E_x^U) = 10\,\mathrm{GeV}\,, \quad \sigma(E_y^U) = 10\,\mathrm{GeV}$

Table 6.2: The resolutions of measurements used in the kinematic fit.

Light Quark Jets	$\frac{\sigma^2(E)}{E^2} = 0.064^2 + \frac{1.04^2}{E}$
Untagged b-jets	$\frac{\sigma^2(E)}{E^2} = 0.12^2 + \frac{1.08^2}{E}$
Tagged b-jets	$\frac{\sigma^2(E_h)}{E_h^2} = 0.064^2 + \frac{1.04^2}{E_h}$
	$\sigma^2(E_l) = 98.95 + e^{(6.833 - \frac{34.80}{P_\mu})}$
	$\sigma^2(E) = \sigma^2(E_l) + \sigma^2(E_h)$

Table 6.3: The jet energy resolutions used in the kinematic fit. Parameters are determined from the fits in Chapter 5. The jet energy E, the leptonic and hadronic energies in the b-quark's semi-leptonic decay, denoted as E_l and E_h respectively, and the tag muon momentum P_μ are in GeV or GeV/c.

The $\mathbf{x}$, $\mathbf{y}$ are reached by minimizing the χ^2 function:

$$\begin{aligned}\chi^2(\mathbf{x},\mathbf{y}) &\equiv (\mathbf{x}-\mathbf{x_m})^T\mathbf{G_x}(\mathbf{x}-\mathbf{x_m})+(\mathbf{y}-\mathbf{y_m})^T\mathbf{G_y}(\mathbf{y}-\mathbf{y_m}) \\ &= \mathbf{c}^T\,\mathbf{G_x}\,\mathbf{c}+\mathbf{d}^T\,\mathbf{G_y}\,\mathbf{d} \qquad (6.7)\end{aligned}$$

under the constraints (6.1–6.3), where $\mathbf{c}\equiv\mathbf{x}-\mathbf{x_m}$, $\mathbf{d}\equiv\mathbf{y}-\mathbf{y_m}$, and $\mathbf{G_x}$ and $\mathbf{G_y}$ are the error matrices for variables in $\mathbf{x}$ and $\mathbf{y}$ respectively. Since the measured quantities are specifically chosen to be uncorrelated, $\mathbf{G_x}$ is a diagonal matrix: $(G_x)_{ij}=\sigma_{x_i}^{-2}\,\delta_{ij}$. The variables in $\mathbf{y}$ are unknowns, so each of them has an infinite resolution: $\sigma_{y_i}=\infty$. Thus the matrix $\mathbf{G_y}$ is null, or $(G_y)_{ij}=0$, and equation (6.7) becomes

$$\chi^2(\mathbf{x})=\mathbf{c}^T\,\mathbf{G_x}\,\mathbf{c}\,. \qquad (6.8)$$

The two components of measured $\vec{\not{E}}_T$ are used as the initial P_x^ν and P_y^ν. But since P_z^ν is completely unmeasured, we can only solve its quadratic equation:

$$M^2(l,\nu)=M_W^2 \qquad (6.9)$$

using the initial P_x^ν and P_y^ν, and adopt its roots as possible initial P_z^ν. When (6.9) has two roots, as happens most of the time, we have to fit each combination twice, each time using one of the two roots as the initial P_z^ν, and keep the solution with a better fit. If (6.9) has no real root, we take the real part as the initial P_z^ν. As for the initial value of the last unknown—the top quark mass (m_t)—we always assign it to be 180 GeV/c^2.

The six constraints (6.1–6.3) can be rewritten as $f_i(\mathbf{x},\mathbf{y})=0$, $i=1,2,\cdots,6$ or simply $\mathbf{f}(\mathbf{x},\mathbf{y})=\mathbf{0}$. We introduce six Lagrange multipliers $\{\lambda_1,\lambda_2,\cdots,\lambda_6\}\equiv\boldsymbol{\lambda}$ in the definition of a new function $\mathcal{M}$:

$$\mathcal{M}=2\,\mathbf{f}^T\boldsymbol{\lambda}+\chi^2 \qquad (6.10)$$

so that the problem of solving for $\mathbf{x}$, $\mathbf{y}$ under the constraints is equivalent to solving the following equations:

$$\frac{\partial\mathcal{M}}{\partial\boldsymbol{\lambda}} = \mathbf{0} \qquad (6.11)$$

$$\frac{1}{2}\frac{\partial \mathcal{M}}{\partial \mathbf{x}} = \mathbf{B_x}\,\boldsymbol{\lambda} + \mathbf{G_x}\,\mathbf{c} = \mathbf{0} \tag{6.12}$$

$$\frac{1}{2}\frac{\partial \mathcal{M}}{\partial \mathbf{y}} = \mathbf{B_y}\,\boldsymbol{\lambda} = \mathbf{0}\,, \tag{6.13}$$

where

$$(B_x)_{ij} \equiv \frac{\partial f_j}{\partial x_i}\,, \qquad (B_y)_{ij} \equiv \frac{\partial f_j}{\partial y_i}\,. \tag{6.14}$$

Note that (6.11) restores the six kinematic constraints. The number of equations that (6.12) represents is equal to the number of well-measured quantities, which in our case is 26; while the number of equations in (6.13) is equal to the number of unknowns, which is 4. Altogether we have 36 equations in (6.11–6.13) that we have to solve for the 36 variables (6 Lagrange multipliers in $\boldsymbol{\lambda}$, 26 of the well-measured in $\mathbf{x}$, and 4 unknowns in $\mathbf{y}$).

The equations are difficult to solve analytically because they are not entirely linear. Our approach is to make approximations for $\mathbf{f}$, $\mathbf{B_x}$ and $\mathbf{B_y}$, and then iterate to find a convergent solution. More specifically, the constraints $\mathbf{f}$ are expanded around the trial solution $(\mathbf{x_0}, \mathbf{y_0})$ as:

$$\begin{aligned} \mathbf{0} &= \mathbf{f}(\mathbf{x},\mathbf{y}) \\ &\approx \mathbf{f}(\mathbf{x_0},\mathbf{y_0}) + \mathbf{B}_\mathbf{x}^T(\mathbf{x}-\mathbf{x_0}) + \mathbf{B}_\mathbf{y}^T(\mathbf{y}-\mathbf{y_0}) \\ &= \mathbf{f}(\mathbf{x_0},\mathbf{y_0}) + \mathbf{B}_\mathbf{x}^T(\mathbf{c}-\mathbf{c_0}) + \mathbf{B}_\mathbf{y}^T(\mathbf{d}-\mathbf{d_0})\,, \end{aligned} \tag{6.15}$$

where we have used $\mathbf{c_0} \equiv \mathbf{x_0} - \mathbf{x_m}$ and $\mathbf{d_0} \equiv \mathbf{y_0} - \mathbf{y_m}$, and the derivatives of $\mathbf{B_x}$ and $\mathbf{B_y}$ are approximated by numerical differentiation[2]. Initially, $(\mathbf{x_0}, \mathbf{y_0})$ is set to be $(\mathbf{x_m}, \mathbf{y_m})$, but as the fitting process evolves, it becomes the temporary $(\mathbf{x}, \mathbf{y})$ in the previous iteration.

Equation (6.15) can be rewritten as

$$\begin{aligned} \mathbf{B}_\mathbf{x}^T\mathbf{c} + \mathbf{B}_\mathbf{y}^T\mathbf{d} &\approx \mathbf{B}_\mathbf{x}^T\mathbf{c_0} + \mathbf{B}_\mathbf{y}^T\mathbf{d_0} - \mathbf{f}(\mathbf{x_0},\mathbf{y_0}) \\ &\equiv \mathbf{r}(\mathbf{x_0},\mathbf{y_0})\,. \end{aligned} \tag{6.16}$$

---

[2] Here we use the 5-point formula of numerical differentiation, in which the first derivative of a function $f(x)$ at x_0 is approximated as

$$f'(x_0) \approx \frac{1}{12h}\left[f(x_0-2h) - 8f(x_0-h) + 8f(x_0+h) - f(x_0+2h)\right],$$

where h is the infinitesimal displacement of x.

with the definition of array $\mathbf{r}$, which is a function of the trial solution $(\mathbf{x_0}, \mathbf{y_0})$. Now let us further define a 6×6 matrix

$$\mathbf{H} \equiv \mathbf{B_x}^T \mathbf{G_x}^{-1} \mathbf{B_x}\,, \tag{6.17}$$

then using (6.12) and (6.16) we have

$$-\mathbf{H}\,\boldsymbol{\lambda} + \mathbf{B_y}^T \mathbf{d} \approx \mathbf{r}(\mathbf{x_0}, \mathbf{y_0})\,. \tag{6.18}$$

Since $\mathbf{r}$ is a function of the trial solution, it can be computed, and thus allows us to solve the linear equations (6.13) and (6.18) combined:

$$\begin{pmatrix} -\mathbf{H} & \mathbf{B_y}^T \\ \mathbf{B_y} & \mathbf{O} \end{pmatrix} \begin{pmatrix} \boldsymbol{\lambda} \\ \mathbf{d} \end{pmatrix} = \begin{pmatrix} \mathbf{r} \\ \mathbf{0} \end{pmatrix}, \tag{6.19}$$

where $\mathbf{O}$ represents a 4×4 null matrix, and $\mathbf{0}$ a 4-dimensional array. Once the solution for $\boldsymbol{\lambda}$ and $\mathbf{d}$ ($\equiv \mathbf{y} - \mathbf{y_m}$) is reached, solution for $\mathbf{c}$ ($\equiv \mathbf{x} - \mathbf{x_m}$) can be immediately computed by (6.12) or

$$\mathbf{c} = -\mathbf{G_x}^{-1} \mathbf{B_x}\,\boldsymbol{\lambda}\,. \tag{6.20}$$

Then the temporary $(\mathbf{x}, \mathbf{y})$ will be used as $(\mathbf{x_0}, \mathbf{y_0})$ for the next iteration. The entire procedure is repeated until the solution approaches its convergence condition set to be $\Delta\chi^2 < 10^{-4}$ (the change of χ^2 between iterations less than 10^{-4}).

Although every possible jet combination of the event is fitted, not every combination will have a convergent solution. When the fit does converge, we keep the solution and its χ^2. In the end, we take the top mass solution of the best fitted combination (the one with the lowest χ^2) to be the fitted top mass for the event.

6.2 Fitting Monte Carlo $t\bar{t}$ Events

Using the method described in the previous section, samples of HERWIG-generated $t\bar{t} \rightarrow l$+jets events with different input top masses have been fitted. Not all the events will be fitted successfully—it is possible that no combination results in a convergent solution. The fit efficiencies (the probability that an event being fitted successfully) for both tagged and untagged events of different top masses are listed in Table 6.4.

m_t	140 GeV/c^2	160 GeV/c^2	180 GeV/c^2	200 GeV/c^2
Untagged	$(97.5 \pm 0.5)\%$	$(97.1 \pm 0.3)\%$	$(95.2 \pm 0.3)\%$	$(93.4 \pm 0.5)\%$
Tagged	$(89.1 \pm 1.6)\%$	$(89.0 \pm 0.9)\%$	$(84.8 \pm 0.9)\%$	$(82.8 \pm 1.2)\%$

Table 6.4: The kinematic fit efficiencies (the probabilities of an event being fitted successfully) for samples with various top masses. The errors are only statistical.

m_t	140 GeV/c^2	160 GeV/c^2	180 GeV/c^2	200 GeV/c^2
	$(70.6 \pm 1.0)\%$	$(73.4 \pm 0.6)\%$	$(74.8 \pm 0.5)\%$	$(77.5 \pm 0.6)\%$

Table 6.5: The fractions of $t\bar{t} \to l +$jets events that the four highest E_T jets are the correct selection—no gluon jet among them—for samples with various top masses.

The tagged events generally have a lower efficiency because they do not have as many combinations as those of the untagged (see Table 6.1).

The overall fitted top mass distributions (tagged and untagged combined) are shown in Figure 6.3 for samples with different top masses. As can be seen, the peaks of the fitted top mass occur at the true value. However, the distributions are broad and their shapes are not Gaussian.

When only the correct jet combination is used in the kinematic fit, the results, shown in Figure 6.4, not only have a much better resolution, but the distributions become more Gaussian-like. This indicates that the asymmetric tails and the broadened distributions in Figure 6.3 are a result of incorrect jet combinations. In other words, those events whose best fitted combination is not the correct one are largely responsible for the width of the fitted top mass distribution.

m_t	140 GeV/c^2	160 GeV/c^2	180 GeV/c^2	200 GeV/c^2
Untagged	$(29.8 \pm 1.4)\%$	$(32.4 \pm 0.8)\%$	$(35.3 \pm 0.8)\%$	$(38.5 \pm 1.0)\%$
Tagged	$(35.9 \pm 2.7)\%$	$(41.5 \pm 1.5)\%$	$(41.6 \pm 1.3)\%$	$(42.5 \pm 1.7)\%$

Table 6.6: The fractions of successfully fitted events that the lowest χ^2 solution results from the correct combination, given that the four jets participating in the fit are the right ones, for different top masses and for tagged and untagged events.

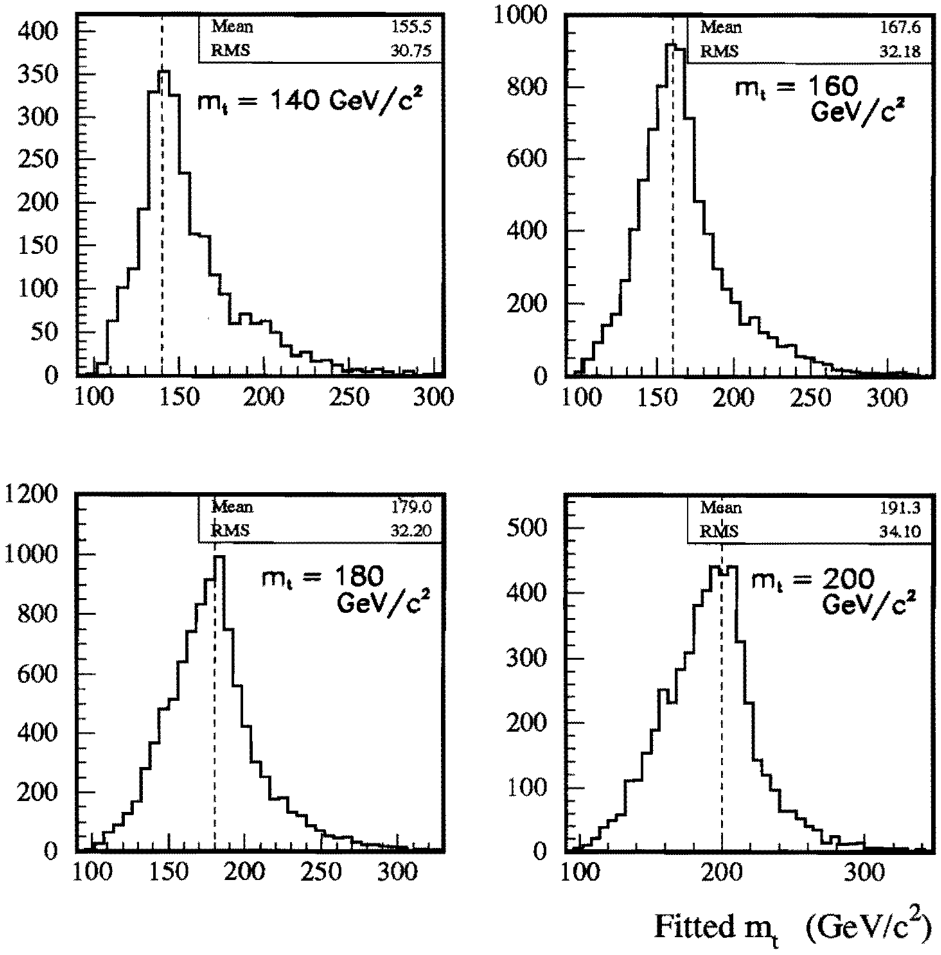

Figure 6.3: The distributions of the fitted top mass (the lowest χ^2 solution among all the possible jet combinations) for the $t\bar{t} \to l +$jets Monte Carlo (HERWIG-modeled) generated with various top masses. The true top mass value is marked with a dashed vertical line.

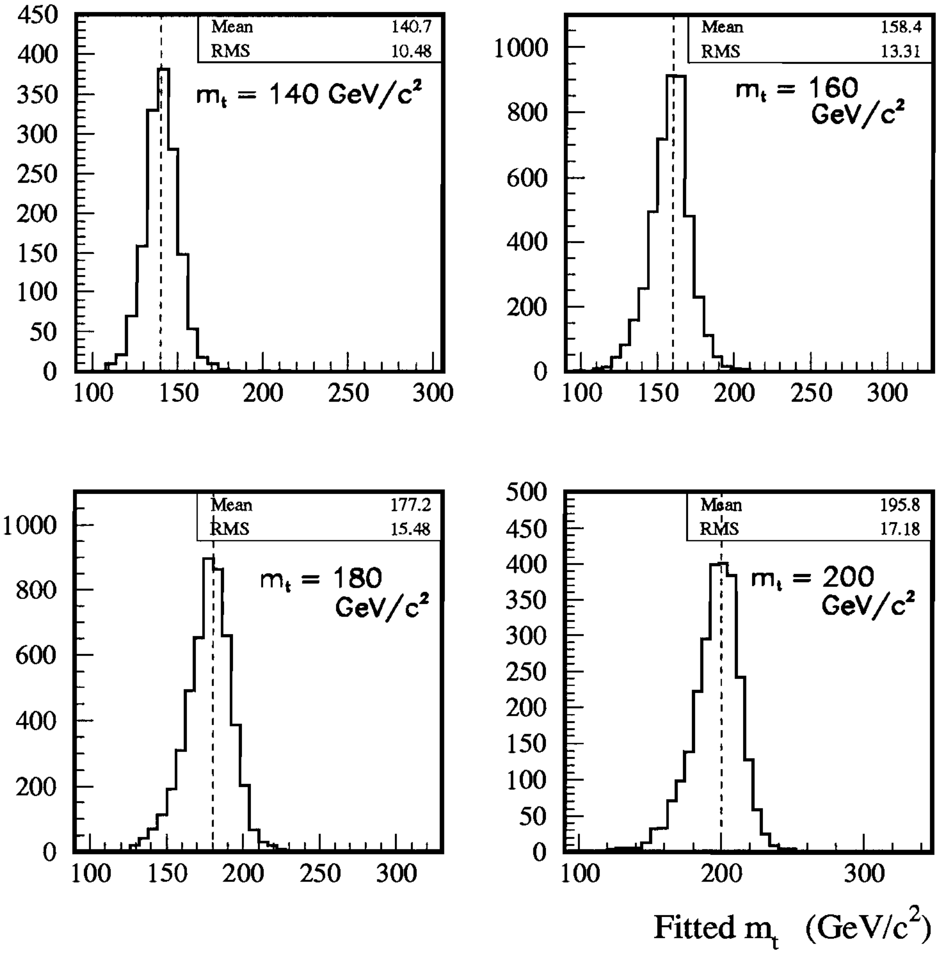

Figure 6.4: The distributions of the fitted top mass using the correct jet combination. The samples are the same as those in Figure 6.3.

Two factors contribute to the jets in an event being assigned incorrectly. The first one is the gluon radiation which results in extra jets. When a gluon jet has an E_T exceeding that of a quark jet from t or $\bar{t}$ decay, the choice of the four highest E_T jets for the kinematic fit is wrong in the first place. The fraction of signal events that the four leading jets are a correct selection is listed in Table 6.5 for samples generated with different top masses.

The second factor is the jet combinatorics itself. Even if the correct four jets are picked from the beginning, there are many combinations to fit (12 combinations if no tagged jet, 6 combinations if one jet is tagged), and very often the solution with the lowest χ^2 does not result from the correct combination. If the four chosen jets correspond to four quark-jets from $t\bar{t}$ decay and the event is fitted successfully, the probability that the fit results in the right combination ranges from 30 to 40% as shown in Table 6.6. As expected, the tagged events in general have a higher probability because of their advantage in combinatorics.

Nonetheless, having a tagged jet does not improve much in the fitted top mass resolution. This can be clearly seen by comparing the fitted top mass distributions for the untagged (Figure 6.5) and the tagged events (Figure 6.6). That is because, although the tagged events have less combinations to fit and thus a better chance to get the right combination, the neutrino energy in the b-quark decay is not measured and thus the energy resolution of the tagged jet becomes worse than the untagged jets. The result of the kinematic fit is therefore affected by the degraded measurements on the tagged jet, offsetting its combinatoric advantages.

6.3 Expectation for Background

In addition to fitting $t\bar{t}$ Monte Carlo events, we need to know the fitted result of backgrounds to provide an accurate modeling for the extraction of the top mass. Using the same method, we fit both the W+jets and QCD background events (how these samples are generated is explained in Section 3.3) that passed the selection criteria. As shown in Figure 6.7, both backgrounds have a similar shape which is characterized by a low-mass peak and a high-mass tail. The fit efficiencies for various

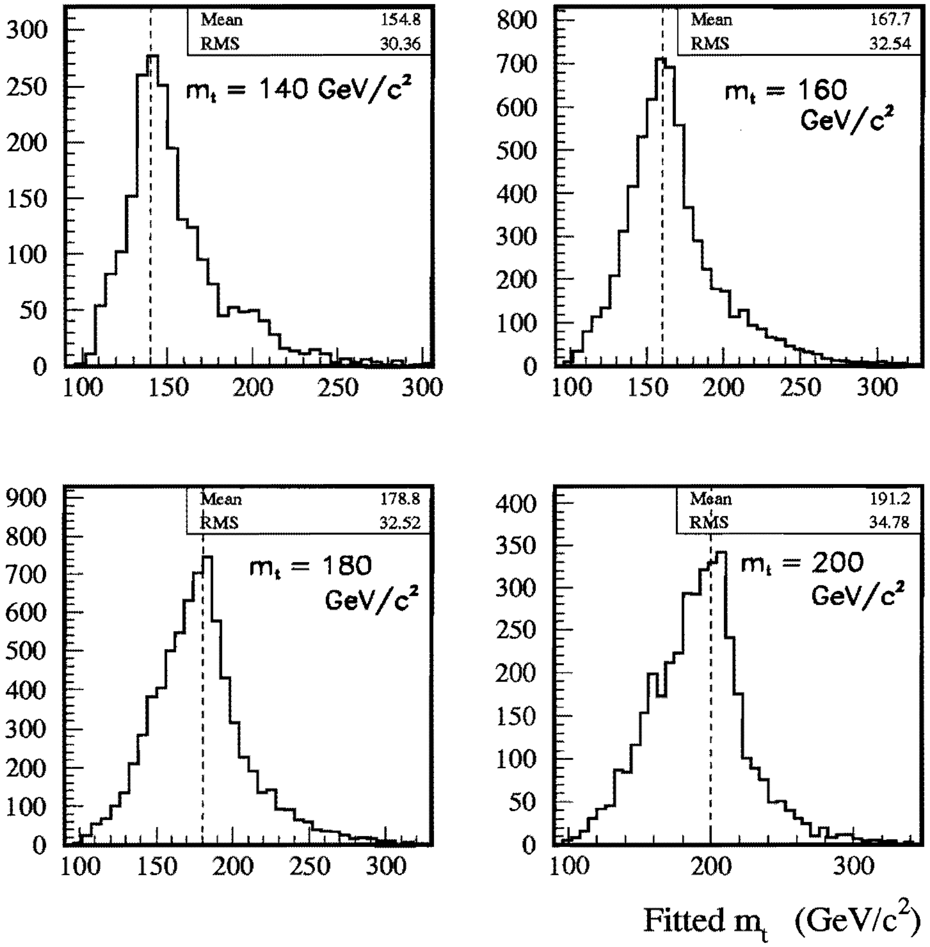

Figure 6.5: The distributions of the fitted top mass for the events without tagged jets. The samples are the same as those in Figure 6.3.

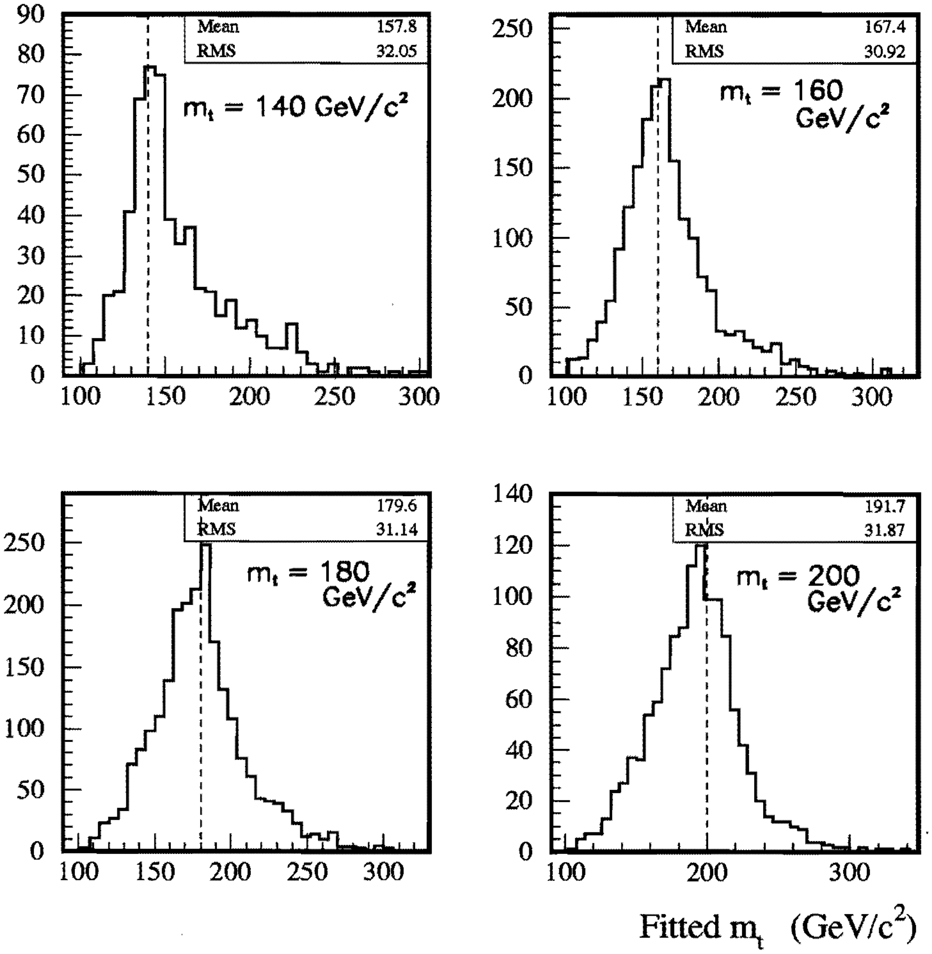

Figure 6.6: The distributions of the fitted top mass for the events having at least one tagged jet. The samples are the same as those in Figure 6.3.

channels are listed in Table 6.7, and will be used to estimate the background number in the final sample.

6.4 Fit Results of Candidate Events

The results of the kinematic fit for the candidate sample are presented in Table 6.8. Thirty-four out of 35 candidates are fitted successfully. Their fitted top mass distribution is shown in Figure 6.8.

Using the background kinematic fit efficiencies in Table 6.7, we calculate the backgrounds in the 34-event final sample from the pre-fit estimates (Table 4.5), and the results are summarized in Table 6.9.

With the background numbers calculated and samples of both backgrounds and signals fitted, we are ready to move on to our final task: the extraction of the top mass.

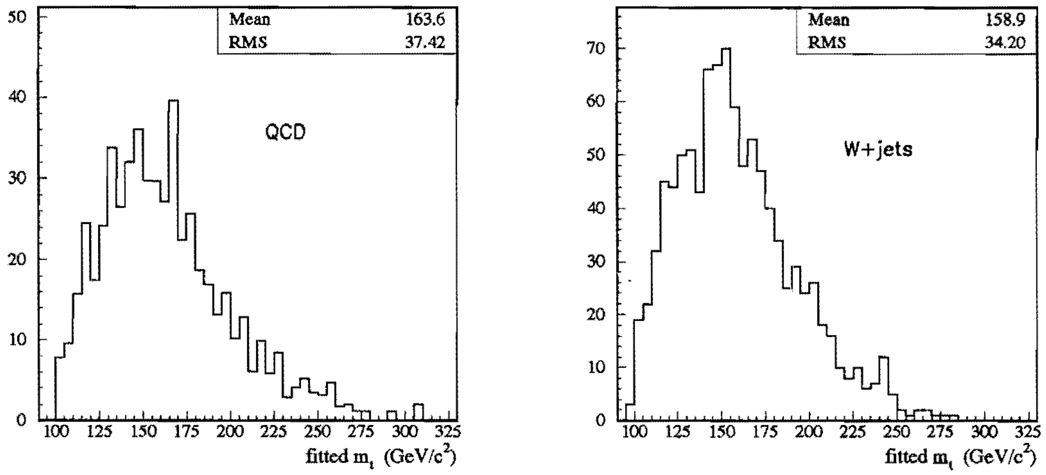

Figure 6.7: The fitted top mass distributions for QCD (determined from data) and W + jets (simulated by VECBOS) background events.

	e+jets		μ+jets	
	efficiency	success/total	efficiency	success/total
W + jets bkg	$(94.52 \pm 1.16)\%$	362/383	$(94.64 \pm 1.06)\%$	424/448
QCD bkg	$(96.69 \pm 1.33)\%$	175/181	$(93.01 \pm 1.68)\%$	213/229

	e+jets/μ		μ+jets/μ	
	efficiency	success/total	efficiency	success/total
W + jets bkg	$(80.00 \pm 6.76)\%$	28/35	$(87.10 \pm 6.02)\%$	27/31
QCD bkg	$(81.25 \pm 4.36)\%$	65/80	$(75.93 \pm 4.11)\%$	82/108

Table 6.7: The efficiencies of the kinematic fit for background events passing the selection criteria.

Run-Event	1st-m_t^{fit}	1st-χ^2	2nd-m_t^{fit}	2nd-χ^2	3rd-m_t^{fit}	3rd-χ^2
e+jets channel						
63066-13373	204.0	1.067	165.6	3.222	166.9	3.404
81949-12380	134.0	1.447	162.5	1.492	124.2	1.817
85917-22	143.8	98.47	—	—	—	—
86601-33128	182.4	0.949	248.5	5.817	244.0	6.365
87063-39091	191.7	3.776	126.3	25.07	145.1	28.06
88045-35311	177.8	2.167	186.4	2.636	180.1	3.946
89484-11741	145.5	0.891	134.6	1.069	173.6	1.163
89708-24871	—	—	—	—	—	—
89936-6306	220.5	0.714	219.1	4.030	248.3	4.252
89972-13657	173.0	6.599	144.1	11.50	192.6	20.34
92673-4679	178.8	31.38	174.1	31.65	191.6	68.20
96329-13811	253.4	36.68	242.1	45.90	167.4	77.36
96738-27592	237.3	7.014	190.3	7.613	196.0	14.69
e+jets/μ channel						
62199-13305	177.3	24.91	207.3	26.63	179.0	39.15
85129-19079	126.3	1.687	125.1	3.204	138.5	3.904
86570-8642	144.3	0.425	141.7	1.997	141.8	5.786
89372-12467	123.9	24.60	—	—	—	—
μ+jets channel						
63183-13926	134.6	1.248	122.5	4.020	137.5	9.463
63740-14197	185.9	2.285	160.0	7.468	168.7	7.875
81909-11966	174.0	2.842	—	—	—	—
82694-25595	112.8	1.309	149.8	8.637	147.2	9.544
84696-29253	222.2	1.120	220.4	3.107	173.6	17.45
87063-14368	182.7	0.012	159.7	2.887	143.6	6.276
87820-6196	174.7	17.24	165.5	17.47	149.1	23.85
88464-2832	152.4	0.313	131.1	0.412	128.0	0.701
88530-7800	151.3	0.077	191.4	0.484	152.2	3.966
89943-19016	163.7	0.021	154.4	0.027	160.8	0.533
90660-20166	110.2	49.11	124.9	63.02	—	—
90690-12392	152.2	0.929	124.5	12.39	124.9	14.56
92114-1243	188.6	12.58	188.4	17.40	185.3	21.14
92714-12581	144.2	3.903	187.8	3.957	146.1	4.707
96399-32921	174.1	0.052	174.8	0.280	166.5	1.231
96591-39318	174.5	0.483	148.1	4.371	185.8	6.719
μ+jets/μ channel						
58203-4980	138.0	0.257	195.2	0.333	195.0	0.617
92704-14022	175.5	0.122	148.6	0.856	172.7	7.951

Table 6.8: The three best fitted top masses and the corresponding χ^2 of candidate events (specified in run number and event number).

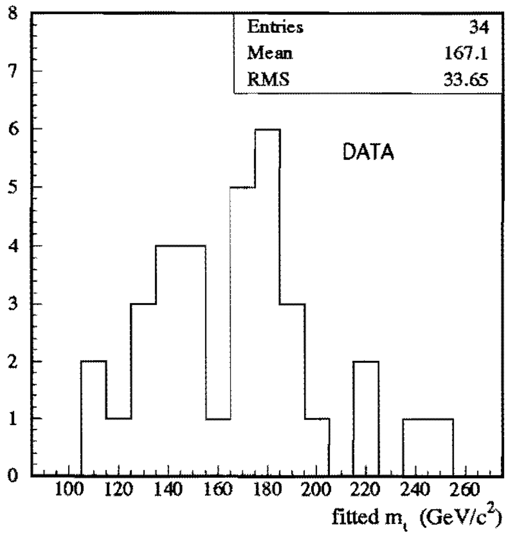

Figure 6.8: The fitted top mass distribution of the 34 candidate events.

	e+jets	μ+jets	e+jets/μ	μ+jets/μ	All l+jets
W +jets bkg	4.85 ± 0.56	4.12 ± 1.24	0.79 ± 0.87	0.73 ± 0.17	10.48 ± 1.62
QCD bkg	1.20 ± 0.38	2.22 ± 0.81	0.21 ± 0.64	0.82 ± 0.23	4.44 ± 1.13
Total bkg	6.05 ± 0.68	6.33 ± 1.48	1.00 ± 1.08	1.54 ± 0.28	14.93 ± 1.98
Observed events	12	16	4	2	34

Table 6.9: The estimated backgrounds and observed events after the kinematic fit (one event failed the fit). The background estimation is based on the kinematic fit efficiencies in Table 6.7 and the backgrounds estimated before the kinematic fit in Table 4.5.

Chapter 7

Top Mass Extraction

In this chapter, we will introduce a likelihood analysis that makes the extraction of the top mass possible and Monte Carlo tests that justify the likelihood method. Finally, studies of systematic errors associated with the measurement will also be presented.

7.1 Likelihood Analysis

In the previous chapter, we have presented the results of a kinematic fit for Monte Carlo $t\bar{t}$ events, backgrounds, and candidates. With the knowledge of these fitted top mass (m_t^{fit}) distributions, we are able to determine the most likely top mass consistent with our data. In the following, we will first calculate the likelihood at different top mass values, then we will introduce the algorithm to extract the top mass based on the likelihood calculation.

For signal and background modeling, we have to normalize the m_t^{fit} distributions and convert them to probability density functions. It is done by multiplying the contents of each bin by the normalization factor $\mathcal{K}$:

$$\mathcal{K} = \frac{1}{w\,n}, \tag{7.1}$$

where w is the bin width and n is the number of total entries, so that the normalized contents approximate the probability densities.

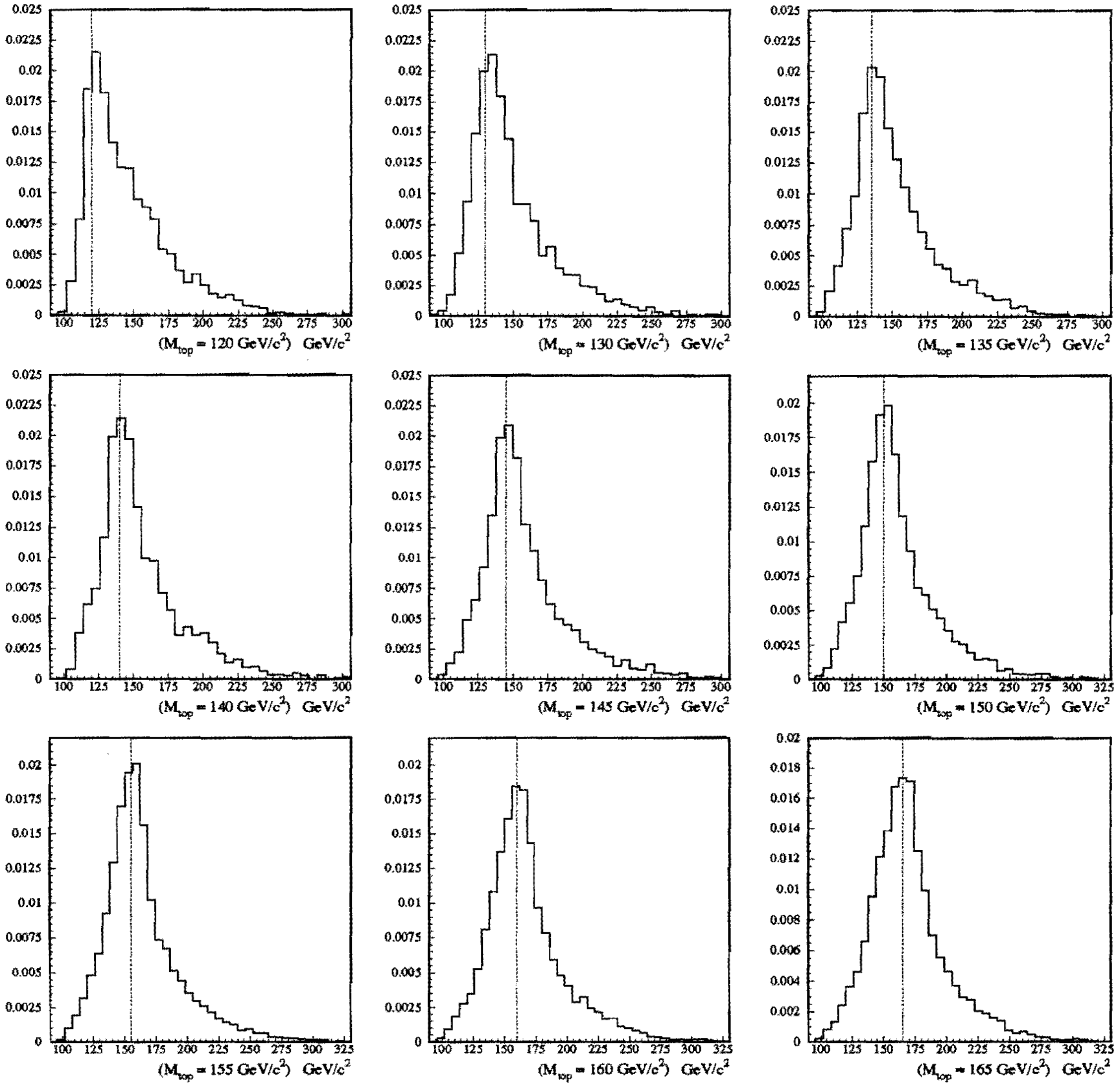

Figure 7.1: Probability density functions of the fitted top mass (m_t^{fit}) for Monte Carlo $t\bar{t}$ events with top mass 120, 130, 135, 140, 145, 150, 155, 160, and 165 GeV/c^2 respectively. The true top mass is marked by a vertical line.

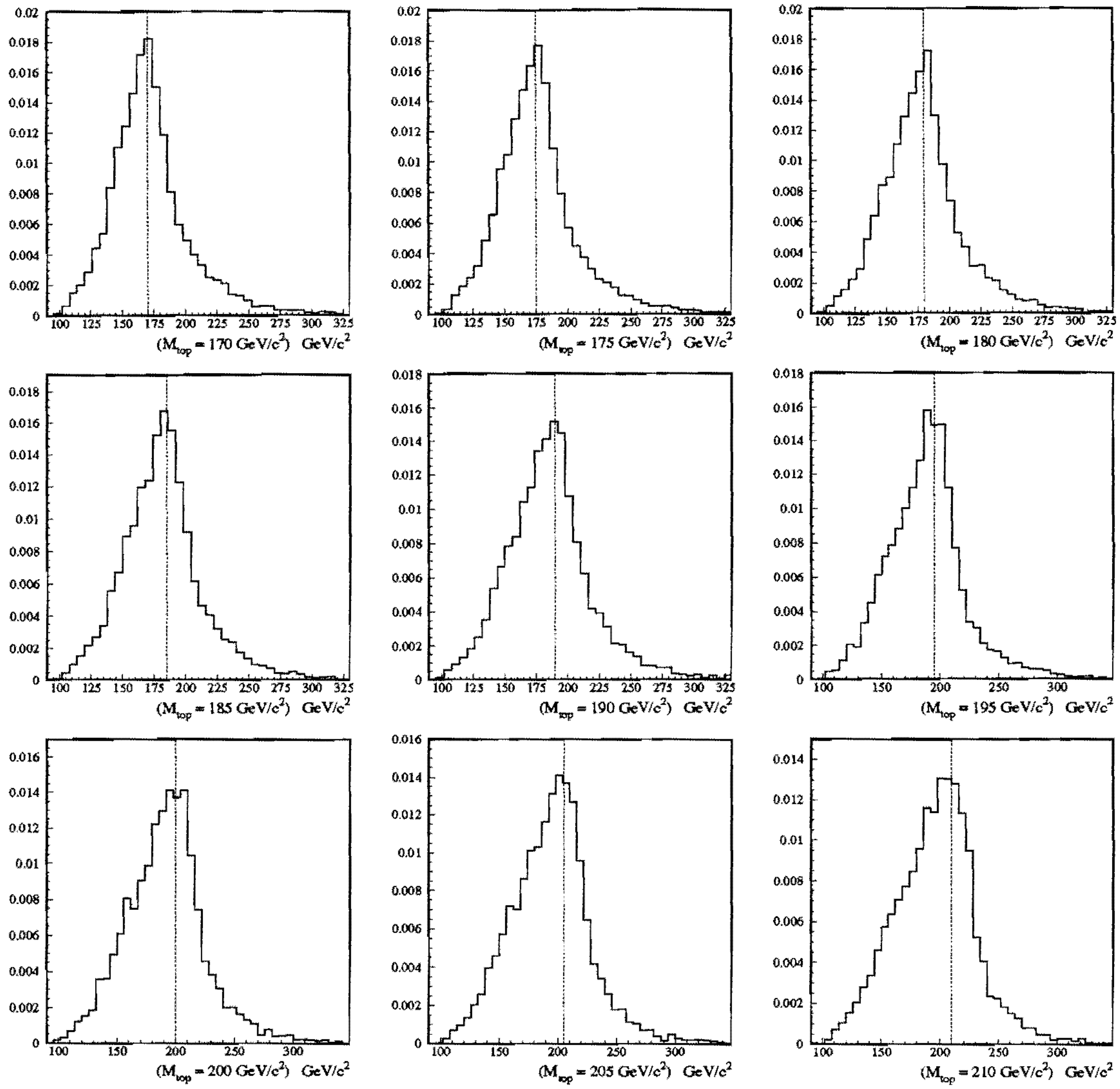

Figure 7.2: Probability density functions of m_t^{fit} for Monte Carlo $t\bar{t}$ events with top mass 170, 175, 180, 185, 190, 195, 200, 205, and 210 GeV/c^2 respectively.

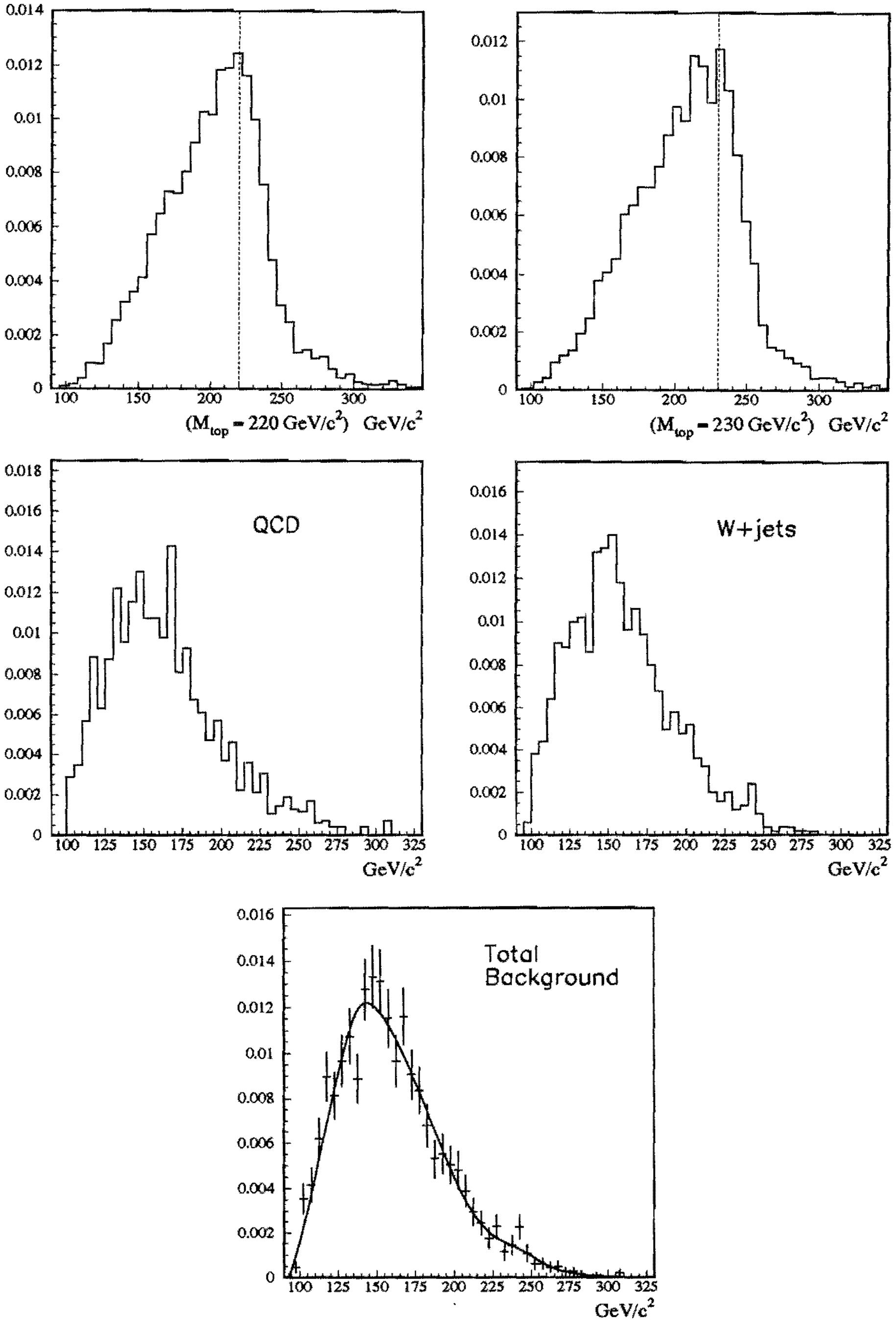

Figure 7.3: Probability density functions of m_t^{fit} for Monte Carlo $t\bar{t}$ events with top mass 220 and 230 GeV/c^2 respectively and for QCD, W+jets and the combined background.

Several Monte Carlo $t\bar{t}$ samples of various top masses[1], ranging from 110 to 230 GeV/c^2, have been generated to provide signal modeling at a variety of m_t. Their m_t^{fit} probability density functions will be used in the likelihood calculation, and some of them are shown in Figures 7.1, 7.2, and 7.3. Similarly, the m_t^{fit} probability density functions for QCD and W +jets backgrounds are derived from their m_t^{fit} distributions. The final background modeling is a mixture of QCD and W +jets contributions weighted by their fraction in the total background of the candidate sample (based on Table 6.9).

In calculating the likelihood of consistency between the observed and the expected m_t^{fit} distributions of events, let us denote the m_t^{fit} probability density function for signal of top mass m_t as $P_s(m_t, m_t^{fit})$, and that for background as $P_b(m_t^{fit})$. Furthermore, let n_s and n_b be the nominal (i. e. the mean of the Poisson distribution) number of signal and background respectively, while n_B and σ_B the estimated number of background and its error respectively. For the observed N candidate events, the likelihood is:

$$\begin{aligned}\mathcal{L}(m_t, n_s, n_b) &= \exp\left(-\frac{(n_b - n_B)^2}{2\,\sigma_B}\right)\left\{\frac{e^{-(n_s+n_b)}(n_s+n_b)^N}{N!}\right\} \\ &\quad \prod_{i=1}^{N}\left(\frac{n_s P_s\left(m_t, m_t^i\right) + n_b P_b\left(m_t^i\right)}{n_s + n_b}\right) . \end{aligned} \tag{7.2}$$

The exponential term allows the background number to fluctuate in a Gaussian distribution of width σ_B. The second term reflects the nature of Poisson fluctuations on the number of observed events N. The last term takes into account the fitted top masses of candidate events. At each m_t where Monte Carlo samples are available, the likelihood is maximized with respect to n_s and n_b. (It is implemented by minimizing $-\ln\mathcal{L}$ using MINUIT [69].) The result is shown in Figure 7.4(Left) where the minimized $-\ln\mathcal{L}$ at each m_t is plotted. Due to limited statistics in both signal and background modeling, certain errors may occur on the binned probability densities; therefore, to some extent the calculated likelihood is influenced by statistical fluctuation.

---

[1] Monte Carlo samples are available for top masses 110, 120, 130, 135, 140, 145, 150, 155, 160, 162, 165, 168, 170, 172, 175, 178, 180, 185, 190, 195, 200, 205, 210, 220, and 230 GeV/c^2.

To determine the most likely top mass and its statistical uncertainty, we interpolate the data points with a continuous curve. Assuming that the likelihood has a Gaussian error, we fit Figure 7.4(Left) with a quadratic function of m_t (since the exponent of a Gaussian distribution is quadratic). Apparently not the entire range of m_t can be fitted well. However, for our purpose, we only need to fit a range large enough that the statistical error of the measured top mass can be determined. Our algorithm is to use the 9 data points with the lowest $-\ln\mathcal{L}$ to perform the quadratic fit.

The central value of the m_t measurement is where the minimum of $-\ln\mathcal{L}$ occurs. The statistical error, equivalent to the Gaussian width of $\mathcal{L}$, is determined by the distance from the central value to either of the two points where $-\ln\mathcal{L}$ is 0.5 larger than the minimum. As shown in Figure 7.4, the result of the quadratic fit indicates that the top mass lies within 177.0 ± 7.3 GeV/c^2. The fitted number of signal and background at the central value of m_t are $n_s = 19.3$ and $n_b = 14.9$ (from a linear interpolation between two adjacent data points next to the central value).

The expected m_t^{fit} distribution can be constructed from the signal and background models using the fitted n_s and n_b, and is compared with the observed distribution in Figure 7.4(Right), where the signal contribution is modeled by the $m_t = 178\,\mathrm{GeV}/c^2$ Monte Carlo (the closest available to the central value). It appears that the observed distribution is fairly consistent with the expectation.

As a cross-check, we redo the likelihood analysis without constraining the background number to our estimate—by simply removing the exponential term involving n_B and σ_B in (7.2) in the likelihood calculation. The quadratic fit, as shown in Figure 7.5, yields $m_t = 177.3 \pm 7.7\,\mathrm{GeV}/c^2$ and $n_s = 20.4$, $n_b = 13.6$, a result similar to that with the background number constrained.

7.2 Monte Carlo Test

The likelihood method for the top mass extraction can be tested by a large number of Monte Carlo experiments. In each experiment, we generate N_s to be the number of signal events and N_b the number of background events from Poisson distributions

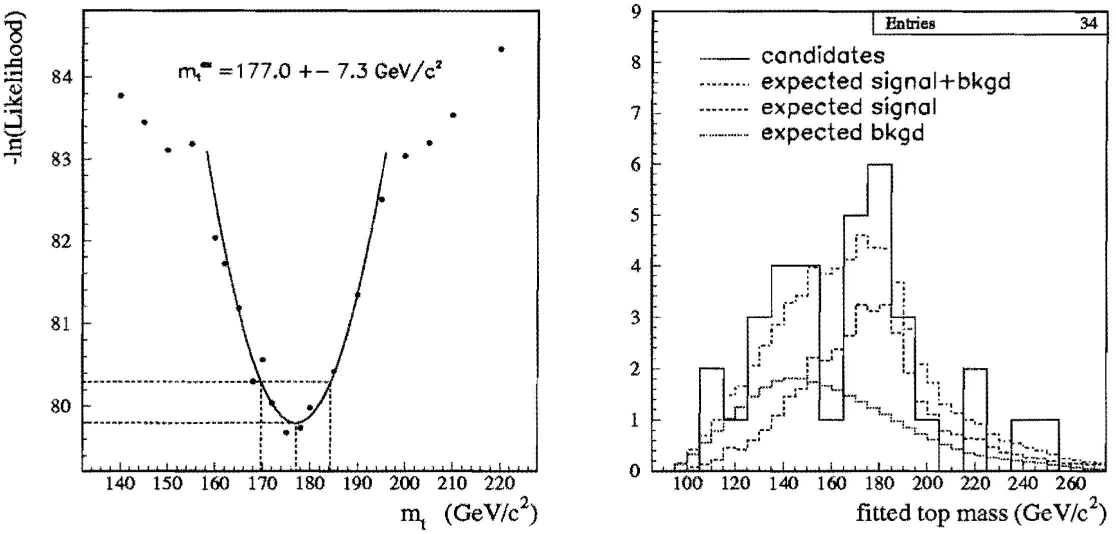

Figure 7.4: **Left**: $-\ln\mathcal{L}$ as a function of m_t. The fitted quadratic function yields $m_t = 177.0 \pm 7.3\,\mathrm{GeV}/c^2$. **Right**:The fitted top mass distribution of candidates together with the expected signal ($m_t = 178\,\mathrm{GeV}/c^2$), background, and signal+background distributions. The χ^2 between the observation and expectation is 8.86 with 13 degrees of freedom.

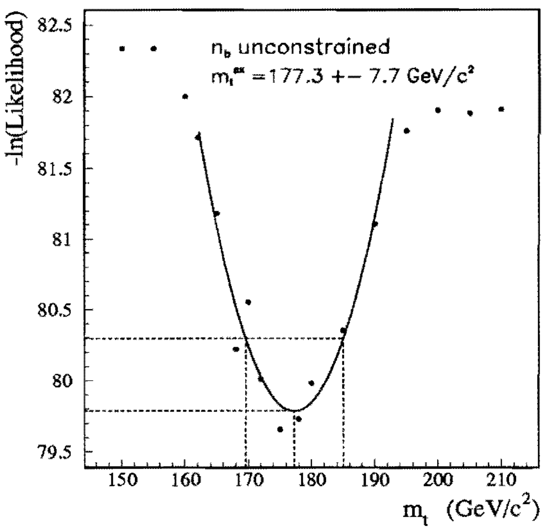

Figure 7.5: Without constraining the background number in maximizing the likelihood, the resulting $-\ln\mathcal{L}$ *vs.* m_t yields $m_t = 177.3 \pm 7.7\,\mathrm{GeV}/c^2$.

of the mean $\langle N_s \rangle = 19.0$ and $\langle N_b \rangle = 15.0$ respectively, as expected in our data. Subsequently, the fitted top mass is generated for each of the signal events from the $t\bar{t}$ m_t^{fit} distribution and for each of the background events from the background m_t^{fit} distribution. For each Monte Carlo experiment, we apply the identical likelihood method to analyze the set of generated m_t^{fit} and the extracted top mass and its statistical error, denoted as m_t^{ex} and $\sigma(m_t^{ex})$ respectively, are recorded.

Figure 7.6 shows the distribution of the resulting m_t^{ex} in 3000 Monte Carlo experiments for the true top mass 160, 170, 175, 180, 185, and 190 GeV/c^2. The fact that the peak of all the distributions is around the true top mass and the distributions are more or less symmetric with a reasonable width indicates that the likelihood method works well with no serious bias.

In addition, the statistical uncertainty of m_t^{ex} from the quadratic fit in the likelihood analysis can be checked by comparing it with $m_t^{ex} - m_t$. The distribution of $(m_t^{ex} - m_t)/\sigma(m_t^{ex})$, which is the ratio of real error to quadratic fit error, for different top masses is shown in Figure 7.7. With the width of all the distributions being approximately unity and the mean being nearly zero, Figure 7.7 suggests that $\sigma(m_t^{ex})$ is a good estimate of the statistical error on m_t^{ex}.

This test vindicates the statistical error of 7.3 GeV/c^2 in our measurement, despite the width of the m_t^{ex} distributions in Figure 7.6 being somewhat larger. The distribution of $\sigma(m_t^{ex})$ from Monte Carlo experiments for top mass 175 and 180 GeV/c^2 is shown in Figure 7.8. It indicates that the most likely $\sigma(m_t^{ex})$ is around 9 GeV/c^2, a little larger than the 7.3 GeV/c^2 error in our measurement.

7.3 Systematic Errors

From the jet energy scale study in Chapter 5, we know that the degree of inconsistency between data and Monte Carlo (event simulation) energy scales can constitute a sizable error in the top mass measurement. In addition, systematic errors may come from the likelihood method, the simulations for signal and background, and the limited statistics in the modeling signal and background m_t^{fit} spectra. These sources have been studied and the results are described in the following.

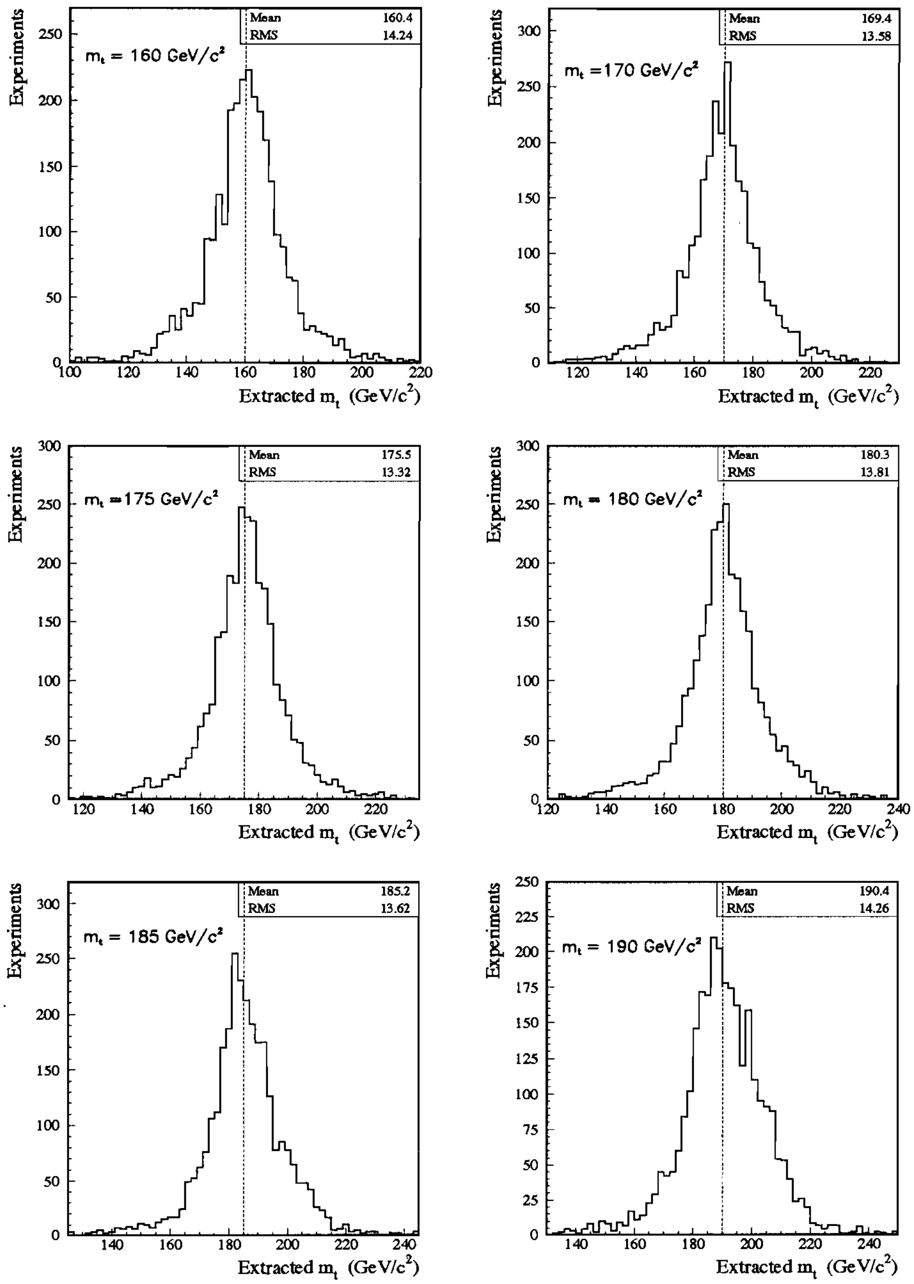

Figure 7.6: The extracted top masses in 3000 Monte Carlo experiments for top mass 160, 170, 175, 180, 185 and 190 GeV/c^2, where the observed number of signal N_s and the observed number of background N_b are fluctuated by Poisson distributions of the mean $\langle N_s \rangle = 19.0$ and $\langle N_b \rangle = 15.0$ respectively.

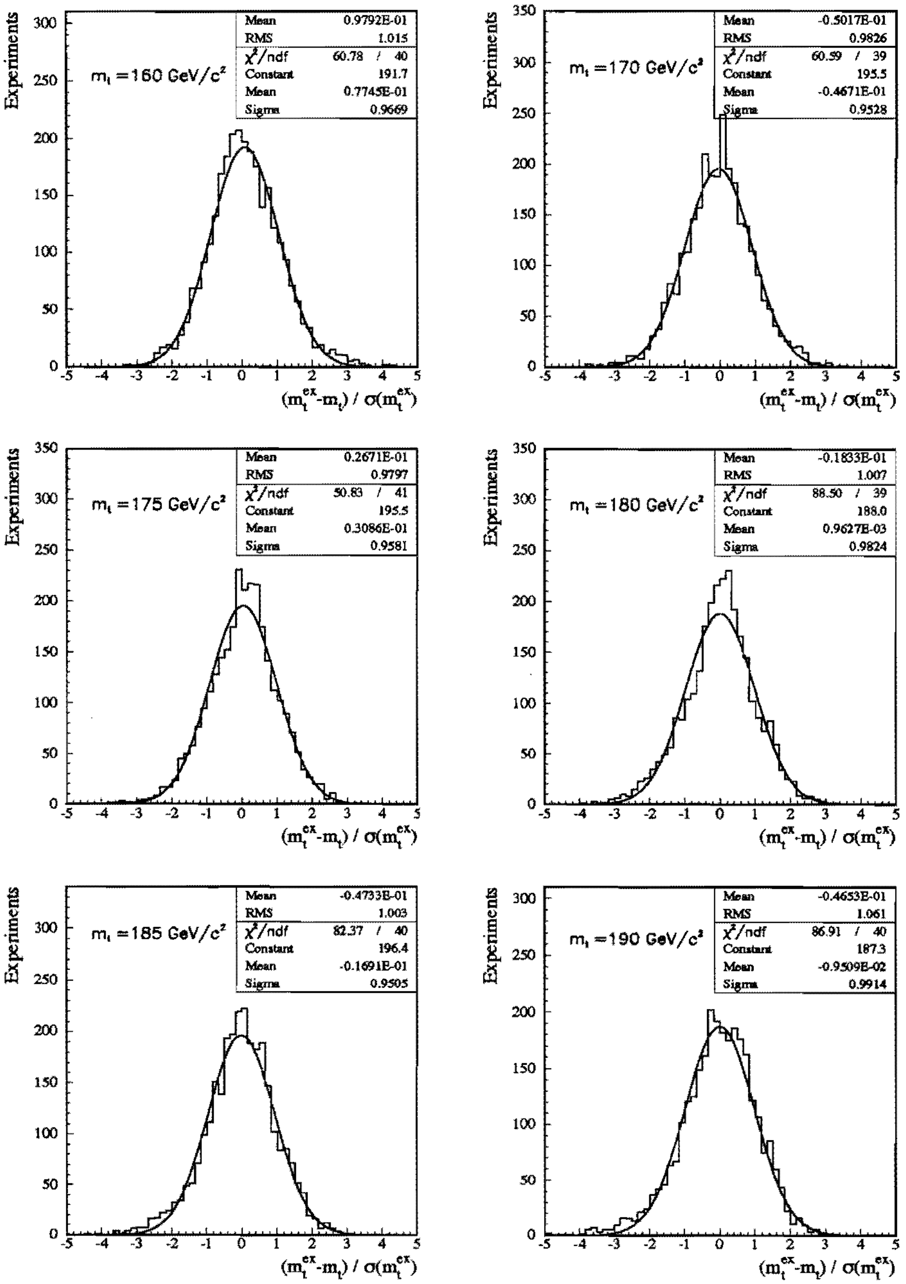

Figure 7.7: The distribution of $(m_t^{ex} - m_t)/\sigma(m_t^{ex})$ in 3000 Monte Carlo experiments for top mass 160, 170, 175, 180, 185 and 190 GeV/c^2. The fact that it has a width of approximately unity indicates that $\sigma(m_t^{ex})$ is an unbiased estimate.

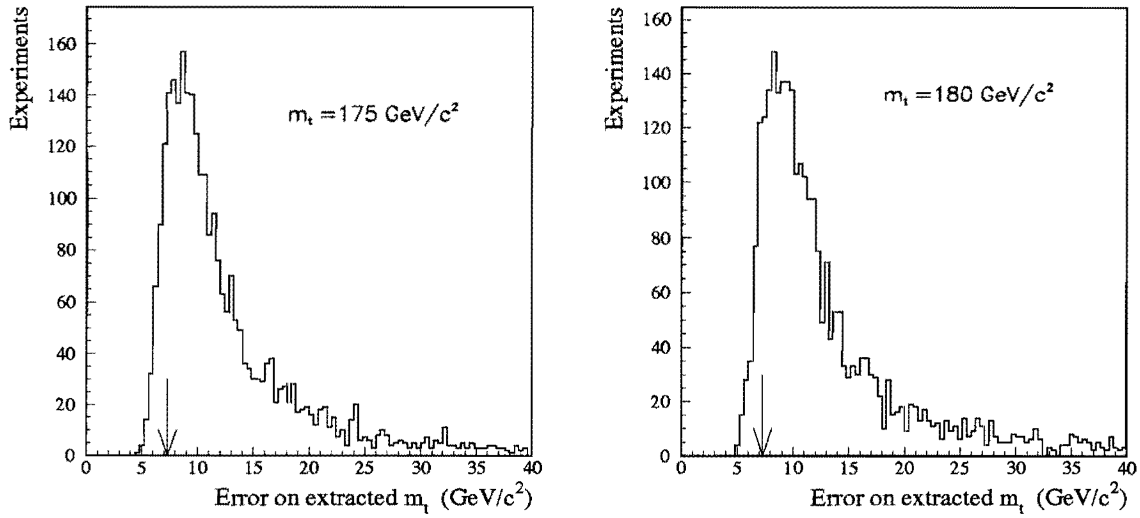

Figure 7.8: The distribution of the quadratic fit error on the extracted m_t in the Monte Carlo tests with signals of top mass 175 and 180 GeV/c^2. The arrow marks the 7.3 GeV/c^2 statistical error from our data.

7.3.1 Likelihood Method

We estimate the error due to the likelihood method from the results of Monte Carlo test in Section 7.2. The means of the extracted top masses in 3000 Monte Carlo experiments (see Figure 7.6) and their deviations from the true top mass are listed in Table 7.1. We take the average of the absolute deviations, which is 0.4 GeV/c^2, to be the systematic error due to this source.

True m_t (GeV/c^2)	160	170	175	180	185	190
$< m_t^{ex} >$ (GeV/c^2)	160.4	169.4	175.5	180.3	185.2	190.4
Deviation (GeV/c^2)	+0.4	−0.6	+0.5	+0.3	+0.2	+0.4

Table 7.1: The means of m_t^{ex} in 3000 Monte Carlo experiments in Section 7.2 and their deviations from the true top mass.

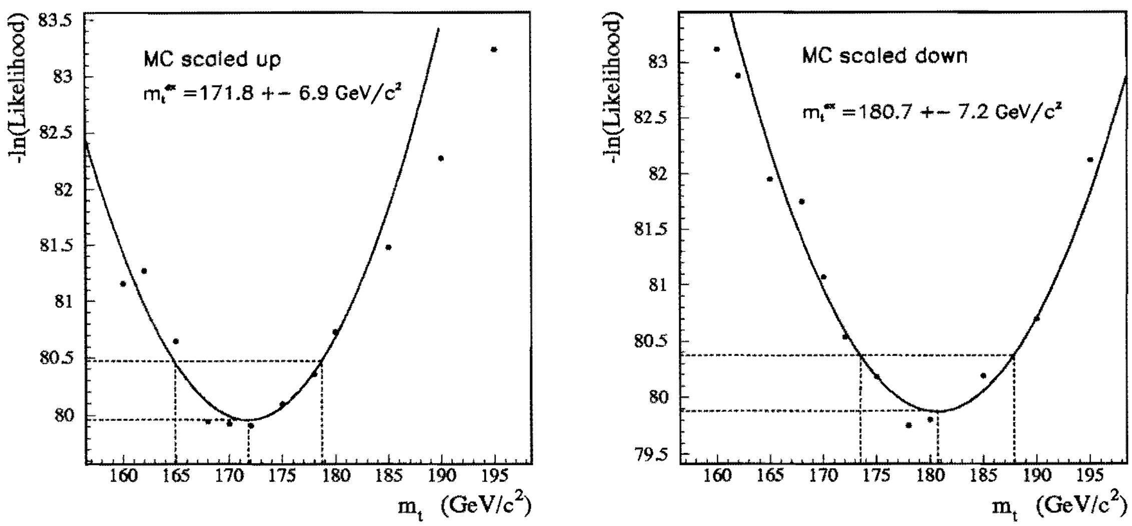

Figure 7.9: Candidates' likelihood analysis results with the jet energies of Monte Carlo events (HERWIG $t\bar{t}$ and VECBOS W + jets) scaled up and down 2.5% + 0.5 GeV.

7.3.2 Jet Energy Scale Uncertainty

The jet energy scale after a series of corrections has an uncertainty of $\pm(2.5\% + 0.5\,\mathrm{GeV}/E_T)$ as concluded in Chapter 5. This uncertainty represents the energy scale differences that may exist between data and Monte Carlo (event simulation). To determine the amount of error it translates to the measured top mass, we first raise or lower the jet energy scale of the Monte Carlo (event simulation)—including HERWIG-generated $t\bar{t}$ events and VECBOS-generated W + jets events—by the amount $\pm(2.5\% + 0.5\,\mathrm{GeV}/E_T)$. Then we perform the kinematic fit for the Monte Carlo events (MC) and repeat the likelihood analysis using the new set of models.

The likelihood analysis results are shown in Figure 7.9: the extracted top mass is 180.7 ± 7.2 GeV/c^2 when jet energies of the MC are lowered, and 171.8 ± 6.9 GeV/c^2 when jet energies of the MC are raised. Comparing with the measurement with the normal jet energies, we conclude that the shifts on m_t^{ex} due to the uncertainty of jet energy scale are ${}^{+3.7}_{-5.2}$ GeV/c^2.

7.3.3 Signal Simulation

The systematic error due to signal simulation is estimated from the difference between HERWIG and ISAJET modelings. We repeat the Monte Carlo experiments discussed in Section 7.2 with the signal fitted top masses generated by ISAJET m_t^{fit} distributions (shown in Figure 7.10) while signal modeling (provided by HERWIG m_t^{fit} distributions) for likelihood calculation remains unchanged.

The m_t^{ex} distribution for 3000 Monte Carlo experiments at top mass 160, 170, 180 and 190 GeV/c^2 are shown in Figure 7.11 and the mean of these distributions are listed in Table 7.2. The deviation of $\langle m_t^{ex} \rangle$ from the true value is typically around 1 GeV/c^2. The average absolute deviation (1.1 GeV/c^2) is taken as the systematic error from the signal modeling.

signal generated by ISAJET		
true top mass	$\langle m_t^{ex} \rangle$	$\langle m_t^{ex} \rangle - m_t$
$m_t = 160$	161.8	+1.8
$m_t = 170$	171.2	+1.2
$m_t = 180$	179.6	−0.4
$m_t = 190$	188.9	−1.1

Table 7.2: The results of $\langle m_t^{ex} \rangle$ from the Monte Carlo experiments where the signal m_t^{fit} is generated from from ISAJET (Figure 7.11). Numbers are in unit of GeV/c^2.

7.3.4 Background Simulation

Our background simulation is discussed in Section 3.3. The major background of W +jets production is simulated by the VECBOS program with the jet fragmentation modeled by HERWIG generator. In order to estimate the systematic error due to background simulation, another set of VECBOS-generated W + jets Monte Carlo events is produced. We change the renormalization scale of the process from average jet p_T to the mass of W, and replace HERWIG with ISAJET to model the jet fragmentation. This alternative W +jets Monte Carlo is then used, along with the unchanged QCD background sample from data, to make another background modeling.

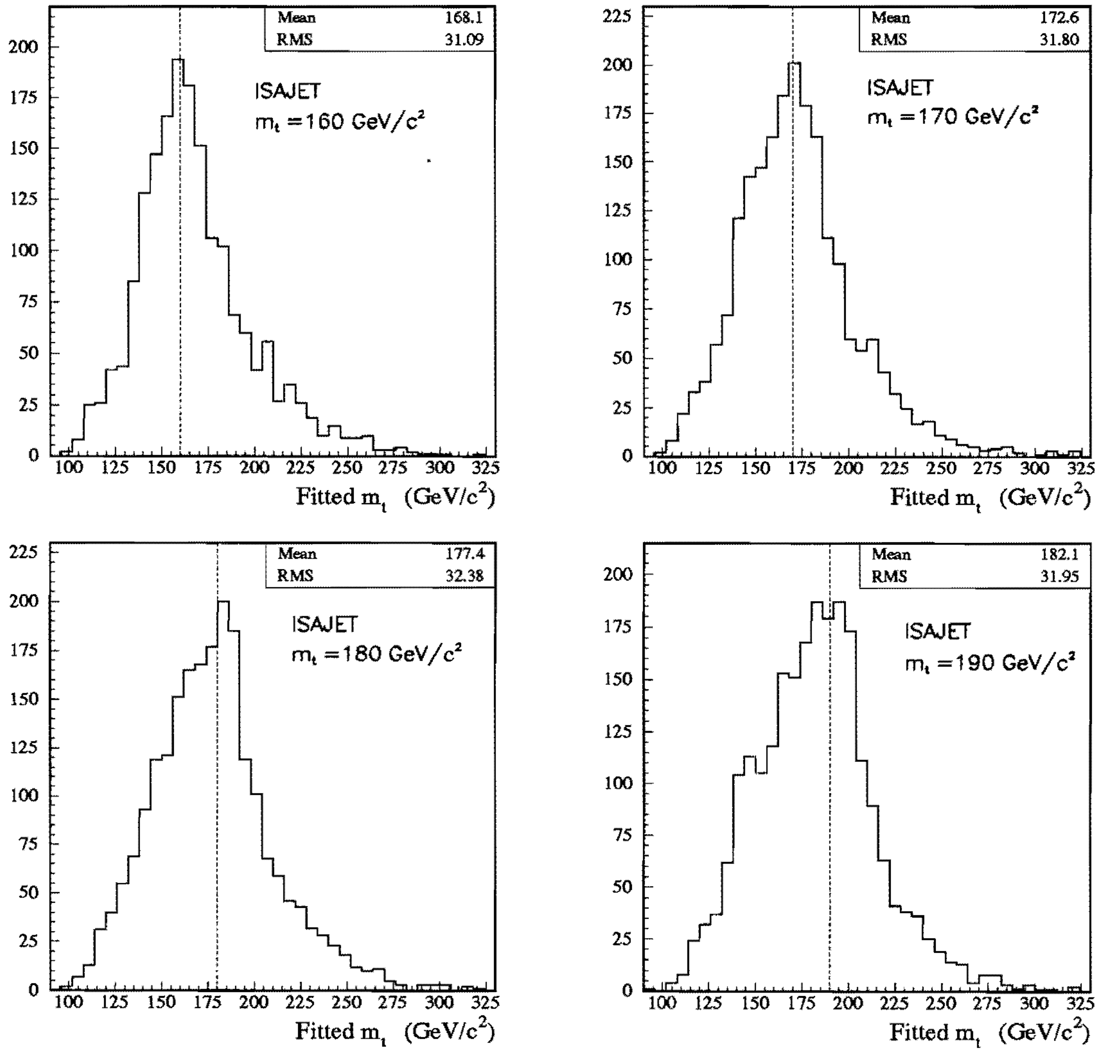

Figure 7.10: The fitted top mass m_t^{fit} distribution for ISAJET-generated $t\bar{t} \to l +$jets events with the top mass 160, 170, 180, and 190 GeV/c^2.

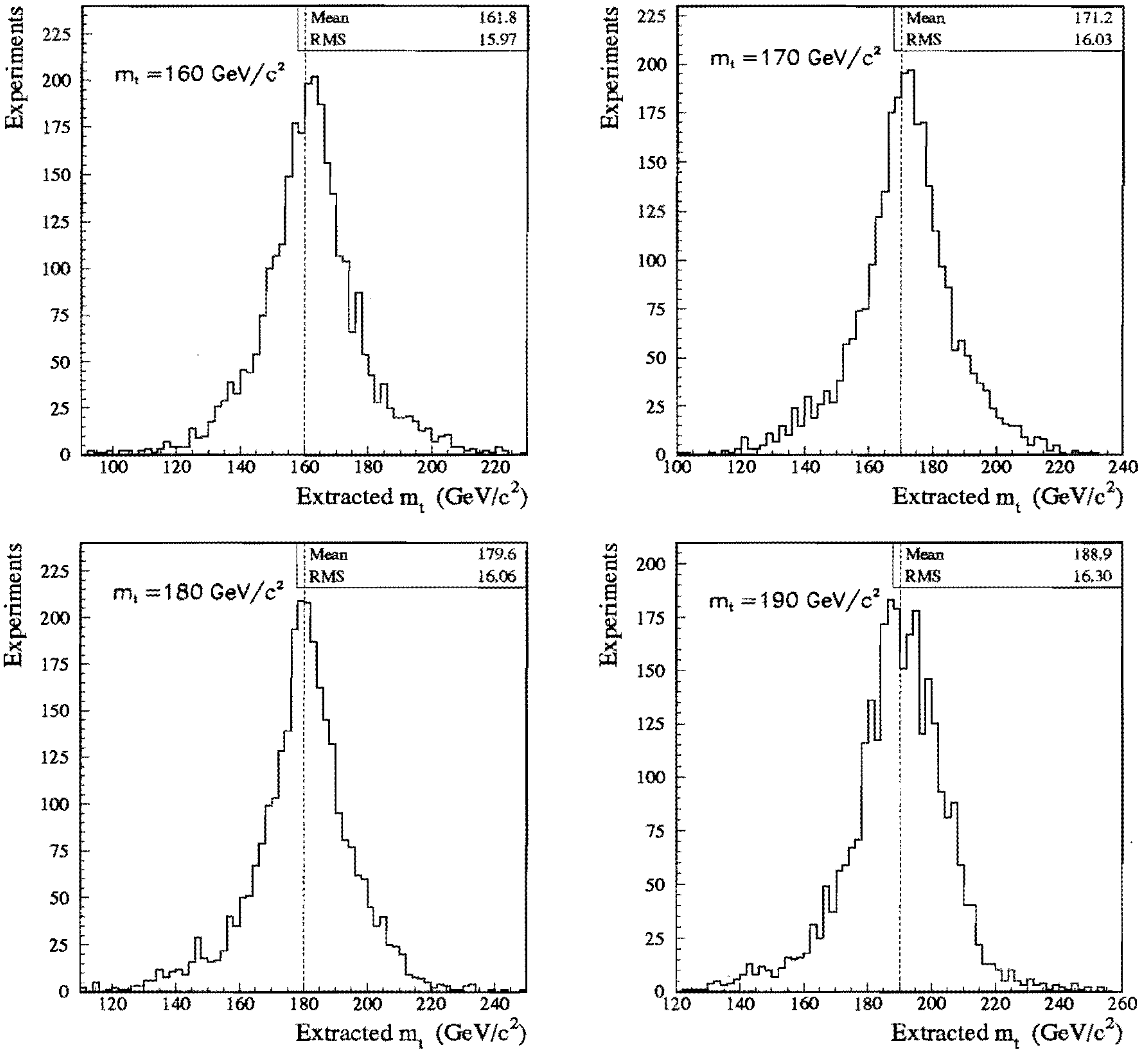

Figure 7.11: The distribution of m_t^{ex} in 3000 Monte Carlo experiments, where the signal m_t^{fit} is generated from the ISAJET spectrum.

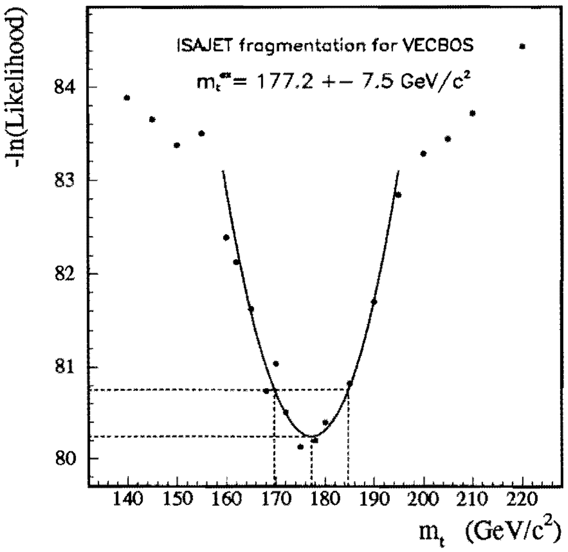

Figure 7.12: Results of a likelihood fit to data where the W + jets background simulation is provided by VECBOS with ISAJET jet fragmentation, rather than with HERWIG fragmentation as in our analysis.

When the candidates are reanalyzed by the likelihood method using this different background modeling, the change in the results is minimal: $m_t = 177.2 \pm 7.5\,\mathrm{GeV}/c^2$, as shown in Figure 7.12. However, how well VECBOS reproduces the W + jets background in our candidate sample cannot be directly studied; therefore, we conservatively assign $1.0\,\mathrm{GeV}/c^2$ as the error due to background simulation to account for possible sources that are still not well understood.

7.3.5 Modeling Statistics

The limited statistics in signal and background simulations can cause the modeled m_t^{fit} probability density spectra to fluctuate, thus affecting the result of m_t measurement. The error from this source can be estimated in the following way.

We perform the likelihood analysis for the data many times, each time both signal and background modeling spectra are properly smeared to reflect the nature of statistical fluctuation. The signal spectrum is smeared by the Poisson uncertainties of individual bins. The background shape smearing is done by first generating a

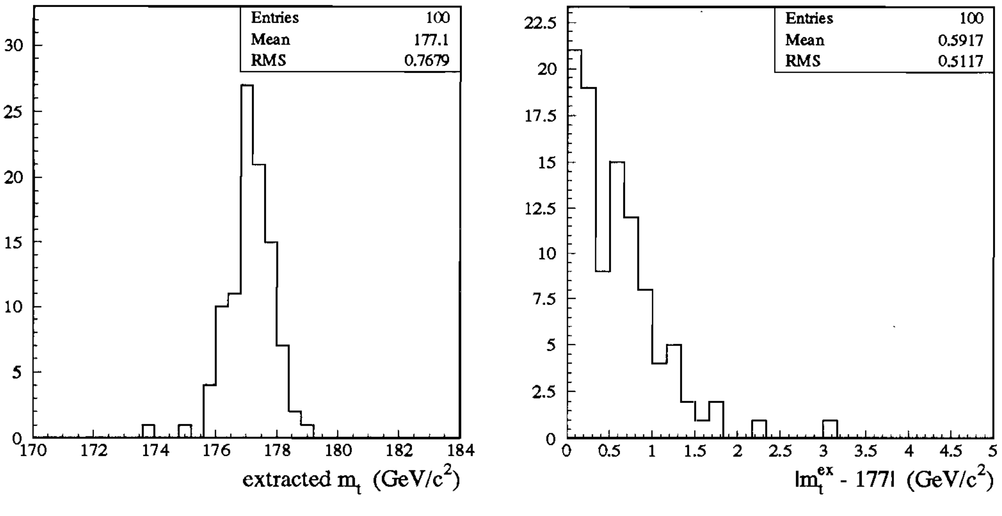

Figure 7.13: **Left**: The extracted top masses (m_t^{ex}) from data when both signal and background models are made to fluctuate statistically. **Right**: The absolute m_t^{ex} deviation from the nominal measurement ($|m_t^{ex} - 177.0\,\mathrm{GeV}/c^2|$).

new m_t^{fit} distribution of the same statistics from the original background spectrum, then normalizing and smoothing the distribution to produce a smeared background spectrum.

Figure 7.13 (Left) shows the extracted top mass (m_t^{ex}) distribution for 100 likelihood analyses for the data, with both signal and background modeling spectra independently smeared each time as described above. The distribution of absolute deviations of m_t^{ex} from the nominal measurement is shown in Figure 7.13 (Right). We take its mean of $\approx 0.6\,\mathrm{GeV}/c^2$ as the systematic error due to signal and background modeling statistics.

7.3.6 Overall Systematic Error

Systematic errors from different sources are summarized in Table 7.3. The total systematic error is calculated to be $^{+4.1}_{-5.5}$ GeV/c^2.

Source	Error (GeV/c^2)
Likelihood Method	±0.4
Jet Energy Scale	$^{+3.7}_{-5.2}$
Signal Simulation	±1.1
Background Simulation	±1.0
Modeling Statistics	±0.6
Total	$^{+4.1}_{-5.5}$

Table 7.3: Summary of estimated systematic errors.

Chapter 8

Conclusion

We have presented a top mass analysis using the data collected by the DØ detector during the 1992-1996 Tevatron run at $\sqrt{s} = 1.8\,\mathrm{TeV}$. The data represent an integrated luminosity of $\approx 100\,\mathrm{pb}^{-1}$. The analysis starts with the selection of $t\bar{t} \rightarrow l$+jets events. In the course of the analysis, we have corrected jet energies, studied the uncertainty of jet energy scale, and employed a kinematic fitting technique to reconstruct the top mass directly from individual candidate events. For each step, we tried to cross-check our results whenever possible to minimize any systematic biases of this complicated analysis. Finally, our likelihood analysis and our evaluation of systematic errors lead us to the conclusion:

$$m_t = 177.0 \pm 7.3\,(\mathrm{stat})\ {}^{+4.1}_{-5.5}\ (\mathrm{syst})\ \ \mathrm{GeV}/c^2.$$

The top quark is about 40 times as massive as the bottom quark and is the thus heaviest fundamental particle in the Standard Model. The discovery and subsequent measurements of the top quark represent major progress in our understanding of the fundamental principles of nature. This achievement is a testament to the dedication and collaboration of those involved. At this point, we cannot help but speculate how much more we can learn over the next few years.

Here at Fermilab, we expect improvements on almost every front of the top mass measurement in the next Tevatron run (Run II). After the completion of the Main Injector project, the Tevatron will be able to deliver a luminosity of $\mathcal{L} \gtrsim 10^{32}\mathrm{cm}^{-2}\mathrm{s}^{-1}$

[70], more than a ten-fold increase of that of Run I, enabling the upgraded CDF and DØ detectors to collect ~1-2 fb^{-1} of data. For the DØ experiment, the upgraded tracking system will provide powerful b-quark tagging capability with the Silicon Vertex (SVX) detector, and will improve the muon momentum resolution significantly with the installation of a tracking magnet. The resolution of the kinematic fitted top mass will be sharpened as a result of the SVX b-tagging and better muon momentum measurements. The SVX tagging technique will also help event selection, resulting in a better signal-to-background ratio and a smaller background estimate error in the candidate sample.

To get an idea of how much the statistical error can be reduced in the top mass measurement in Run II, we perform a Monte Carlo study as presented in Section 7.2 with an assumption that the experiments are conducted with the same detector and analyzed in the same way, except the data amount is ten times larger ($\approx 1\,\mathrm{fb}^{-1}$). As shown in Figure 8.1, the result for the true top mass $178\,\mathrm{GeV}/c^2$ suggests the most likely measurement error is about $3.4\,\mathrm{GeV}/c^2$. But considering all the improvements, we expect that the statistical error in Run II should be smaller.

Undoubtedly, our present systematic error will surpass the statistical error from a 1-2 fb^{-1} data set. Jet energy scales, the predominant source of our systematic error, need to be more precisely calibrated in order to improve the top mass measurement.

In short, with all the prospects of Run II in mind, we believe a total (statistical and systematic combined) error of $3\,\mathrm{GeV}/c^2$ is not impossible. Along with more precise M_W measurements, we may begin to effectively constrain the Higgs mass and set a new direction on the pursuit of the now most wanted, yet ever elusive particle.

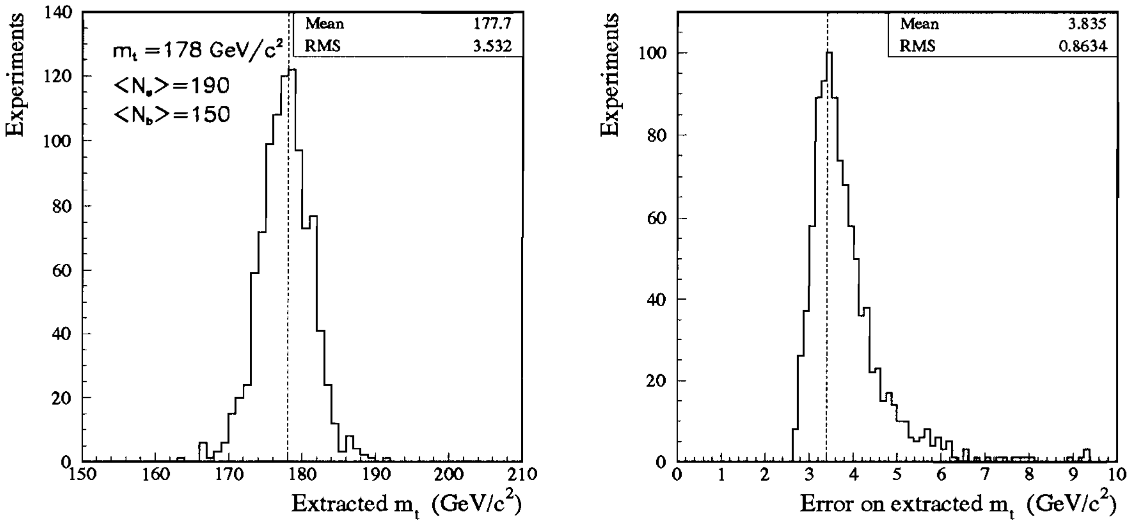

Figure 8.1: **Left**: The extracted top masses in 1000 Monte Carlo experiments where the true top mass is 178 GeV/c^2. In each experiment, the observed signal and background numbers are fluctuated by Poisson distributions of a mean $< N_s >= 190.0$ and $< N_b >= 150.0$ respectively, which is equivalent to data ten times of our present amount or about 1 fb^{-1}. **Right**: The quadratic fit errors of the m_t measurement in the Monte Carlo experiments. As marked by the dashed line, the most likely error is about 3.4 GeV/c^2.

Bibliography

[1] S. W. Herb *et al.*, Phys. Rev. Lett. **39**, 252 (1977).

[2] CDF Collaboration, F. Abe *et al.*, Phys. Rev. Lett. **74**, 2626 (1995).

[3] DØ Collaboration, S. Abachi *et al.*, Phys. Rev. Lett. **74**, 2632 (1995).

[4] V. F. Weisskopf, *The Privilege of Being a Physicist*, W. H. Freeman & Co., 1990.

[5] M. Gell-Mann, Phys. Lett. **8**, 214 (1964).

[6] G. Zweig, CERN-report TH-401 (1960) and TH-412 (1964), published in: *Developments in the Quark Theory of Hadrons, A Reprint Collection*, Vol. I: 1964-1978, edited by D. B. Lichtenberg and S. P. Rosen (Hadronic Press, Nonamtum, Ma., 1980).

[7] S. L. Glashow, J. Iliopoulos and L. Maiani, Phys. Rev. **D2**, 1285 (1970).

[8] J. J. Aubert *et al.*, Phys. Rev. Lett. **33**, 1404 (1974).

[9] J. E. Augustin *et al.*, Phys. Rev. Lett. **33**, 1406 (1974).

[10] S. L. Glashow, Nucl. Phys. **22**, 579 (1961).

[11] S. Weinberg, Phys. Rev. Lett. **19**, 1264 (1967).

[12] A. Salam, in *Elementary Particle Theory: Relativistic Groups and Analyticity (Nobel Symposium No. 8)*, edited by N. Svartholm (Almqvist and Wiksells, Sweden, 1968), p. 367.

[13] G. 't Hooft, Nucl. Phys. **B33**, 173 (1971); **B35**, 167 (1971).

[14] R. P. Feynman, Phys. Rev. **76**, 749 (1949); Phys. Rev. **76**, 769 (1949).

[15] J. Schwinger, Phys. Rev. **73**, 416 (1948); Phys. Rev. **74**, 1212 (1948).

[16] S. Tomonaga, Phys. Rev. **74**, 224 (1948).

[17] P.A.M. Dirac, Proc. Roy. Soc. Lon. **A114** 243 (1927).

[18] F. J. Hasert *et al.*, Phys. Lett. **46B**, 121, (1973); Phys. Lett. **46B**, 138 (1973); Nucl. Phys. **B73**, 1, (1974).

[19] N. Cabibbo, Phys. Rev. Lett. **10**, 531 (1963).

[20] M. Kobayashi and K. Maskawa, Prog. Theor. Phys. **49**, 652 (1973).

[21] R. P. Feynman, Phys. Rev. Lett. **23**, 1415 (1969).

[22] J. D. Bjorken and E. A. Paschos, Phys. Rev. **185**, 1975 (1969).

[23] D. J. Gross and F. Wilczek, Phys. Rev. **D8**, 3633 (1973); **D9**, 980 (1974).

[24] H. D. Politzer, Phys. Rev. Lett. **26**, 1346 (1973); Phys. Rep. **14C**, 129 (1974).

[25] UA1 Collaboration, G. Arnison *et al.*, Phys. Lett. **B147**, 493 (1984); C. Albajar *et al.*, Z. Phys. **C48**, 1 (1990).

[26] UA2 Collaboration, T. Akesson *et al.*, Z. Phys. **C46**, 179 (1990).

[27] CDF Collaboration, F. Abe *et al.*, Phys. Rev. Lett. **64**, 147 (1990); Phys. Rev. Lett. **64**, 142 (1990); Phys. Rev. **D43**, 664 (1991); Phys. Rev. Lett. **68**, 447 (1992); Phys. Rev. **D45**, 3921 (1992).

[28] DØ Collaboration, S. Abachi *et al.*, Phys. Rev. Lett. **72**, 2138 (1994).

[29] E. Laenen, J. Smith, and W. van Neerven, Phys. Lett. **B321**, 254 (1994).

[30] J. F. Donoghue, E. Golowich, and B. R. Holstein, *Dynamics of the Standard Model*, Cambridge University Press, 1992, Chap. 1.

[31] R. N. Cahn, Rev. Mod. Phys. **68**, 951 (1996).

[32] F. Halzen, B. Kniehl and M. L. Stong, Z. Phys. **C58**, 119 (1993); F. Halzen and B. A. Kniehl, Nucl. Phys. **B353**, 567 (1991).

[33] L. M. Lederman, "The Tevatron," Scientific American, Vol.264, p.53, March 1991.

[34] J. Thompson, Fermilab Report No. FERMILAB-TM-1909, 1994.

[35] J. D. Jackson, *Classical Electrodynamics*, 2nd ed., John Wiley & Sons, 1975, p. 661.

[36] DØ Collaboration, S. Abachi *et al.*, Nucl. Instrum. Methods **A338**, 185 (1994).

[37] P. Rice-Evans, *Spark, Streamer, Proportional, and Drift Chambers*, The Richelieu Press, London, 1974, Chap. 10.

[38] F. Sauli, CERN Report 77-09, 1977.

[39] F. Sauli in *Experimental Techniques in High Energy Physics*, edited by Thomas Ferbel (Addison-Wesley, 1987), p. 79.

[40] A. R. Clark *et al.*, Nucl. Instrum. Methods **A315**, 193 (1992).

[41] A. R. Clark *et al.*, Nucl. Instrum. Methods **A279**, 243 (1989).

[42] R. Avery *et al.*, IEEE Trans. Nucl. Sci. **NS-40**, 573 (1993).

[43] J. F. Detoeuf *et al.*, Nucl. Instrum. Methods **A265**, 157 (1988); **A279**, 310 (1989).

[44] Particle Data Group, Phys. Rev. **D50**, 1173 (1994).

[45] S. J. Wimpenny *et al.*, Nucl. Instrum. Methods **A279**, 107 (1989); M. Abolins *et al.*, Nucl. Instrum. Methods **A280**, 36 (1989).

[46] C. Brown *et al.*, Nucl. Instrum. Methods **A279**, 331 (1989); J. M. Butler *et al.*, Nucl. Instrum. Methods **A290**, 122 (1990); Yu. M. Antipov *et al.*, Nucl. Instrum. Methods **A297**, 121 (1990).

[47] C. Gerber *et al.*, "Muon Momentum Determination," DØ Note 2140, 1994 (unpublished).

[48] G. S. Gao and R. Partridge, IEEE Trans. Nucl. Sci. **NS-38**, 286 (1991).

[49] M. Abolins *et al.*, IEEE Trans. Nucl. Sci. **NS-36**, 384 (1989); Nucl. Instrum. Methods **A289**, 543 (1990).

[50] D. Edmunds, S. Gross, and P. Laurens, "The Level 1.5 Trigger Framework for DØ," DØ Note 1638, 1993 (unpublished).

[51] J. Drinkard, "The DØ Level 1.5 Calorimeter Trigger," DØ Note 2274, 1994 (unpublished).

[52] D. Cutts *et al.*, IEEE Trans. Nucl. Sci. **NS-36**, 738 (1989).

[53] DØ Collaboration, M. Narain, in *The Fermilab Meeting Proceedings of Meeting of the Division of Particles and Fields of the American Physical Society, Batavia, Illinois, 1992*, edited by C. Albright, P. Kasper, R. Raja and J. Yoh (World Scientific, Singapore, 1993).

[54] M. Narain and U. Heintz, "A likelihood Test for Electron ID," DØ Note 2386, 1994 (unpublished).

[55] UA1 Collaboration, G. Arnison *et al.*, Phys. Lett. **123B**, 115 (1983); **132B** 21 (1983).

[56] CDF Collaboration, F. Abe *et al.*, Phys. Rev. Lett. **69**, 2898 (1992).

[57] DØ Collaboration, J. A. Guida, in *Proceedings of the 4th International Conference on Advanced Technology and Particle Physics*, Como, Italy, 1994 (unpublished); Fermilab Report No. FERMILAB-CONF-95/010-E, 1995 (unpublished); DØ Collaboration, J. Kotcher, Fermilab Report No. FERMILAB-CONF-95/007-E, 1995 (unpublished).

[58] R. Astur and R. Kehoe, "Determination of the hadronic energy scale of DØ calorimetry," DØ Note 2908, 1996 (unpublished); R. Kehoe, *Proceedings of the*

6th International Conference on Calorimetry in High Energy Physics, Frascati, Italy, 1996.

[59] G. Marchesini and B. Webber, Nucl. Phys. **B310**, 461 (1988); I. G. Knowles, Nucl. Phys. **B310**, 571 (1988); G. Marchesini *et al.*, Comp. Phys. Comm. **67**, 465 (1992).

[60] F. Paige and S. Protopopescu, BNL Report No. BNL38034, release v6.49, 1986 (unpublished).

[61] DØ Collaboration, J. Womersley, *Proceedings of the XXVI International Conference on High Energy Physics*, Dallas, Texas, 1992, edited by J. Sanford, AIP Conf. Proc. No. 272 (AIP, New York, 1993).

[62] F. A. Berends, H. Kuijf, B. Tausk, and W. T. Giele, Nucl. Phys. **B357**, 32 (1991).

[63] DØ Collaboration, S. Abachi *et al.*, Phys. Rev. **D52**, 4877 (1995).

[64] DØ Collaboration, M. Strovink, in *Proceedings of the 11-th Topical Workshop on $p\bar{p}$ Collider Physics*, Padova (1996); Fermilab Report No. FERMILAB-CONF-96/336-E, 1996.

[65] V. D. Barger and R. J. N. Phillips, *Collider Physics*, Addison-Wesley, 1987, Chap. 9.

[66] F. Hsieh and H. Lan, "Post-CAFIX Jet Corrections For Top Mass Analyses," DØ Note 3055, 1996 (unpublished).

[67] F. Hsieh "Study of the Jet Energy Scale Using $\gamma + 1\,$jet Events," DØ Note 3130, 1996 (unpublished).

[68] O. I. Dahl, T. B. Day, F. T. Solmitz, and N. L. Gould, "SQUAW Kinematic Fitting Program," Group A Programming Note No.P-126, Lawrence Berkeley Laboratory, Berkeley, California, July, 1968.

[69] F. James *et al.*, MINUIT-Reference Manual, CERN Program Library D506, Version 92.1, CERN Geneva, Switzerland, March, 1992.

[70] Tev-2000 Study Group, D. Amidei *et al.*, Fermilab Report No. FERMILAB-Pub-96/082, 1996 (unpublished).